



ROMA TRE UNIVERSITY
Department of Mathematics and Physics
Doctoral School in Mathematics and Physics
XXVIII Cycle

Ph.D. Thesis in Physics

**New Methodologies for Uranium, Radium and
Tritium Groundwater Analysis**

by
Lorenzo Copia

Rome, 2015

Tutor
Prof. Wolfango Plastino

Coordinator
Prof. Roberto Raimondi

Contents

Introduction	3
1 Uranium, Radium and Tritium	6
1.1 Uranium geochemistry in groundwater	6
1.2 Radium geochemistry in groundwater	8
1.3 Tritium in groundwater	9
1.4 Water-rock interaction and transport modeling	10
2 Methodologies	15
2.1 Inductively Coupled Plasma Mass Spectrometry	15
2.1.1 Sample introduction	16
2.1.2 Source	16
2.1.3 Mass spectrometer	18
2.1.4 Detector	20
2.1.5 Quantitation	21
2.1.6 Interferences	21
2.2 Liquid Scintillation Counting	23
2.2.1 Liquid Scintillation	23
2.2.2 Photomultiplier	25
2.2.3 Interferences in Liquid Scintillation Counting	26
2.2.4 Equipment	28
3 Measurements	29
3.1 Tritium measurements	29
3.1.1 Electrolysis of water	29
3.1.2 Electrolytic enrichment	30
3.1.3 Contamination	33
3.1.4 Tritium activity concentration	33
3.1.5 Materials and Results	37
3.2 Radium measurements and new developments	38
3.2.1 Extraction Chromatography	39

3.2.2	Ion Exchange Chromatography	41
3.2.3	Reagents and standards	41
3.2.4	Equipment	41
3.2.5	Sample preparation	42
3.2.6	Results	45
3.3	Uranium isotopic ratio measurements	51
3.3.1	Materials	52
3.3.2	Equipment	52
3.3.3	Results	54
4	Results and discussion	56
4.1	Gran Sasso aquifer	56
4.2	Experimental setup	59
4.3	Tritium time series	62
4.3.1	Tritium Data Analysis	64
4.4	Radium time series	73
4.4.1	Radium Data Analysis	74
4.5	Uranium isotope ratios analysis	79
4.6	Discussion	80
	Conclusion	85
	Appendix	86
A	Uncertainty Assessment	87

Introduction

Underground facilities of Gran Sasso National Laboratories (LNGS-INFN) are located inside the largest aquifer of central Italy and within the calcareous formation of an upturned syncline, near the main overthrust fault. It is a complex geological system, in which water masses pass through different types of rock (more or less permeable), by different paths and are, therefore, characterized by their own percolation features, that influence their main chemical-physical properties.

In the framework of the National Institute of Nuclear Physics activities, the ERMES (Environmental Radioactivity Monitoring for Earth Sciences) experiment originates with the intent of estimating environmental radioactivity inside LNGS, as a contribution to the background noise for neutrino and dark matter physics experiments.

Since June 2008, uranium content, along with other chemical-physical groundwater characteristics, was monitored weekly with the aim of determining possible radon sources in groundwater, radon transport through cataclastic rocks, and analyzing, at the same time, uranium contribution to the neutron flux in the Underground Laboratories [1].

Uranium content anomalies, observed until March 2009, have been related to the seismic activity of the area, culminated in a violent earthquake (magnitude $M_w = 6.3$) on April the 6th, 2009, whose epicenter was located about 18 km from LNGS [2]. Abrupt variations in uranium concentrations have been associated, as possible physical explanation, with the upward movements of endogenic fluids related with the geodynamics of the earthquake [3]. Therefore uranium was proposed as a potential new indicator of geodynamical processes that can precede an earthquake.

In order to single out those parameters variations that are not due the usual aquifer dynamics, this last must be thoroughly investigated. Therefore the aquifer hydrological setting must be known together with local dynamics in the aquifer. Discerning these dynamics and relating them with the uranium behavior over a time span which includes intense seismic activity and the periods preceding and following it is exactly the purpose of this work.

The hydrogeological description of an aquifer is generally obtained by means of a black-box model with an input (meteoric events), an output (springs) and calculating its transfer function. In this description, we benefit from the unique position of being "inside the black box": in fact, the sampling sites inside the underground laboratories are located in the core of the aquifer, in the saturated part below the water table oscillation zone, and on the two sides of the overthrust fault.

A new approach had to be sought in order to achieve the proposed scope: the behavior of three elements 3H , ^{234}U , and ^{226}Ra , along with ^{238}U concentration, were to be studied, by applying, modifying and, when needed, developing to the purpose distinct measurement techniques and comparing the results over time. Tritium, a radioactive isotope of hydrogen, was chosen because of its features in defining groundwater masses movements and mixing without being affected by the water-rock interaction. $^{234}U/^{238}U$ was chosen because it might provide useful information on the uranium dynamics and a characterization of the aquifer. ^{226}Ra concentration and $^{226}Ra/^{238}U$ allow to investigate water-rock interactions and disequilibrium along the ^{238}U decay-chain.

Studying these element behaviors over time might highlight different aspects regarding the response of such an aquifer to an external forcing such as an earthquake. Moreover, uranium and radium are the parent nuclides of radon, so knowing their concentrations and their geochemical differentiated patterns with respect to environmental pH and redox potential, might be useful to explain radon variations out of the consolidated scheme which relates them with stress-strain processes in the rock.

This work is divided into four chapters:

- The first chapter deals briefly with groundwater geochemistry of uranium and radium, water-rock interaction processes and transport equation with particular interest in ^{238}U , ^{234}U , ^{226}Ra and ^{222}Rn patterns. Tritium features, its role in describing water cycle and exchanges among reservoirs are also presented.
- The second chapter treats the operating principles of the adopted measurement techniques: Inductively Coupled Plasma Mass Spectrometry (ICPMS) for uranium and radium and Liquid Scintillation Spectrometry (LSS) for tritium.
- Chapter 3 introduces in detail the sample pretreatment procedures and instrumental protocols, which were developed, optimized and adopted in this work.

- Chapter 4 describes the experimental set up, the results of each single element of interest for each site are reported and analyzed. An overall discussion of the results is also presented.

Chapter 1

Uranium, Radium and Tritium

1.1 Uranium geochemistry in groundwater

Uranium (atomic number 92) is a silvery-white metal, toxic and radioactive. When pure, it is malleable, ductile and slightly paramagnetic. In nature its isotopic composition consists of three major isotopes: ^{234}U ($\sim 0.005\%$), ^{235}U ($\sim 0.720\%$) and ^{238}U ($\sim 99.275\%$). As a result of nuclear fission, also isotopes ^{233}U and ^{236}U are present in traces. Low uranium concentrations are virtually found in all rocks and soils ($\sim (0.7 - 11) * 10^{-6}g/g$), and in almost all waters ($\sim (0.1 - 50) * 10^{-9}g/g$), usually combined with other elements [4].

Isotopes ^{238}U and ^{235}U give rise to two decay chains, shown in figure 1.1, which shows radioactive isotopes of many different elements. Geochemical properties can cause fractionation among these elements in the various ambients such as rocks, soils, and waters; this fractionation may occur also among isotopes of the same element, known as isotopic fractionation. Both these processes give rise to disequilibria in the decay chains.

Uranium presence in groundwater and soil plays an important role in the description and analysis of underground aquifers. The uranium transport mechanism in natural waters has been studied for a great number of systems with the aim of dating underground waters by means of uranium isotope disequilibrium.

From a chemical point of view uranium exists in four distinct oxidation states U(III), U(IV), U(V) and U(VI), the most common in nature being U^{6+} and U^{4+} . The first is dominant on the earth's crust as U^{4+} is generally insoluble and therefore much less mobile than U^{6+} .

Concentrated deposits of uranium are found in uraninite, $U(IV)O_2$; due to the atmospheric agents action on uraninite, other secondary minerals containing uranium are obtained: uranium oxyhydroxides, phosphates, silicates,

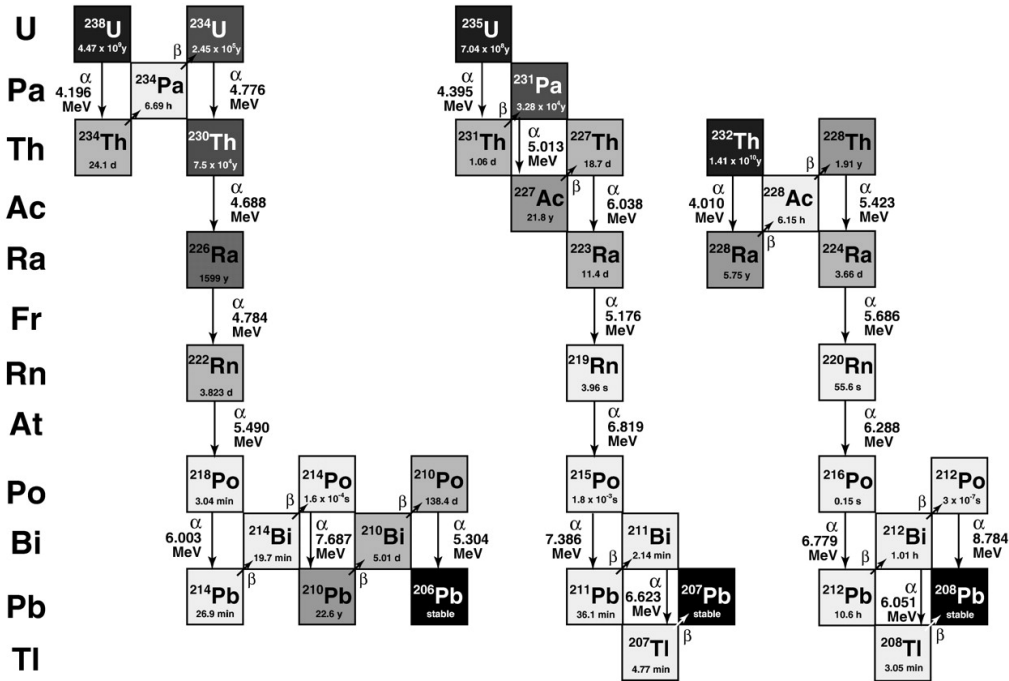
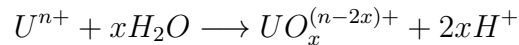


Figure 1.1: ^{238}U , ^{235}U and ^{232}Th decay chains.[5]

sulfates and carbonates of [5].

Uranium chemistry in aqueous solution depends on its ability to bind with other present ions. In pure water, considering uranium in a generic state U^{n+} , the following hydrolysis reaction takes place:



so that, for example, U^{6+} is present in solution as uranyl ion UO_2^{2+} . Under reducing condition, increasing pH hydroxy complexes $U(OH)^{(n-1)+}$ and $UO_xOH^{(n-2x-1)+}$ are formed.

In oxidizing environments the dominating species will depend on Eh-pH conditions, temperature, concentration and availability of complexing ions. Binding with elements or inorganic complexes such as F^- , Cl^- , PO_4^{3-} , CO_3^{2-} regulates uranium mobility, usually forming compounds such as uranyl carbonate, uranyl chloride and uranyl sulfate. For example, in presence of low concentrations of CO_2 and pH above 5 the dominant species are various uranyl carbonate complexes, as shown in figure 1.2.

As it can be seen [7], the most important complexes are the free uranyl ion below $pH = 3$, fluoride for $pH = 3 - 4$, phosphate for pH values of 4-7.5, and the carbonate complexes above $pH = 7.5$.

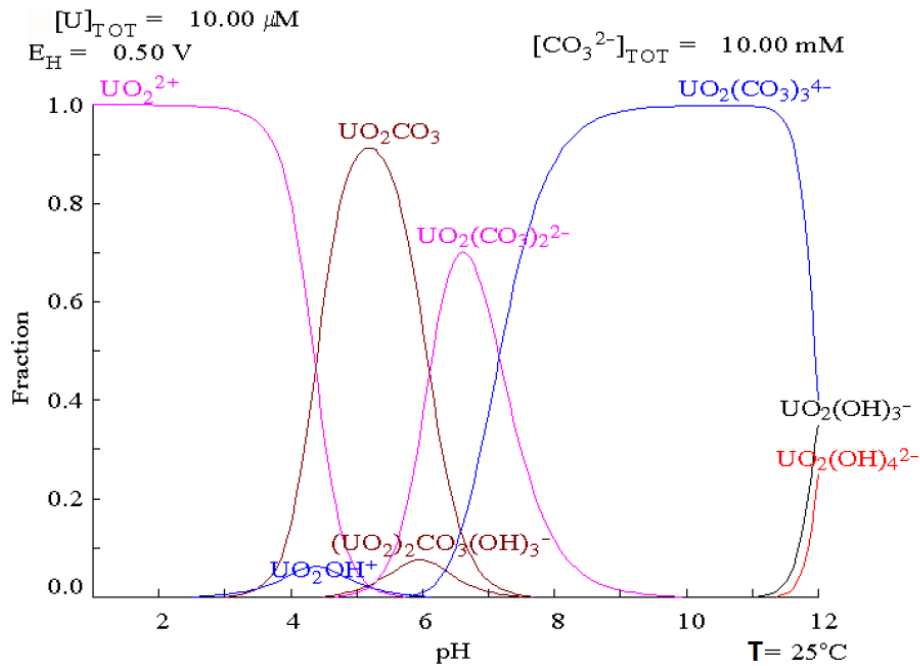


Figure 1.2: Relative concentrations of uranium chemical forms in carbonate solution.[6]

If the decay chain were in secular equilibrium, the isotope ratio between the isotopes ^{238}U and ^{234}U should remain constant in groundwater at the same level as in rock, however, this does not occur and an excess of ^{234}U has been measured anywhere in the world and is widely reported in literature [5]. This excess is normally justified by the higher ^{234}U mobility, due to its greater efficiency in forming UO_2^{2+} (highly soluble) than ^{238}U , most of which remains in oxidation state IV, practically insoluble. Otherwise it is possible to justify the ^{234}U isotope excess as resulting from input by recoil of the ^{234}Th [5].

1.2 Radium geochemistry in groundwater

Radium (atomic number 88) is a metal, when pure it is bright white, it darkens in contact with air and exhibits luminescence as well as its salts do. By nature radium is present in 36 known isotopes, four of which are natural: ^{228}Ra and ^{224}Ra from the decay chain of ^{232}Th (figure 1.1), ^{226}Ra and ^{223}Ra belonging to the chains of ^{238}U and ^{235}U .

^{226}Ra , the most abundant, decays alpha in ^{222}Rn with a half-life of 1599

years. It is present in all minerals where uranium can be found, therefore, in particular, in uraninite (or pitchblende) and carnotite [4]. It belongs to the group of alkaline earth metals, but, compared to Ca or Sr it is slightly more soluble; its solubility depends on sulphates and carbonates concentration in groundwater. Its chemical behavior is almost completely equivalent to that of barium.

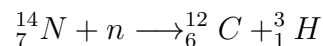
Radium speciation in groundwater has been documented in literature, although some aspects, related to material transport by means of colloids or to differentiated distribution of uranium and thorium in the aquifer, are often not taken into account [8].

Generally, in solutions with low salinity, radium can be found as free ion Ra^{2+} , while significant complexing as $RaSO_4$, $RaCO_3$ and $RaCl^+$ can occur at high concentration of dissolved ions. In natural environment, radium hardly reaches saturation, while it precipitates as carbonate.

Clearly, the initial content in groundwater depends on the amount dissolved from the host aquifer rock, but adsorption exerts a strong control on ^{226}Ra concentration, this process heavily depends on the type of mineral, on the pH, on the redox potential (ORP) and on the temperature of the solution.

1.3 Tritium in groundwater

Tritium is a radioactive hydrogen isotope, in nature it is originated in very small amounts mainly by the interaction of cosmic rays with nitrogen in the atmosphere, according to the following reaction:



the mean production rate was estimated to be around $7 * 10^4 TBq$ per year for the whole atmosphere; its production takes place in stratosphere and troposphere [12].

It decays β^- as



with a half life $T_{\frac{1}{2}} = 12.33 y$ and a maximum peak energy $E_{max} = 18 keV$.

Tritium exists as a hydrogen gas (T , HT , DT) which is oxidized to HTO and removed from the atmosphere by precipitation and isotope exchange with the oceans. The meteoric water tritium content shows a latitudinal and a seasonal dependence, the average level in continental precipitation ranging between 1 and 20 tritium units (TU) [13], where one TU is defined as

$$1 \text{ TU} \equiv \frac{[{}^3\text{H}]}{[\text{H}]} = 10^{-18}$$

Precisely because of its features, since the discovery of cosmic-ray produced tritium in 1949 [14], this isotope has been widely used in investigating the dynamics of water movement at the different levels of the global water cycle (atmosphere, ocean, groundwater, rivers, lake, etc.) with a number of publications exceeding several thousands [12].

Other sources of tritium are nuclear explosions and nuclear facilities. The former were performed in atmosphere mainly between 1952 and 1963, releasing an amount of tritium greater than the natural amount by orders of magnitude. This, so called "bomb pulse", has been utilized to trace fluxes and exchanges among different reservoirs in hydrology. Presently, levels in precipitation can be considered back to the natural ones [13]. The latter discharge tritium into the atmosphere giving rise to variations on a local scale [12].

Nowadays in hydrology tritium is mainly used in constraining groundwater residence times, recharge rates and in dating groundwater masses over a time span of 100 years. This because ${}^3\text{H}$ abundance in ground water isolated from atmosphere is only affected by radioactive decay and not by reactions between water and aquifer matrix. To accomplish these tasks tritium input function due to rainfalls has to be known [15].

In principle, the knowledge of tritium concentration alone enables to distinguish water masses with different percolation and residence times within the same aquifer and it can also be used in evaluating the mixing between them. Moreover by monitoring tritium level it is possible to distinguish seasonal effects caused by rainfall or snow melting and acquire information on the dynamics of the aquifer.

1.4 Water-rock interaction and transport modeling

The metals and radionuclides transport through porous media is strongly influenced by possible interactions between host aquifer rock and water. In order to describe these interactions and predict U- and Th-decay series behavior in aquifers, several different models were developed. A detailed discussion of models and general equations governing these phenomena is provided in [9, 8, 10]. In this section the general characteristics of the models and processes controlling nuclides distribution are summarized.

In the above models three phases are considered: groundwater with a constant linear Darcy's velocity v_w , host aquifer rock with a porosity n , and a surface layer that coats grains with a thickness ζ . The last one, also called active surface layer, consists of the adsorbed atoms on the surface of the grain.

Adsorption is a chemical-physical phenomenon, usually reversible, whereby molecules, atoms or ions establish an interaction through Van Der Waals or electrostatic forces on an interphase surface (physical adsorption), or through formation of chemical bonds (chemical adsorption). The relationship between concentrations of dissolved and adsorbed species in low concentrations systems follows a linear path; however, if concentrations in solution increase, the surface is saturated and the concentration of adsorbed species tends asymptotically to an upper limit. The phases mentioned above are also three nuclides pools with different species, concentrations, and exchange times. In figure 1.3 model phases and relative interactions are shown.

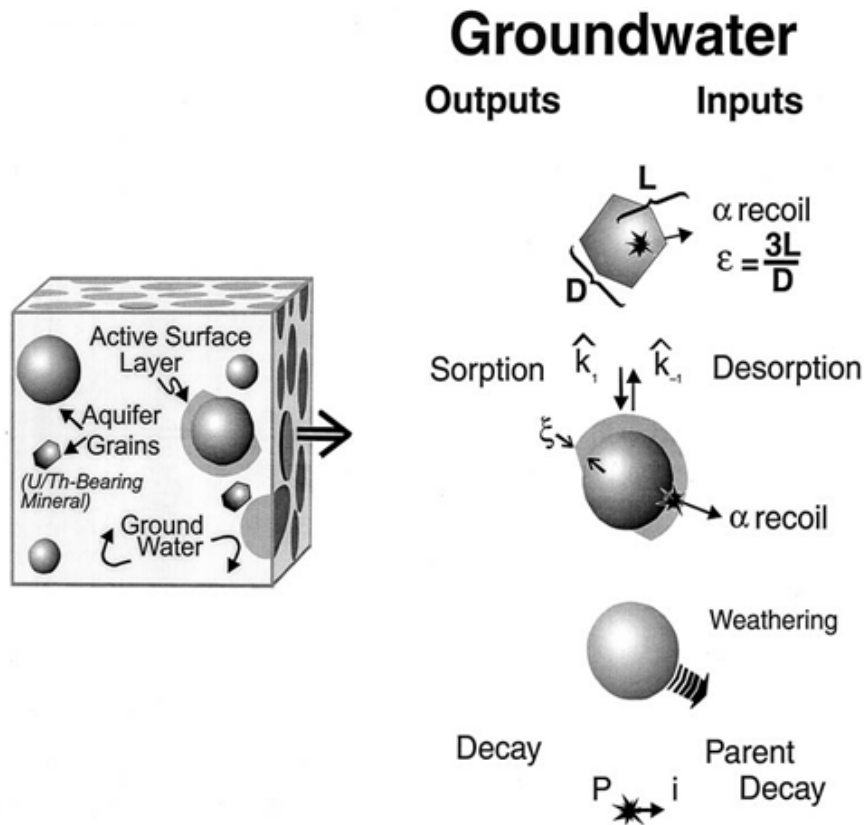


Figure 1.3: Model of an aquifer with the three phases and principal water-rock processes [10].

Referring to a generic radionuclide belonging to the chains of uranium and thorium, concentration level and its possible variations in groundwater are related to water-rock interactions, that consist of the following phenomena:

- **Input by weathering.** This phenomenon is modeled as a mineral, with molar concentration I_r , releasing nuclides with a constant rate w_I due to the erosion of the material. It is normally assumed that all radionuclides belonging to a decay chain have the same release rate [8].
- **Input by recoil.** Parent radionuclide, with molar concentration P_R in rock, releases by direct recoil the daughter nuclide in water. Only a fraction ϵ_i of the daughter nuclide atoms are released in water because the direction of the recoil is clearly casual and the emittance depends on the nuclide energy and on the distance from the surface of the grain.
- **Input by decay.** It is the production from decay of dissolved parent (with molar concentration P_w) in solution.
- **Input by desorption.** Adsorbed nuclides of molar concentration I_{ads} are desorbed according to a first-order rate constant k_{-1}^I .
- **Input by production from sorbed parent atoms.** Considering sorbed parent atoms of molar concentration P_{ads} , they produce daughter atoms by α -decay. A fraction f_I is released into the surrounding groundwater.
- **Removal by precipitation.** It depends on environment, acid or basic, on radionuclide concentration and solubility and on dissolved ions. Only in case of precipitation of low-concentration species by partitioning into phases defined by other elements, it can be described as a first-order process with constant rate Q_i [11].
- **Removal by decay.** it is the decay of I in water.
- **Removal by adsorption.** It is modeled as a first-order process with a constant rate k_1^I .

These phenomena are usually expressed by means of parametric relations, often linear, and are inserted into the equation of transport in order to predict the distribution of radionuclides along flow paths into aquifers. Therefore the general equation for one-dimensional advective transport in a porous medium for an isotope I with a molar concentration I_w and parent P with P_w at any distance x is

$$\frac{\partial I_w}{\partial t} + v_w \frac{\partial I_w}{\partial x} = b w_I I_r + b \epsilon_I \lambda_P P_r + I_{ads} k_{-1}^I + f_I \lambda_P P_{ads} + \lambda_P P_w - Q_i I_w - \lambda_I I_w - k_1^I I_w \quad (1.1)$$

where λ_I and λ_P are the nuclide and parent decay constants, b converts the concentrations of weathered rock to those in water, in porous rocks it is $b = (1 - n)\rho_r/n\rho_w$. The terms on the left side represent the concentration variation with time in a point x of the flow line and the advection term which is the net flux of I to a location x . There is generally more adsorbed U,Th, and Ra than in the solution, therefore the production by parent decay is greater from the surfaces than in the solution.

We are not interested in solving this equation, but our goal is comprehending the typical behavior of the elements of our interest in order to interpret time series data. In particular, with the aim of identifying possible geodynamical signals related to seismic activity, a deep understanding of the dominant processes that may supply or remove each element is required.

In figure 1.4 the processes involved for each element subject of this study are shown.

For ^{238}U , the advection term is important just until a constant value is reached, with a balance between weathering and precipitation; no general assumption can be made for adsorption; input by weathering from the vadose zone is another contribution to be taken into account [8].

Unlike ^{238}U , the dominant process for ^{234}U is recoil. Clearly not direct recoil, ^{234}U being the product of a β -decay, but recoil of ^{234}Th from the host aquifer rock and from the adsorbed pool.

^{226}Ra is affected by all the processes of water-rock interaction. Input by weathering may be neglected, while adsorption is likely to be the dominant process.

^{222}Rn is a non reactive noble gas, so it does not precipitate or adsorb, it is completely dissolved in water and it can be directly measured. The only two processes affecting its concentration in ground water are recoil from the aquifer host rock and production from the mobile radium pool.

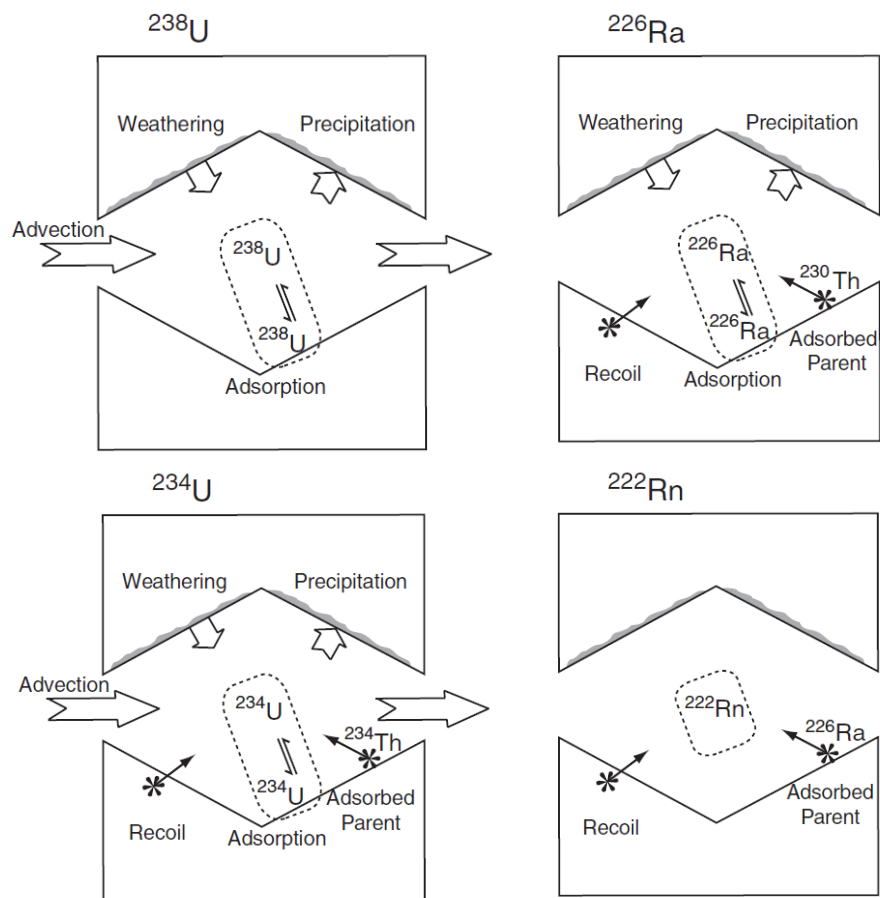


Figure 1.4: The important fluxes for each nuclide are shown. The surface and groundwater populations can be considered individually, or together as the mobile pool. [11].

Chapter 2

Methodologies

2.1 Inductively Coupled Plasma Mass Spectrometry

Mass spectrometry (MS) can be considered one of the most widespread and precise techniques used in analytical chemistry. Due to its peculiar features it found many applications, ranging from inorganic to organic chemistry, from elemental to molecular characterization of unknown compounds. These characteristics include the ability to precisely identify and measure (quantitatively) almost all elements in the periodic table. This technique can also measure individual isotopes of the analyte elements allowing many useful applications, for examples: isotope ratio determination and isotope tracer studies. An equally important characteristic is the ability to detect and measure concentrations at very low levels from 10^{-9}gg^{-1} down to 10^{-15}gg^{-1} .

In principle this technique consists in atomizing and successively ionizing a sample, the ions so produced are transferred to a mass analyzer where they are separated according to their mass and then detected. A mass spectrometer can be schematized as follow:

- Sample introduction system
- Source
- Mass analyser
- Detector

Each of these parts can be realized using different methodologies, but we focused on those adopted in the instrument provided by Gran Sasso national

laboratories. Chemistry and chemical plants service at LNGS is equipped with a Thermo Scientific Finnigan Element 2, which uses a plasma torch as source, hence the technique name Inductively Coupled Plasma Mass Spectrometry (ICP-MS).

2.1.1 Sample introduction

A sample, usually in the form of an acidified aqueous solution ($2\%HNO_3$), is introduced in a nebulizer by a peristaltic pump. The nebulizer perform the function of converting liquid samples to an aerosol, by passing through an orifice the liquid sample and a gas flux. The nebulization process creates a population of droplets with a distribution ranging from a mean diameter of about 1 to 80 μm . Larger droplets require more energy to evaporate and to atomize, resulting in local instability of the plasma, reflected on the measured ion currents of the analyte elements. So the narrower the size distribution the more precise the results of the subsequent analytical determinations [16]. A spray chamber is used to accomplish this separation with respect to the droplets diameter. There are several of these devices, the common principle being that the larger droplets are eliminated, while the smaller ones are transported trough the system in the plasma torch.

In this phase the choice of the carrier gas is crucial, argon gas is usually used because: it is inert, inexpensive, available with a high purity grade and it has a first ionization potential (15.76 eV) higher than that of most elements, while lower than the second ionization potential of almost all elements. This condition enables an efficient first ionization, limiting formation of doubly charged species, as shown in figure 2.1.

2.1.2 Source

Plasma torch

Inductively coupled plasmas are formed by coupling the energy produced by a RF generator to the support gas with an electromagnetic field. In a load coil an alternating current field is created that oscillates at the frequency of the RF generator (27 MHz). The first electrons, generated from the spark of a Tesla coil, are accelerated and oscillate, colliding with neutral gas atoms, thus creating an ionized medium.

The term torch indicates a device used to contain and shape the plasma. Torches can be made of materials such as ceramics or quartz. A typical quartz torch consists of three concentric tubes, as shown in figure 2.2. Between the outer and the centre tubes, the coolant gas (argon) was introduced to separate

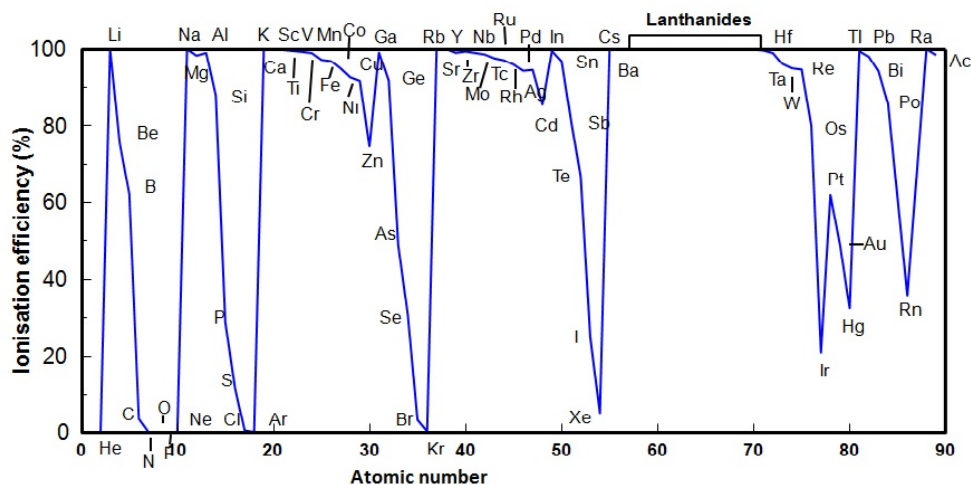


Figure 2.1: Ionizing efficiency vs atomic number, considering a temperature of 6680K and an electron density of $1.47 \times 10^{14} \text{cm}^{-3}$. [17]

plasma from the quartz wall and to shape it in the typical form (figure 2.2). The centre tube injects the aerosol into the plasma. The remaining tube is used for introducing an auxiliary flow of argon gas.

Inside the plasma the temperature can vary between 5000 and 10000 K, depending on the zones, passing through these a sample is vaporized, decomposed, atomized and lastly ionized.

Interface and ion lenses

The function of the interface is sampling the ions produced in the ICP and transporting them into the mass spectrometer. This action requires the use of two or more concentric metal cones. The outer one, called *sampler* or *extraction cone*, has an orifice diameter of $\sim 1\text{mm}$, placed on the terminal part of the plasma. Ions, passing through this orifice, form an ion beam. An additional cone, called *skimmer*, with an orifice diameter $< 0.5\text{mm}$, is positioned behind the skimmer cone to focus the ion beam.

In this region the pressure is reduced by a dual vacuum pumping system from atmospheric to working pressure. In the first stage, between the sampler and the skimmer cone, a mechanical vacuum pump reduces the pressure to $\sim 330\text{Pa}$. The second stage of interface, behind the skimmer cone, reduces the pressure to $\sim 10^{-3}\text{Pa}$ by means of a turbomolecular pump. A representation of this region is reported in figure 2.3.

As the ion beam passes through the interface, it is attracted by a negatively charged electrode into the electrostatic lens assembly, that is a series

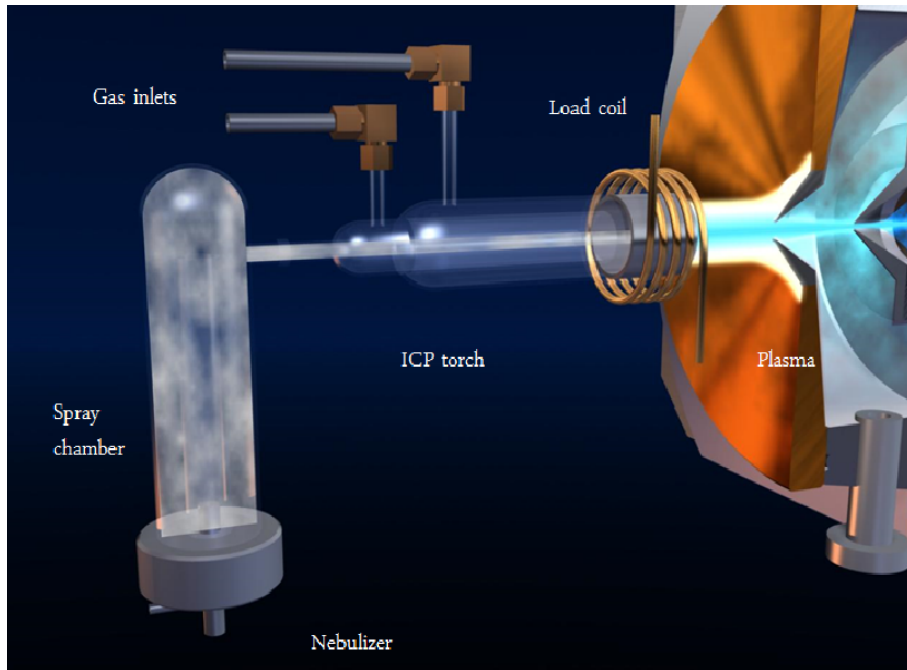


Figure 2.2: Introduction system and plasma torch main components. Agilent Technologies 7500a

of cylindrical electrodes. This assembly further focuses the ion beam. The first component of the series often consists of a metal disk called photon stop, mounted after the exit of the skimmer cone in order to stop the neutral radiation, while ions are deflected around it and refocused behind it. Eliminating this component of the signal significantly lowers the background noise [16].

2.1.3 Mass spectrometer

The mass spectrometer is a mass filter designed to separate ions of a specific mass to a charge ratio ($\frac{m}{z}$) from the multi ion beam. Subsequently individual ion beams are directed to a detector where their current is measured. The presence of a specific $\frac{m}{z}$ allows for a qualitative identification, while the magnitude of the ion current enables a quantitative measurement of the analyte concentration. Several types of mass spectrometer exist, each using a different mass separation principle, including quadrupole, magnetic, time-of-flight and ion-trap. A double-focusing mass spectrometer, like the one at LNGS, is described below.

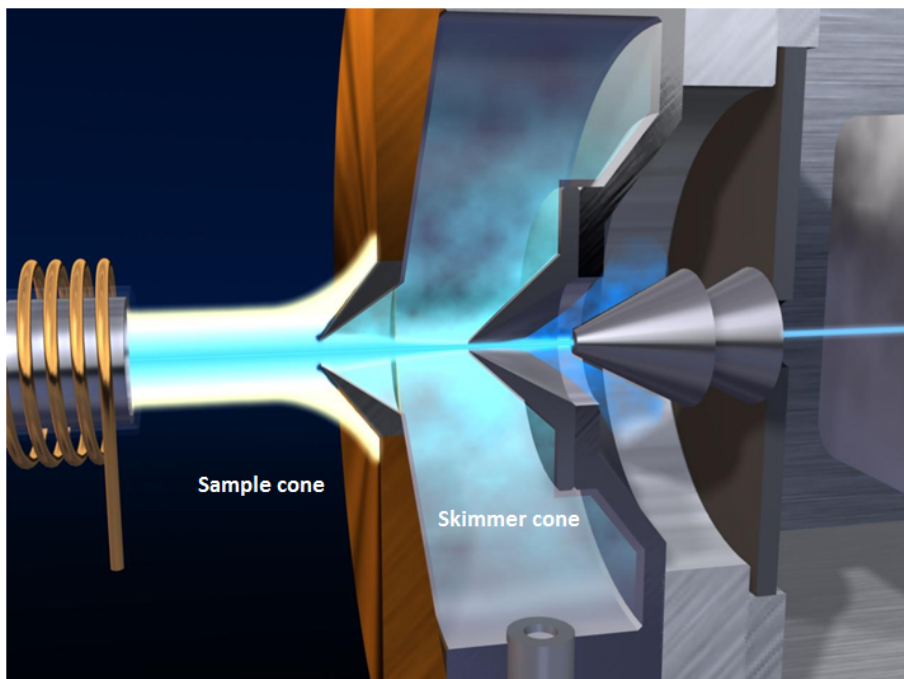


Figure 2.3: Interface and ion lenses main components. Agilent Technologies 7500a

Double focusing

A double focusing or double sector mass spectrometer is obtained combining a magnetic sector mass analyser with an electrostatic analyser. When the electrostatic sector is positioned after the magnetic one, the configuration is called reverse Nier-Johnson geometry. A simplified schematization is reported in figure 2.4

As mentioned above, the magnetic sector divides ions with respect to their $\frac{m}{z}$. This selection is performed accelerating an ion beam by a constant voltage V ; conserving energy it is obtained:

$$\frac{1}{2}mv^2 = zV \quad (2.1)$$

Within this sector, a constant magnetic field B is generated so that the magnetic field lines of force are perpendicular to the flying path of the ion beam, therefore the Lorentz force can be written as:

$$\vec{F}_L = z\vec{v} \times \vec{B} = zvB \quad (2.2)$$

the Lorentz force effect is to deflect ion beams, the radius of curvature r of

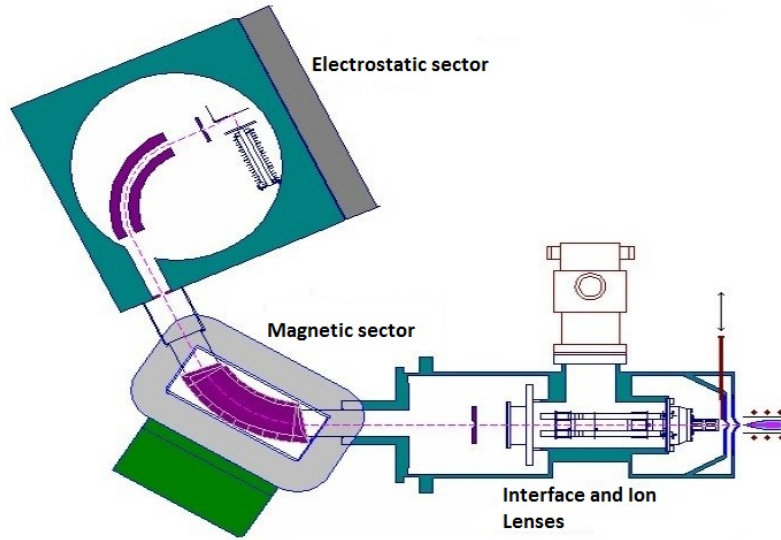


Figure 2.4: Thermo Scientific Finnigan Element 2: a simplified scheme. Element 2 Operating Manual

an individual $\frac{m}{z}$ ion beams can be obtained by the second law of Newton:

$$r = \sqrt{\frac{2Vm}{z} \frac{1}{B}} \quad (2.3)$$

An electrostatic analyser, a curved flight tube through an electrostatic field, is used to filter ions according to their kinetic energy, irrespective of their mass to charge ratio [16]. Passing through it, they travel in a path of radius r such that the electrostatic force and the centrifugal force are balanced:

$$\frac{mv^2}{r} = Ez \quad (2.4)$$

Where E is the electric field strength.

2.1.4 Detector

In Thermo Scientific Finnigan Element 2 the detector is a discrete dynode electron multiplier. It consists of a series of individual dynodes, metal plates, to which a higher dc potential is always applied. Therefore electrons, emitted in the collision between an ion and the first plate, will be accelerated toward the second plate and collide with it. As a results of the collision of each primary electron, two or more secondary electrons will eject from the second

plate and accelerate toward the third plate, and so on in a cascade process. This way an electrical current proportional to the number of ions striking the first dynode is measured. A detector of this type has typical values of amplification around 10^6 .

This device can work in two different modes: *digital* and *analog*. In *digital* mode a voltage difference of $3kV$ is applied at the ends of the device, achieving a gain of $\sim 10^8$, which enables the system to generate an impulse for each ion. Saturation and dead time have to be considered. In *analog* mode a lower potential is applied, consequently a lower gain is achieved $\sim 10^3$, therefore the number of incident ions is proportional to the generated current intensity and the dead time can be neglected. The detector provided with the equipment is capable of automatically changing the acquisition mode depending on the ions flux on the first dynode.

2.1.5 Quantitation

As mentioned above the output analyte signal of the detector is linked through a series of steps to the analyte concentration in the initial sample. There are several different strategies to estimate this relation and quantifying the initial analyte concentration. In this paragraph the most fundamental approach, that is the use of an analytical calibration curve is briefly described. This curve establishes a functional relationship between the analyte ion current and the known concentration of carefully prepared calibration standards, obtained by gravimetric dilution of a commercially available calibration standard solution. For the highest accuracy, the calibration curve should be constructed so that the unknown sample concentration value is placed between two standards [16]. In order to produce a calibration equation for each element of interest, a statistical least square regression fit of the data is performed. The goodness of the regression is used as a measure of the reliability of the calibration.

2.1.6 Interferences

The term interferences means all the effects that can alter the ion current of a specific analyte. In principle this alteration can be positive or negative, the first one being by far the most frequent. Interferences can be classified in two basic categories:

- **spectrometric interferences** resulting in a positive error on analyte ion current measurement. There are four different origins:

- isobaric interferences: generated from the overlapping of isotopes of different elements with the same $\frac{m}{z}$, i.e. the same atomic mass, for example $^{64}\text{Zn}^+$ and $^{64}\text{Ni}^+$ or $^{40}\text{Ar}^+$, $^{40}\text{K}^+$ and $^{40}\text{Ca}^+$.
 - polyatomic molecular interferences: formed in the plasma or in the ions beam, the most common molecular ions observed, consist of atoms from the plasma support gas $^{40}\text{Ar}_2^+$ or $^{40}\text{Ar}^{36}\text{Ar}^+$, atoms from the solvent that is introduced into the plasma ArO^+ and ArOH^+ , and atoms from the major components of the sample matrix.
 - doubly charged ions: these interferences are due to elements which have sufficiently low ionization potential to form doubly charged ions, these ions will appear in the mass spectrum on the element of mass $m/2$.
 - instrumental background
- **nonspectrometric interferences** are generated by various chemical and physical effects, that can seriously affect the measurement accuracy. These can originate from multiple sources and vary with the instrument used, so they can be difficult to identify and correct. They are classified into two main groups:
 - matrix effects: this term refers to a suppression of the ion current of analyte species due to the high concentrations of a matrix constituent. The reason for this is not well understood; however, it is thought to be a combination of ionization properties and space charge effects due to the ion lenses. The effect amplitude depends on the absolute amount of the matrix elements rather than the relative proportion to the analyte element.
 - physical effects: this category includes those effects due to the influence that a sample can have on the instrumental devices, for example, a high dissolved solids content in the sample could bring a drift in analyte ion current signals, related to the buildup of salts on the orifice of the sampler cones.

Generally the first type of interferences can easily be eliminated increasing the resolving power; if this could not be possible or if a matrix effect is present, interferences are eliminated by a chemical pretreatment of the sample.

The term resolving power R means the capacity of the instrument to resolve two adjacent peaks in the mass spectrum, and it is defined as:

$$R = \frac{\bar{M}}{\Delta M} \quad (2.5)$$

where ΔM is the distance between the two peaks and \bar{M} is their mean mass. Two peaks are considered resolved if the magnitude of the valley between the peaks (Y_v) is less than 10% of the mean magnitude of the height of the peaks (\bar{Y}) [16]:

$$Y_v < 0.1\bar{Y} \quad (2.6)$$

The Finnigan Element 2 is able to operate on three fixed level of resolution:

- low $R = 300$
- medium $R = 4000$
- high $R = 10000$

2.2 Liquid Scintillation Counting

Liquid scintillation counting (LSC) has been one of the first and still widely used technique for the quantitative measurement of radioactivity. Due to the ability to detect principally alpha and beta particle, but also weak gamma, x ray, and Auger electron, it found many applications from the low-level environmental radioactivity to the high-level radioactivity used in the radioisotope applications. LSC in environmental studies is used especially in the quantification of pure β -emitters as ^{14}C or ^3H .

This section deals with a brief description of the technique, focused on the highlight of the peculiar problems of its application to a low-level environmental measurement.

2.2.1 Liquid Scintillation

Regardless of its aggregation state and of its nature, organic or inorganic, a scintillator is based on a physical process known as fluorescence. That is the prompt emission of visible radiation from a material following its excitation by the interaction with a particle, charged or not. This light is converted in a current signal by a photomultiplier. In general a scintillator should have some appreciable characteristics: a high efficiency in converting kinetic energy into detectable light, this conversion being linear and fast.

In LSC a liquid organic scintillator is used, precisely a scintillation cocktail is a solution composed of: the organic solvent, the organic scintillator and a surfactant [18]. The surfactant enables the acceptance of water samples with loads exceeding 50%. After the sample is placed into the scintillation cocktail to form a homogeneous counting solution, the first process to take place is the interaction of the decay products with the solvent. This is an

organic aromatic compound like: pseudocumene, linear alkylbenzene or diisopropylnaphthalene (DIN). The energy released in the decay is accepted by the solvent molecules and brings them in an activated state [19], which transfers their energy to the organic scintillator or fluor, such as diphenyloxazole (PPO). These organic compounds have a structure known as π -electron, the energy levels of such a molecule are shown in figure 2.5.

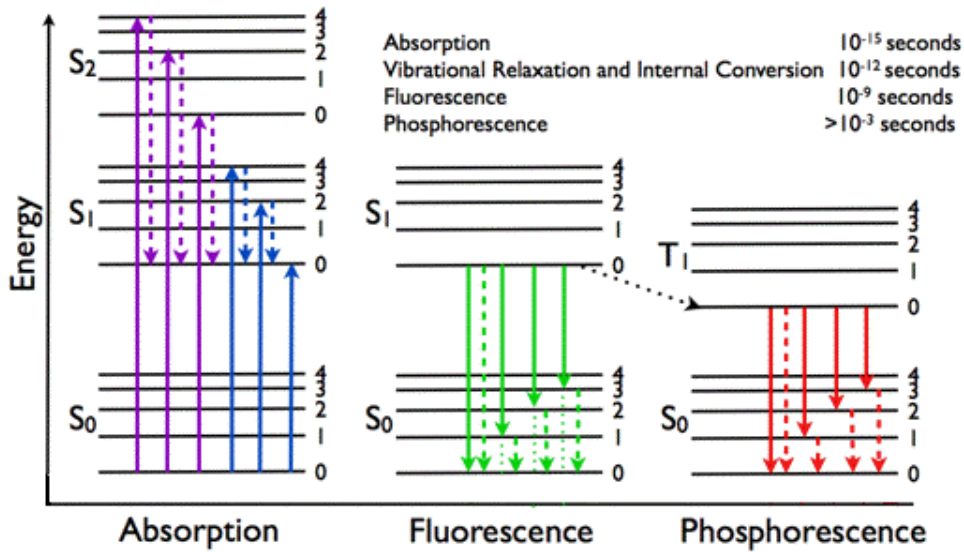


Figure 2.5: Jablonski diagram representing energy levels and possible transitions. Solid arrows indicate radiative transitions as occurring by absorption or emission. Dashed arrows represent non-radiative transitions. Image taken from <http://www.photobiology.info/Visser-Rolinski.html>

An electron from the ground state S_{00} , absorbing energy, is quickly ($10^{-15}s$) excited to a higher singlet state and consequently de-excited ($10^{-12}s$) to the S_{10} via non-radiative transitions known as internal conversion and vibrational relaxation. The subsequent transition between this S_{10} state and a S_{0i} state emits prompt visible light, known as fluorescence ($10^{-9}s$), in a typical wavelength range from 375 to 430 nm. There is another possible transition, called intersystem crossing, between the singlet S_{10} state and the triplet T_{10} state with a consequential de-excitation to the S_{0i} state with emission of radiation known as phosphorescence ($> 10^{-3}s$).

As illustrated in figure 2.5, the emission transitions have lower energy than the adsorption ones with a very little overlap between the spectra, therefore the medium is almost transparent to its own emission wavelength, this phenomenon is called Stokes shift[20]. The emission wavelength depends on the

scintillator, while intensity depends on the energy and type of particle. In the literature [19] it is reported that an α -particle produces a light intensity about ten times lower than a β -particle of the same energy, and that the pulse decay time of the light emission from an α -particle can be about $35 - 40ns$ longer than that produced by a β -particle.

2.2.2 Photomultiplier

A photomultiplier (PMT) is a device capable of converting light photons to electrons. A PMT simplified scheme is shown in figure 2.6. The device is enclosed in glass in order to sustain vacuum that allows an efficient electron acceleration.

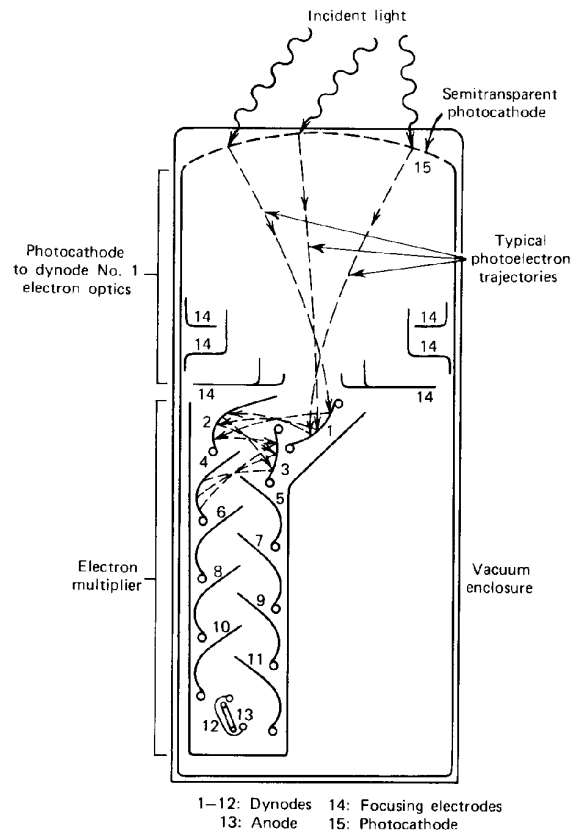


Figure 2.6: Principal components of a photomultiplier [20].

The device consists of two major components:

- **photocathode:** usually, a bialkali thin layer that adsorbs incident photon and emits an electron by photoelectric effect. The quality of

the conversion is quantified by a simple unit, the quantum efficiency (QE), defined as

$$QE = \frac{\text{number of photoelectron emitted}}{\text{number of incident photons}}$$

typical QE values are of 20-30% [20].

- **electron multiplier:** based on the secondary electron emission. Photoelectrons emitted from the photocathode are accelerated and focused so as to strike on the first electrode (dynode) where electron multiplication takes place by secondary emission. This secondary emission is repeated at each of the subsequent dynodes resulting in clusters of electrons multiplied by 10^6 to 10^7 times or more being collected by the anode.

2.2.3 Interferences in Liquid Scintillation Counting

In LSC the term interferences indicates all phenomena that can generate counts in the energy window of the radionuclide of interest, not due to the decays of the radionuclide itself, or that can cause a loss of counting efficiency. Six major causes of interference can be identified[19]:

1. **background:** defined as counts originating from radiation external to the sample, such as cosmic radiation, environmental radioactivity due to the construction materials and to the surroundings and from instrumental noise. Background can be quantified measuring a blank solution with the same composition and quench of the sample with the exception of the radionuclide of interest and then subtracting the blank count rate from the sample one.
2. **quench:** the term encompasses all causes that can lower the conversion efficiency of energy in light pulses and in the detection of these by the photomultiplier. Two causes can be identified:
 - **chemical quench:** it is caused by a chemical substance in the sample that absorbs energy, preventing energy transfer between decay products and solvent or between solvent and scintillator.
 - **color quench :** whether the sample is colored, it induces a variation of optical properties of the scintillation mixture, i.e. some photons produced by the scintillator are adsorbed before they reach the photomultiplier.

In both cases, the count rate, normally expressed in counts per minute (CPM), is lowered. In order to determine the actual activity of the sample, expressed in DPM or disintegration per minute, and correct quench effect, the evaluation of the counting efficiency is needed. This is defined as:

$$efficiency\% = \frac{CPM}{DPM} \times 100 \quad (2.7)$$

the decrease of efficiency is higher for low energy decay products, for example 3H sample, with optimized measurement parameters, has an efficiency of 20-30%, while α particles reach almost 100% [19, 21].

3. **radionuclide mixtures:** this interference appears when the energy spectra of two or more radionuclides overlap. This always happens in the presence of β -particles which produce continuous spectra from 0 to E_{max} . Several methods exist to quantify the separate radionuclide activities, but in the case of 3H chemical separation by distillation is performed.
4. **luminescence:** it is due to the energy adsorption and subsequent emission of photons in the scintillation cocktail, not originated by nuclear radiation. It can be of two types:
 - photoluminescence: it consists of a single photon emission process that takes place when the scintillation mixture has been exposed to ultraviolet light. The effect lasts for few minutes, so waiting 10-15 min to start counting after the sample has been put inside the instrument can easily eliminate this effect.
 - chemiluminescence: it is the production of light by single photon emission due to chemical reactions. These reactions often occur when the sample is mixed with the scintillation cocktail, for example when the PPO cocktail is mixed to a basic solution (pH 8-14).
5. **static:** electrostatic discharge, due to charge accumulation on the plastic vials, can cause photons production.
6. **wall effect:** the organic solvent can penetrate the plastic vial walls and cause an alteration of the quench parameters; this effect is not present for DIN based cocktail[22].

2.2.4 Equipment

Gran Sasso National Laboratory are equipped with a spectrometer QUANTULUS 1220 (Perkin Elmer). This instrument was designed and built to enhance the measurements of low-level activity concentrations, in particular of pure β emitters such as 3H and ^{14}C .

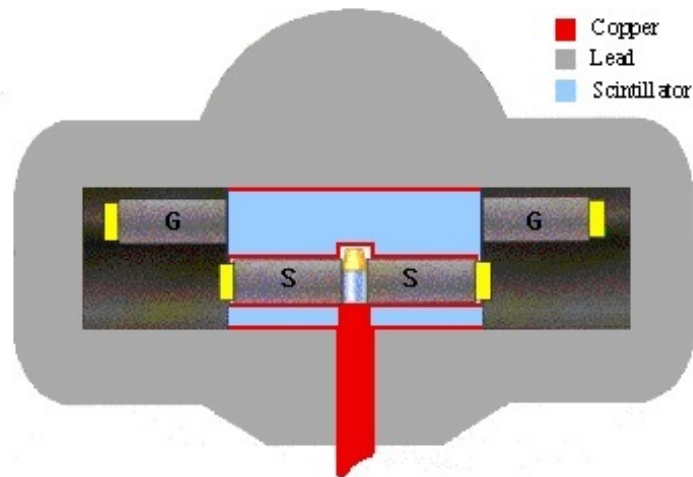


Figure 2.7: A scheme of the detector. <http://c14dating.com/quant.html>

A scheme of the detector is reported in figure 2.7: the detector consists of two PMT (S) equipped with diodes for automatic stabilization of the spectrum. The two PMT work in coincidence mode discriminating photons emitted in the scintillation cocktail by a particle interaction from self-emission by a single photomultiplier and from a single photon emission process such as luminescence.

Lowering external background is a fundamental task for low-level activity measurement. The shield from external radiation is made of a passive component that is an asymmetric radiation shield made of low radioactivity lead. The active part consists of two PMT (G) guarding a batch of scintillation cocktail optically isolated from the detector PMT (S). The guard photomultipliers work in coincidence mode to detect external radiation and in an anti-coincidence mode with respect to the detector photomultipliers to subtract the events from the sample spectrum. The instrument is placed in the underground laboratory where the thickness of the overburden rock is 1400 m, equivalent to 3100 m of water. This is a great further benefit for reducing the external background [23, 24].

Quench evaluation, monitoring and correction are performed by an external-standard method [19, 21], using a low activity 37 kBq ^{152}Eu source.

Chapter 3

Measurements

3.1 Tritium measurements

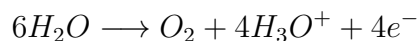
The natural concentration of 3H , around 5-10 TU in the northern hemisphere, makes a measurement of activity concentration in the water sample without pre concentration very complicated, if not impossible. Nowadays it is still widely used a measurement method, developed in the 1970s, that consists of two main phases [25, 26, 27, 28, 29, 30, 31, 32, 33, 34, 35, 36, 37, 38, 39, 40]:

1. tritium preconcentration in water sample via electrolytic enrichment
2. activity concentration measurement using Liquid Scintillation Spectrometry or LSC

3.1.1 Electrolysis of water

Electrolysis of water is the decomposition of water into hydrogen and oxygen gas due to the passage of electric current in an electrolytic cell consisting of two electrodes placed in the water and connected to a current generator. The current dissociates water molecules in OH^- and H_3O^+ ions.

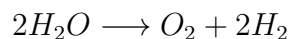
At the anode (positive pole) an oxidation reaction takes place:



At the cathode (negative pole) electrons from the anode give rise to a reduction reaction:



Combining the two half reactions



If the reaction were to take place in pure H_2O , the passage of electric current would be prevented by the accumulation of H_3O^+ cations at the cathode surface, and of the OH^- anions at the anode surface and the process would be very slow.

This problem is solved by adding a soluble electrolyte to the solution to increase conductivity, indeed its dissociation in anion and cation compensates the charge of H_3O^+ and OH^- , avoiding charge repulsion and facilitating electric current flow.

The choice of the electrolyte is crucial because the anions and cations that are introduced may compete with the process of water electrolysis. In order to avoid this situation, during the electrolytic enrichment run, Na_2O_2 is added as electrolyte.

The whole process follows the Faraday's law of electrolysis

$$Q = M_W F \quad (3.1)$$

so the electrolyzed water mass M_W is proportional to the charge given to the system Q by the Faraday's constant $F = 2.975 Ahg^{-1}$.

3.1.2 Electrolytic enrichment

The Electrolysis of water was used to concentrate tritium, because the HTO molecule has a slightly higher binding energy than H_2O and DHO , so it is disadvantaged in the dissociations in an electrolytic cell; this process is known as electrolytic enrichment.

The procedure consists of putting a water sample in an electrolytic cell and giving it a fixed amount of charge. The dissociation of water in gaseous H_2 and O_2 reduces the sample volume to a fraction of the initial one. The isotopic fractionation, due to the difference in binding energy, allows to concentrate nearly 90% of the HTO in the remaining water [19].

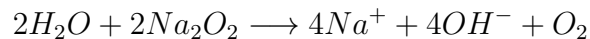
The ability to concentrate HTO molecules instead of H_2O and DHO ones, called separation factor, depends critically on the catalytic property of the materials which the cells are made of. Among the metals that exhibit a high separation factor, there are stainless steel and iron which are, respectively, the anode and the cathode of the cells supplied to the Gran Sasso National Laboratory [27].

The enrichment procedure can be divided in the following steps [31]:

- **distillation of water samples** Initial distillations aim to eliminate solid impurities, and to reduce the electrical conductivity of the samples. It is normally preferable to bring distillation to dryness in order

to avoid isotopic fractionation [29]. At the end of this step the electrical conductivity of the samples is checked: it has to be below $50\mu S cm^{-1}$ to be considered negligible.

- **weighing of cells before electrolysis** First of all the empty cells are weighed, then they are filled with 500 mL of water sample mixed with (1.5 ± 0.05) g of Na_2O_2 . During the dissolution Na_2O_2 reacts with water giving

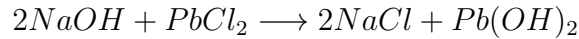


In the reaction gaseous oxygen is released with a not negligible loss of weight. The reaction is rather slow, for this in [30] a correction to the initial mass of the sample is performed. In the calculation this correction is not taken into account, because from the dissolution to the pouring in the cells a 12 hours time intervals occurs, therefore the reaction can be considered at equilibrium. The solution is made up to volume. The addition of a fixed amount of electrolyte homogenizes the conductivity between samples. At the end of this phase the filled cells are weighed again.

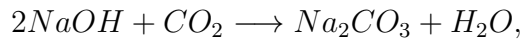
- **electrolysis of water sample** In this step the cells are connected in series to a current generator so that, at the end of the process, the same charge is given to each cell. Following the Faraday's law of electrolysis, the electrolysed water mass is proportional to the total charge given to a cell. In a real electrolytic cell evaporation takes place too. In order to control, homogenize and minimize evaporation, cells are put in a refrigerator with an operational temperature range of $-2 \div 2^\circ C$. When the water sample in the cells is about half of the initial volume, the electrolytic enrichment is stopped and three cells are weighed. Knowing the charge given to the system, it is possible to estimate an *effective Faraday's constant* C' for the enrichment run. Starting from this value, the electric current to be given to the system to obtain the desired final water mass in the cells is calculated. Once the estimated charge value is reached, the system is shut down.
- **weighing of cells after electrolysis** The cells are weighed again. The three weighings allow to calculate the initial and final water masses.
- **neutralization and distillation of water samples after enrichment** In this phase the electrolyte, introduced after the initial distillation, is precipitated by neutralisation and eliminated by distillation in

order to avoid chemiluminescence and quench effects in the scintillation mixture.

In literature two possible neutralization reactions are reported. The first and most adopted [27] is



the latter



in principle, allows for the highest tritium recovery, converting hydrogen into $NaOH$ in water [28]. Then samples are fluxed with gaseous CO_2 precipitating Na_2CO_3 , that is eliminated by distillation. At the end of this phase the pH of each solution is measured and registered, if the value is above 7 the process has to be repeated.

- **preparation of the scintillation mixture** In this phase, 10 mL of aqueous solution and 10 mL of scintillation cocktail are mixed in a 20 mL plastic vial. The choice of the type of vial and of the 1 ÷ 1 ratio between volumes shows the best performance[41].

The entire procedure, called electrolytic enrichment run, is performed on a batch of 20 almost identical cells. In order to make reproducible measurements, all the parameters of a run are controlled and made as homogeneous as possible, for example: the constructive features of the cells, the operating temperature and the electrical conductivity of the samples.

At the end of each electrolytic enrichment run 26 vials are prepared: 15 unknown samples, 3 spikes, 2 blank solutions (called Dead Water) that constitute the enriched solutions and 2 standards, 2 spikes and 2 blank solutions that are the not enriched part of a run.

The term dead water (DW) indicates a water with negligible tritium concentration, taken from isolated aquifers. The term spike means an aqueous solution with a concentration of tritium higher compared to the samples, but not necessarily known with high precision; this characteristic differentiates a spike from a standard, that is an aqueous solution with a concentration of the tritium higher than the samples, known with the greatest precision possible.

The role that each of these has in the final quantification of tritium concentration activity of the samples will be explained in the following two paragraphs.

3.1.3 Contamination

The intrinsic characteristics of tritium (gas, ease in forming *HTO*), combined with the ubiquitous presence of water vapour in the atmosphere, together with the capacity of all the surfaces to adsorb water in traces, make contamination a problem to be taken into account during the entire procedure. Two categories of contamination can be distinguished:

- memory effect due to the sample previously treated in the electrolysis and distillation apparatus
- contamination due to the exchange with the atmosphere or with other sources of tritium during the entire process.

The first effect can be minimized, if not completely eliminated, through proper and conscientious washing and drying of the entire equipment used.

As far as the contamination by exchange with the atmosphere is concerned, it is reduced by minimizing the contact between the samples and air, by using bottles with sealing plugs during storage, hydraulic guard during distillation and film layers in transport. Moreover the sources are kept in separate rooms from the samples and the DW.

Cross-contamination between different solutions in the pouring passages is avoided following a sequence with increasing activity such as DW-samples-spike.

However to take into account all the possible effects mentioned above, for each run two samples of dead water are submitted to the entire enrichment process and then measured. If their count value deviates from that of the not enriched dead water, using it as a new background will eliminate the effect of contamination.

3.1.4 Tritium activity concentration

The activity concentration in the enriched samples can be calculated, as reported in literature[27, 30, 28], using

$$A_T = \frac{N_{SA}A_{ST}}{N_{ST}Z_I} \exp(-\lambda t) \quad (3.2)$$

where:

N_{SA} is the net count rate of the sample

N_{ST} is the net count rate of the standard

A_{ST} is the activity concentration of the standard (Bq/kg)

$\lambda = (1.5403 \pm 0.0027) \times 10^{-4} d^{-1}$ is the tritium decay constant

t is the time elapsed between the sampling date and the measurement date.

Z_I tritium enrichment factor for the given sample

the equation (3.2) is valid if we consider the sample and the standard masses equal, and if both are measured under the same conditions. As it can be seen from (3.2), the standard, being a source of known activity, has the function of evaluating the counting efficiency of the instrument, which is extended de facto to all samples. This extension is justified by the assumption of constant quench level in the different solutions. The goodness of this assumption is tested, measuring and evaluating an external standard.

The net counting rates, for samples and standards, are defined as the gross counting rate to which the background obtained by counting dead water is subtracted:

$$\begin{aligned} N_{SA} &= N_{GSA} - N_B \\ N_{ST} &= N_{GST} - N_B \end{aligned}$$

where N_{GSA} , N_{GST} and N_B are the gross counting rate of sample, standard and background, defined as:

$$\begin{aligned} N_{GSA} &= \sum_{i=1}^n \frac{N_{GSAi}}{n} \\ N_{GST} &= \sum_{i=1}^m \frac{N_{GSTi}}{m} \\ N_B &= \sum_{i=1}^k \frac{N_{Bi}}{k} \end{aligned}$$

where:

n, m, k number of individual measurements of the sample, standard and background in the given run, respectively.

$N_{GSAi}, N_{GSTi}, N_{Bi}$ individual (gross) count rates for the sample, standard and background, respectively, in the given measurement run.

The enrichment factor Z_I , defined as $Z = C_f/C_i$, that is the ratio between initial and final concentration of tritium in the sample, deserves a more detailed explanation.

Enrichment parameter

The relationship between the electrolytic enrichment factor and the mass reduction of the sample is given by [27, 28]:

$$Z = \frac{C_f}{C_i} = \left(\frac{W_i}{W_f} \right)^{EP_{eff}}$$

where W_i and W_f are initial and final water masses, W_i/W_f is, therefore, the reduction in mass of the sample and EP_{eff} is known as effective enrichment parameter.

The effective enrichment parameter EP_{eff} takes into account the processes by which the water mass inside the cell is reduced, that are: electrolytic dissociation and evaporation loss, and is therefore linked to the separation factors of individual processes according to:

$$EP_{eff} = r_e \left(1 - \frac{1}{\beta} \right) + r_v \left(1 - \frac{1}{\beta_v} \right) \quad (3.3)$$

where β and β_v , r_e and r_v are the separation factors and the water mass reductions respectively, relevant to electrolysis and evaporation. r_e is the ratio between the mass of electrolyzed water, obtained from (3.1), and the total mass lost. If spraying can be overlooked $r_v = 1 - r_e$.

For an enrichment system such as the one in use at LNGS, the second term of the second member of (3.3) is of the order of 0.5% of the first term, and, if all cells operate under the same conditions, its variation from cell to cell is negligible. Moreover equation (3.3) suggests that a set of cells with uniform β should show a uniform value of EP_{eff} in an enrichment run. Therefore, the parameter EP_{eff} is used to monitor the performance of a set of electrolytic cells.

In the routine run it is impossible to obtain uniform evaporation and spraying losses for all cells, despite, being connected in series, they undergo the same current flow.

This is why the cells are weighed and EP_{eff} is calculated according to:

$$EP_{eff} = \left(\frac{W_i - W_f}{W_e} \right) \frac{\ln Z}{\ln \left(\frac{W_i}{W_f} \right)} \quad (3.4)$$

where W_e is the electrolyzed water mass, calculated using Faraday's law. W_i, W_f are determined by weighing.

During a run, in some cells spikes are enriched (water samples with a moderate concentration of tritium high enough to obtain a low counting

uncertainty, low enough to avoid contamination problems), for each of which, starting by net counting after and before enrichment N_{SPf} and N_{SPi} , the enrichment factor P_i may be calculated as

$$P_i = \frac{N_{SPf}}{N_{SPi}}$$

Starting from the value of P_i , the effective enrichment parameter for the spike cell taken into account can be calculated using the equation (3.4).

Averaging this parameter of the 3 spike cells for run, we get the value that describes the single electrolytic enrichment run called P . Starting from P the electrolytic enrichment factor for a given cell is calculated according to:

$$Z_I = \left(\frac{W_i}{W_f} \right)^{\frac{PQ}{(W_i - W_f)F}} \quad (3.5)$$

where Q is the total charge given to each cell. Loading spikes in different cells, enables the efficiency monitoring of each cell.

Uncertainties

As shown in the above paragraphs, tritium activity concentration measurement is a complex process consisting of many steps, each of which has several uncertainty sources. Some sources are mathematically quantifiable, while others are not, so that the only way to treat them is trying to minimize them. A complete and exhaustive description of uncertainties assessment for the overall measurement procedure can be found in [30, 31, 42] and it is adopted in this work. In the Appendix A a brief discussion of the principal source of uncertainties is reported.

Referring to equation (3.2), the combined standard uncertainty of the measured quantity A_T can be expressed by the standard uncertainties of the parameters in the equation using the law of uncertainty propagation, that, in case of linear equations of a purely multiplicative form, is:

$$\frac{u(A_T)}{A_T} = \sqrt{\left(\frac{u(N_{SA})}{N_{SA}} \right)^2 + \left(\frac{u(N_{ST})}{N_{ST}} \right)^2 + \left(\frac{u(A_{ST})}{A_{ST}} \right)^2 + \left(\frac{u(Z)}{Z} \right)^2 + \left(\frac{u(D)}{D} \right)^2}$$

where $D = \exp(-\lambda t)$. Considering tritium activity concentration, in our samples between 3 and 10 TU, the dominating uncertainty components are the net count rate one and the enrichment parameter one.

3.1.5 Materials and Results

In order to further clarify the procedure and to show the results obtained applying this technique, a summary of the materials used and the results that were obtained is presented in this paragraph.

Materials

During the electrolytic enrichment procedure an equipment consisting of various glassware, heaters and chillers was used. The Standard Reference Material 4361C with the specific activity of $(2.009 \pm 0.015) Bqg^{-1}$ at 3 September 1998 (NIST, Gaithersburg, Maryland, USA) was used as tritium standard. Tritium spike solutions were obtained diluting a standard of $(4.79 \pm 0.11) kBqg^{-1}$ at 1 October 2013 (PTB, Berlin, Germany). The scintillation cocktail Ultima Gold LLT (PerkinElmer) was used in the preparation of the scintillation mixture.

Results

In the first two columns of table 3.1 values of the fundamental quantities for an enrichment run, explained in this chapter, are reported.

In the third and the fourth columns the LSC acquisition and global parameters are reported. The total acquisition time is divided in three cycle each of which is composed of 5 independent counts sessions (repeats) for each sample, so the duration of a single repeat is of 40 min for samples and backgrounds, while it is of 30 min for standards and spike.

Dividing the total counting time in shorter duration segments is a precaution, that takes into account possible instrumental instability and malfunctioning. On all sample repeats an outliers rejection procedure is performed using a 2σ criterion.

The background and blank signals (DW and DW before enrichment respectively) are coincident, that means no contamination was acquired during the procedure.

In the table 3.1, the counting efficiency ϵ and the figure of merit (FOM) are also reported, the last being a parameter that represents the quality of a measurement, defined as:

$$FOM = \frac{\epsilon^2}{B} \quad (3.6)$$

where B is the background signal. The signal integration window is optimized with respect to this parameter.

Table 3.1: it shows some relevant parameters regarding the electrolytic enrichment procedure and the liquid scintillation counting.

Electrolytic enrichment run parameters		LSC parameters	
Number of cells	20	Cycles	3
Sample	15	Repeats	5
Spike	3	Acquisition time	(min)
DW	2	Samples, backgrounds	600
Initial mass	499.74(2)	Standards, Spike	450
Final mass	20.36(1)	Background signal (CPM)	0.43(3)
Q (Ah)	1402(7)	Blank signal (CPM)	0.44(3)
P	0.885(6)	ϵ (%)	23.75
Mean Z	16.3(2)	FOM	1335

3.2 Radium measurements and new developments

Several analytical radiometric and mass spectrometry techniques have been developed for the analysis of ^{226}Ra in environmental samples: radon emanation [43], liquid scintillation spectrometry [44], alpha-ray spectrometry [45], gamma-ray spectrometry [46], TIMS (Thermal Ionization Mass Spectrometry) [47] and ICP-MS (Inductively Coupled Plasma Mass Spectrometry) [48, 49, 50, 51, 52, 53]. With the exception of ICP-MS, these methods are time consuming, often expensive and therefore not convenient when large numbers of samples are to be analyzed. However, the ICP-MS method has also some drawbacks, above all possible interferences, which could make precise ICP-MS analysis of long-lived radionuclides in the environment rather difficult [54].

The aim of the present work has been to develop a robust technique for ^{226}Ra analysis of groundwater samples collected from the Gran Sasso aquifer (central Italy) ([55]). In order to construct time series of ^{226}Ra concentration and to assess its behaviour, small concentration variations over time need to be appreciated, leading to good count statistics, while using the minimum possible amount of the sample.

Keeping this idea in mind, the literature on the subject was carefully studied and among the various ones the Lariviere et al. (2005)[51] method was chosen, because it presented some very good characteristics and prospects

for improvements. It consists of the sequential application of a cation exchange resin (50W-X8) and an extraction chromatographic resin (Sr-resin). The first one has been widely used to separate ^{226}Ra in liquid matrices [49, 51, 53, 52, 48], while the latter retains Sr and partially Ba cause of the main polyatomic interference in Ra [56, 48]. Every step of the Lariviere procedure was tested in order to check the actual operation of the method and possibly improve it.

Due to the high data precision requirements for the development of the ^{226}Ra groundwater time series, the original Lariviere et al. (2005) method has been modified adding a pre-concentration part, the effects of which were thoroughly investigated.

This work focuses therefore on optimization of separation protocol and on pre-concentration, evaluating in particular related polyatomic interferences and matrix effects that could affect the ^{226}Ra peak window [57].

3.2.1 Extraction Chromatography

Extraction chromatography (EXC) is a particular form of column chromatography, in which the stationary phase is an organic liquid or organic solution impregnating on an inert, usually polymeric, support while the mobile phase consists of an aqueous solution. This technique combines the favourable selectivity features of organic compounds used in liquid-liquid extraction with the multi stage character of a chromatographic process; it is particularly advantageous when micro-amounts are concerned, as in the case of radiochemical separations, and when contamination must be avoided.

EXC is ideally suited to separate radionuclides from a wide range of sample types. Figure 3.1 is a simplified scheme of the three major components of an extraction chromatography system. These are:

- The inert support is usually made from porous silica or organic polymers, ranging in size from 50 to 150 μm in diameter.
- The stationary phase consists of the liquid extractant, which can be either a single compound or a mixture. Diluents can also be used to solubilize the extractant and to increase the hydrophobicity of the stationary phase.
- The mobile phase is an acidic aqueous solution, often nitric or hydrochloric acid; complexants, such as oxalic or hydrofluoric acids, are frequently used to enhance selectivities or the stripping of strongly retained elements from columns.

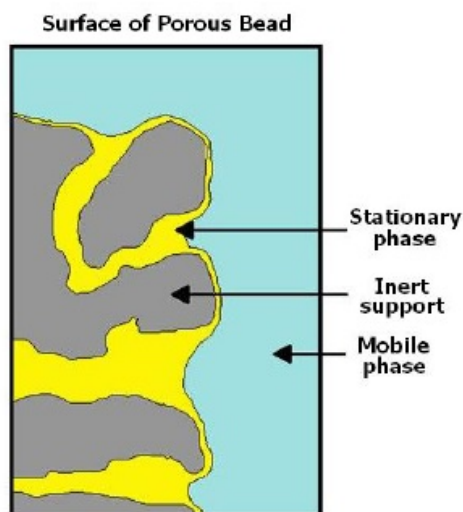


Figure 3.1: Simplified depiction of the three main components of an extraction chromatographic system: inert support, stationary phase and mobile phase. <http://www.eichrom.com/eichrom/products/extraction.aspx>

Traditional solvent extraction systems (SX) are characterized by the distribution ratio D :

$$D = \frac{C_o}{C_{aq}}$$

where C_o and C_{aq} are analyte concentration in extractant organic phase and in aqueous phase respectively, while extraction chromatography systems are characterized by the number of free column volumes to peak maximum, i.e the column capacity factor k' . D is converted to k' according to the formula:

$$k' = D \frac{V_s}{V_m}$$

where V_s and V_m are the volumes of stationary and mobile phase, respectively. (V_m is also defined as Free Column Volume, FCV). k' measures the column uptake ability of the element being considered. For EXC systems D and k' are not usually directly measured, but calculated from the weight distribution ratio D_w , that is the amount of a given metal ion uptaken by a measured weight of resin from a given volume of aqueous solution. D_w can be easily measured.

3.2.2 Ion Exchange Chromatography

In an ion exchange procedure, the counter-ions on the resin are replaced by sample ions that have the same charge. In applications involving a cation exchange resin, such as the AG 50 resin, neutral molecules and anions do not interact with the resin. A resin can be converted from one ionic form to another. Usually the resin is used in an ionic form with a lower selectivity for the functional group than that of the sample ions to be exchanged. The sample ions are then exchanged when introduced, and can be eluted by introducing an ion with higher affinity for the resin or a high concentration of an ion with equivalent or lower affinity.

In general, the lower the selectivity of the counter-ion the more readily it exchanges for another ion of equal charge. The order of selectivity can also be used to estimate the effectiveness for different ions as eluants, with the most highly selective being the most efficient.

3.2.3 Reagents and standards

During the study, deionized water (Milli-Q water system, Millipore, Bedford, MA, USA) and hyperpure hydrochloric and nitric acids (Panreac, Barcelona, Spain) were used. Mono-elemental standard of Ca, Ba, Mg, Sr, Ce, La and Nd (NIST absolute standard, Gaithersburg, MD, USA) in stock solutions were diluted to obtain matrix-matched standards and spikes.

Radium standard and spikes were obtained by dilution from a 100.5Bqg^{-1} STD (PTB, Braunschweig, Germany).

Pre-concentration and separation of ^{226}Ra were performed using two commercially available resins: a strong cation exchange resin (AG-50W-X8) and a crown ether based resin (Sr-resin) (Triskem, Bruz, France).

3.2.4 Equipment

In order to determine ^{226}Ra in ground water samples, a SF-ICP-MS (Finnigan Element 2, Thermo Scientific) was used. It was equipped with an introduction system Apex Q high-sensitivity (Element Scientific Inc.). A spray chamber operational temperature of 100°C and a Peltier-cell condenser operational temperature of 2°C , optimal for aqueous samples, were chosen. The Apex Q system was tested with three different micro-nebulizers: $64\mu\text{Lmin}^{-1}$, $100\mu\text{Lmin}^{-1}$ and $200\mu\text{Lmin}^{-1}$, using a 100pgg^{-1} Thermo Tuning solution and monitoring ^{238}U as descriptive of heavy elements. The results of the tests are reported in table 3.2 below.

Table 3.2: Optimized values of Finnigan Element 2 with Apex Q introduction system.

NEBULIZER 64 μ l	
Sample Gas	0.875
Auxiliary Gas	0.2-0.3
Cps N_2 on	$2 * 10^5$
Signal	stable
NEBULIZER 100 μ l	
Sample Gas	0.875
Auxiliary Gas	0.2-0.3
Cps N_2 on	$4 * 10^5$
Signal	stable
NEBULIZER 200 μ l	
Sample Gas	0.879
Auxiliary Gas	0.25
Cps N_2 on	$2.5 * 10^5$
Signal	unstable

The second one showed the best performance, which means that the 100 μ Lmin⁻¹ shows a higher count rate than the others two with a stable signal, moreover the 100 μ Lmin⁻¹ uptake rate permits working with no more than 0.5 mL samples. .

N_2 flow pressure was noticed not to be crucial to the gain of the system, in the sense that above a certain value, flux variation didn't modify the cps in uranium window. The instrument was optimized with respect to the sample and the auxiliary gas flow, in order to reach maximum sensitivity and stable signal. The acquisition parameters were chosen with an isotopic ratio measurement approach [58], that is a narrow mass window in order to gain in sensitivity and a long acquisition time to improve count statistics. Values are reported in the table 3.3. the 100 μ Lmin⁻¹

3.2.5 Sample preparation

In order to accomplish separation from matrix constituents and from spectral interfering elements, a Lariviere (2005) [51] revised procedure was developed and applied [57]. It consisted of the sequential application of a strong cation

Table 3.3: Optimized values of Finnigan Element 2 with Apex Q introduction system

Instrumental parameters	
Gas flow (L/min)	
Sample	0.875
Auxiliary	0.2-0.3
Cool	16
RF power (W)	1250
Interface cones	Nickel
Acquisition parameters	
Resolution	300
Number of run	3
Number of passes	3
Samples per peak	50
Mass window (%)	40
Integration window (%)	100
Sample time (s)	0.5
Acquisition time (s)	10
Apex-Q parameters	
Spray chamber temperature (°C)	100
Peltier-cell condenser temperature (°C)	2
N ₂	on

exchange resin (AG50WX8) and an extraction chromatographic resin (Sr-resin).

AG 50W strong acid cation exchange resin is composed of sulfonic acid functional groups attached to a styrene divinylbenzene copolymer lattice. The amount of resin cross-linking determines the bead pore size. A resin with a lower cross-linkage has a more open structure permeable to higher molecular weight substances than a highly cross-linked resin. For removal of cations and metal separations a high percentage cross-linked resin, such as AG50WX8 (8% resin), was suggested.

The extractant system in Eichrom's Sr Resin is 1.0M 4,4'(5')-di-t-butylcyclohexano 18-crown-6 (crown ether) in 1-octanol. A 40% (w/w) loading of this organic

solution is loaded onto an inert chromatographic support. The bed density of Sr Resin is approximately 0.35 g/mL and it's typically used to separate Sr from alkali, alkaline earth and other metal cations.

First of all, 1 g of (AG50WX8) resin was packed into a plastic cartridge. The column was pre-washed and conditioned using 10 ml of 4M HNO₃, 5 ml of H₂O MilliQ and 10 ml of 1.7M HCl. Then 25 ml of acidified (pH 2 HCl) sample were loaded. After that 15 ml of 2.5M HCl were eluted to wash away Ca, Mg and the other matrix constituents.

At this point the AG50WX8 cartridge and the Sr cartridge were connected in series and 10 ml of 4M HNO₃ were eluted through, to desorb Ra from AG50WX8 and separate it from Sr and Ba in the Sr-resin. Then 10 ml of 3M HNO₃ were eluted in order to completely recover Ra.

The series connection allows to avoid the intermediate evaporation step in Lariviere procedure, with a significant reduction of procedure duration [57]. Loading sample in Sr-resin at 4M HNO₃ didn't affect the column capacity factor k' , as in [56]. In radium 226 measurements via ICP-MS, the formation of ⁸⁸Sr¹³⁸Ba polyatomic interference is a great issue, but this could be eliminated by using Sr-resin, adsorbing Sr, partially Ba and not Ra. Referring to the graphs 3.2 below, it was chosen to work at 4M nitric acid concentration to maximize Ba and Sr uptake by Sr-resin.

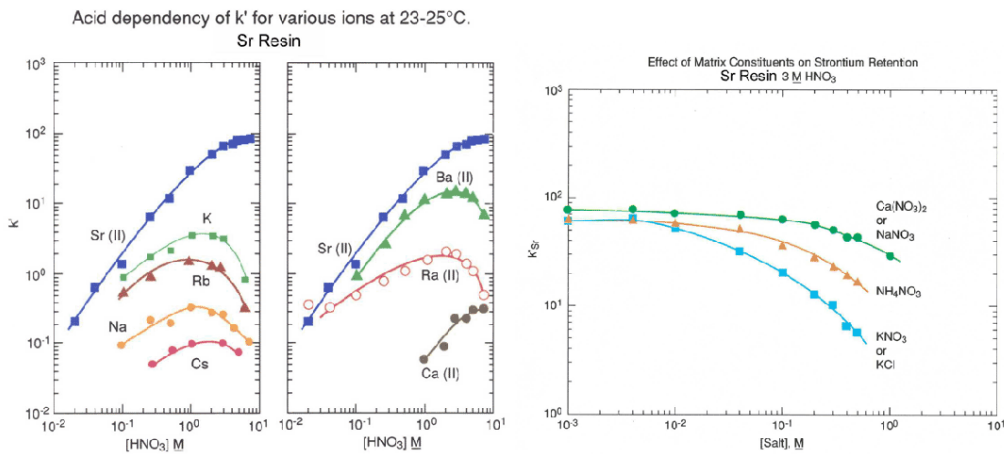


Figure 3.2: Uptaking and saturation profile of Sr-resin [56]

At the end, the solution containing Ra was collected, evaporated and redissolved in 0.5 mL of 3M HNO₃.

3.2.6 Results

Starting from the a priori assumption that ^{238}U decay chain is in secular equilibrium in our water samples and having a ^{238}U concentration between 1 and 2 ngg^{-1} , a ^{226}Ra concentration around 0.3 - 0.7 fgg^{-1} was expected. At such a low concentration, radium was barely detectable by the available instrumentation, so pre-concentration was needed. A pre-concentration factor of 50 was chosen because, on one side, it guarantees a measurable signal and good count statistics, on the other a small amount (25) mL of water sample is sufficient for the analysis.

The ^{226}Ra ICP-MS measurements suffer of both spectral and non-spectral interferences, therefore it is crucial to understand how these elements are separated in the procedure, how high are their levels in the final solution, and which are their effects on the measurement. This part of the work was focused on understanding and quantifying these effects.

Polyatomic interference study

Table 3.4: In first and second column blank and Gran Sasso (GS) ground water signal values are shown. The third and fourth column report signal values after Sr elution and total pre-concentration procedure respectively. The fifth column reports signal values of a Ce, La, Nd and Sr standard (50 pgg^{-1} Ce La Nd and 10 ngg^{-1} Sr) for interference evaluation.

Isotope	BLK (s^{-1})	GS sample (s^{-1})	Sr resin (s^{-1})	EVAPC (s^{-1})	Std (s^{-1})
Ba138	$149 * 10^3$	$97 * 10^6$	$3 * 10^6$	$120 * 10^6$	-
Sr88	$44 * 10^3$	$51 * 10^6$	$492 * 10^3$	$19.7 * 10^6$	$63.9 * 10^6$
La139	175	$1.8 * 10^3$	-	$90.5 * 10^3$	$961.5 * 10^3$
Ce140	475	831	-	$41.5 * 10^3$	$907 * 10^3$
Nd146	308	$1.4 * 10^3$	-	$68 * 10^3$	$199 * 10^3$
Ra226	0.6	-	-	-	0.6

As reported in literature, ^{226}Ra measurements by ICP-MS may suffer several polyatomic interferences [59]:

- $^{88}\text{Sr}^{138}\text{Ba}$
- $^{40}\text{Ar}^{40}\text{Ar}^{146}\text{Nd}$

- $^{87}\text{Sr}^{139}\text{La}$
- $^{86}\text{Sr}^{140}\text{Ce}$

The aim of this part of the study was to characterize the matrix concentrations of the elements Ba, Sr, Ce, La, and Nd, which are responsible for interferences, in Gran Sasso (GS) groundwater samples and to evaluate if, after a pre-concentration, these interferences could really be observed, and what was their impact on the Ra peak.

First of all, each interfering element signal in the GS groundwater and in solution after the elution procedure was measured, then signal values after evaporation were calculated and reported in Tab. 3.4 (columns 4 and 5). Considering the values in the fourth column of this table as representative of the signals of interfering elements after evaporation and redissolution, we mimicked these concentrations using single element standard solutions, and evaluated the effect in the ^{226}Ra peak window.

In order to evaluate $^{88}\text{Sr}^{138}\text{Ba}$, an interference calibration curve using Ba 500 ngg^{-1} and increasing level of Sr (0, 10, 20, 30, 40, 50 ngg^{-1}) was obtained and measured. Concentration values were selected comparing the expected signals to Sr and Ba calibration curves. When the concentrations of Ba and Sr were under 500 ngg^{-1} and 20 ngg^{-1} respectively, the counts in Ra window could be considered as a fluctuation of the background, while above these values they were signs of interference. Results are reported in figure 3.3.

The possible interferences depending on Ce, La and Nd were evaluated measuring a solution containing 50 pgg^{-1} Ce La Nd and 10 ngg^{-1} Sr. As shown in table 3.4 (column 6), no sign of interference was observed. These concentrations were around ten times higher than the actual values in the final step of the procedure, thus these interferences were excluded permanently, even considering possible fluctuations in the initial sample concentrations.

Matrix interferences

As we will see in this paragraph, the presence of Ca and Mg in ground water can affect the sensitivity of the ICP system both in a positive and a negative way. Assuming to work with a pre-concentration factor of fifty, the matrix element concentration values reported in table 3.5 were expected.

Starting from these values (column 3 (x)), and maintaining the ratio between element concentrations, we constructed a matrix calibration curve on four levels ($8x/3$, x , $x/2$, $x/6$), with a fixed value of Ra (33 fgg^{-1}). There was a non-linear decrease in elements signal, likely due to a loss of ionizing

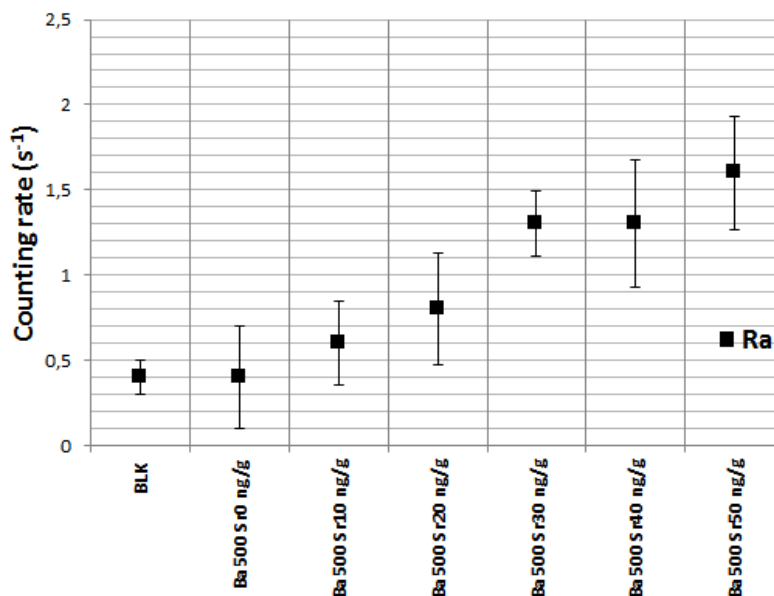


Figure 3.3: Counting rate in the Ra peak in solutions. The fixed concentration of Ba is given at 500 ngg^{-1} . The Sr concentrations varied from 0 to 50 ngg^{-1} .

efficiency, together with a quick and progressive obstruction of the skimmer cone, as shown in figure 3.4.

These effects preclude a priori the application of chromatographic extraction methods without the separation of matrix elements, as for example in the Lariviere et al. (2003) method, or in the mere application of a Sr-resin in order to eliminate polyatomic interferences [57].

After the application of the elution procedure, matrix elements were separated with an efficiency higher than 99%. Then the sample was concentrated by a factor of 40, obtained evaporating to dryness the 20 ml of elution products and redissolving them in 0.5 ml of 3M HNO_3 . Signal values and relevant efficiencies are reported in table 3.5.

The matrix effect was then evaluated for concentrations around those previously obtained, using five matrix matched Ra226 standards with increasing concentrations of Ca and Mg (Ca 1, 2, 5, 10, 20 μgg^{-1} and Mg 0.25, 0.5, 1.25, 2.5, 5 μgg^{-1}) and comparing them with a standard without Ca and Mg at the same Ra226 concentration (27.5 fgg^{-1}). Results are reported in table 3.5.

This study was carried out for evaluating if possible slight variations in

Table 3.5: The first part reports: Ca, Mg, K and Na concentration typical values in a sample of Gran Sasso groundwater (col. 1), theoretical values after pre-concentration without separation (col. 2), Ca and Mg signals in GS ground water (col. 3), after elution procedure (col. 4), after evaporation (col. 6) and the relevant separation efficiencies (col. 5). The latter part shows Ra signals with respect to increasing values of Ca and Mg. Each sample was spiked at ^{226}Ra concentration of 27.5 fgg^{-1} .

Isotope	GS (μgg^{-1})	GS APCWS(x) (μgg^{-1})	GS (s^{-1})	After proc. (s^{-1})	Sep. eff. %	After Evap. (s^{-1})
Ca	18	1000	$46 * 10^6$	$0.26 * 10^6$	99.4	$10.4 * 10^6$
Mg	9.4	500	$860 * 10^6$	$1.63 * 10^6$	99.8	$65.2 * 10^6$
Na	0.9	50				
K	0.2	10				

Isotope	S1	S2	S3	S4	S5	Std
Ca (μgg^{-1})	1	2	5	10	20	0
Mg (μgg^{-1})	0.25	0.5	1.25	2.5	5	0
Ra (s^{-1})	93(2)	93(1)	96(3)	97(1)	95(1)	85(2)

Ca and Mg concentrations, due to either different initial values in samples or differences in the separation efficiencies of the procedure, or both, could affect the sensitivity of Radium signal.

Results showed that the presence of the matrix has a positive effect on the signal, this remaining quite constant over concentration range. This can be taken into account in measurement sessions performing a calibration curve acquisition with standards matching at the proposed Ca and Mg concentrations.

Separation procedure optimization and recovery studies

The utilization of a strong cation exchange resin (AG50WX8) in separating Ra from water matrix constituents was well documented in literature [49, 51, 53, 52]. The procedure can be divided in four steps:

1. Pre-washing and conditioning
2. Sample loading
3. Washing away Ca, Mg and other matrix constituents using HCl
4. Recovering of Ra using HNO_3

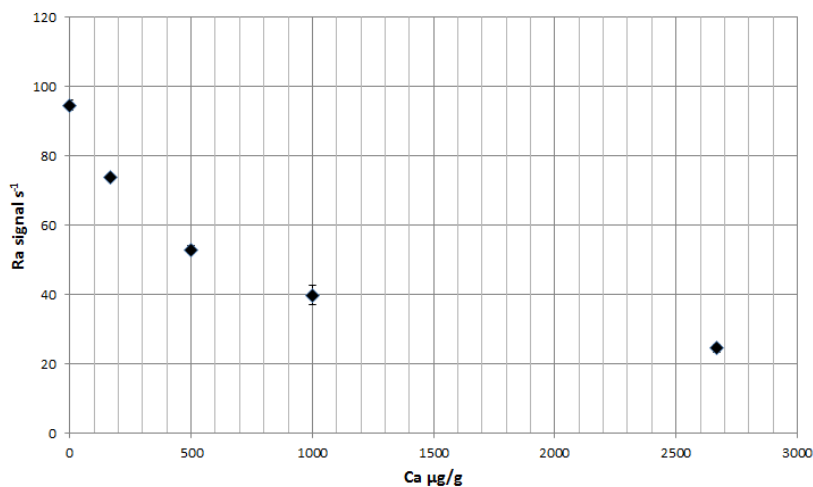


Figure 3.4: Effect of Ca concentration on Ra signal.

The four different methods cited above mainly differ in HCl molarity in step 3, and the matrix element separation efficiencies are not always reported. In order to evaluate the separation efficiencies and the radium recovery for each method, four replicas with different HCl molarity in phase 3 were done, using a GS sample spiked at 22 fgg^{-1} of ^{226}Ra . The results are reported in Table 3.6.

Table 3.6: Ra recovery efficiencies and Ba, Sr, Ca and Mg separation efficiencies.

step3 HCl M	recovery eff %		separation eff %			
	Ra226		Ca43	Mg25	Sr88	Ba138
1.7	86.9		68	98.2	19.8	23.4
2.5	100		99.7	99.9	96.4	12.1
4	64.2		99.8	99.9	99.7	96.2
6	9.1		99.8	99.9	99.6	76.4

Considering recovery and separation efficiencies, a 2.5 M HCl wash seemed the best choice, as suggested in Lariviere et al. (2005) [51].

The elution profiles for the most important elements were reported in figures 3.5 and 3.6. They graphically show in which step of the procedure each single element was eliminated or recovered. The first one shows a very good separation efficiency for Ca and Mg and also a very good recovery

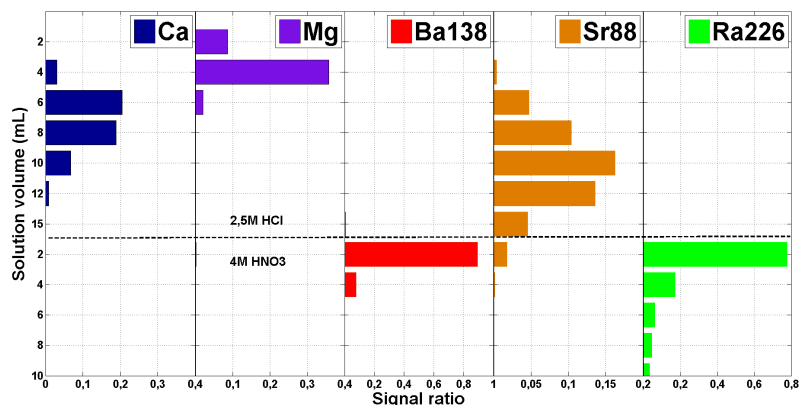


Figure 3.5: AG50WX8 elution profile for Ca, Mg, Ba, Sr, and Ra, solutions collected every 2 mL. Bars amplitudes were expressed in an arbitrary unit obtained as signals ratio between the volume fraction collected and the original sample, weighted for the relevant volumes.

efficiency for Ra, Ba and Sr were not retained properly by this resin, so using Sr-resin was required to avoid the formation of $^{88}\text{Sr}^{138}\text{Ba}$ interference.

After the washing with HCl (step 3), the two cartridges were connected in series and the rest of the procedure was performed. The series connection allows to avoid the intermediate evaporation step in Lariviere procedure [51], with a significant reduction of procedure duration. Loading sample in Sr-resin at 4M HNO_3 didn't affect the column capacity factor k' , as in [56].

After the elution in Sr-resin, as shown in figure 3.6, separation efficiencies of Ba and Sr was sensibly improved, 98% and 99.3% respectively, the resulting values of Ba and Sr were below the level of interference formation obtained in figure 3.3.

At last looking at figure 3.6, the amount of 3M nitric acid rinse was then reduced by 5 mL.

A quantitative evaluation of Ra recovery of the entire method was performed on twelve replicas, E3dx water spiked at 22 fgg^{-1} Ra226. A Ra recovery efficiency of $(100 \pm 3)\%$ was achieved.

Careful optimization of the separation and pre-concentration procedure led to an almost perfect Ra recovery and the same could be said with respect to the separation of the interfering elements. The instrumental limit of detection was 0.089 fgg^{-1} considering a 3σ criterion. The absolute detection limit was of 0.049 fg using 25 mL of liquid sample equivalent to $1.95 \cdot 10^{-18} \text{ gmL}^{-1}$ [57].

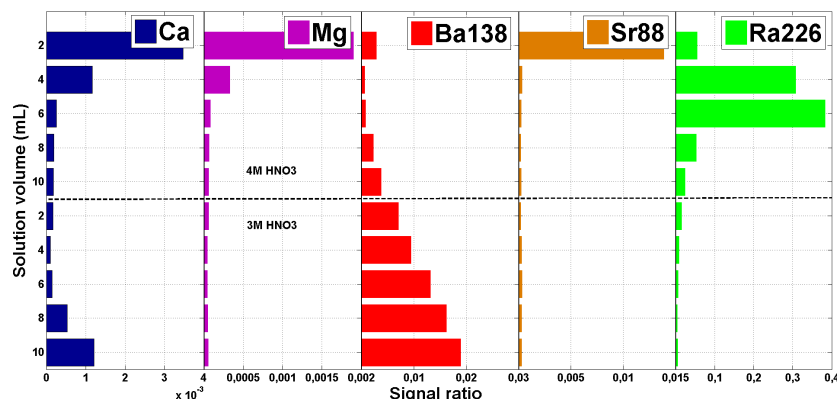


Figure 3.6: Sr-resin elution profile for Ca, Mg, Ba, Sr, and Ra, solutions collected every 2 mL. Bars amplitudes were expressed in an arbitrary unit obtained as signals ratio between the volume fraction collected and the original sample, weighted for the relevant volumes.

3.3 Uranium isotopic ratio measurements

Isotopes identification and isotope ratios precise measurements are the main objectives of mass spectrometry since its early days in 1910-1940. Nowadays this branch of application is still widely used in, for example, dating and tracing experiments [60, 61].

Isotopic analysis of metal elements are made using either a thermal ionization mass spectrometer (TIMS) or a ICP-MS. The main difference between these two instruments is how the sample is introduced into the instrument and how the sample is ionized. The first technique allows the most precise and accurate estimation, but it requires long preparation and measurement times.

In this study, measuring uranium isotope ratios by TIMS, was not a viable option, because the total element amount required for one measurements is almost $1\mu g$ that means a starting sample volume greater than 1L, the actual volume of our samples. Therefore a single collector ICP-MS instrument was chosen.

It has to be pointed out that, in order to obtain optimum isotopic analysis, a multi-collector instrument should be adopted, able to acquire different isotopes simultaneously and not sequentially as it happens with single collector ones.

Among the natural uranium isotope ratios in groundwater analysis $\frac{^{234}\text{U}}{^{238}\text{U}}$ is the most studied one due to its high variability and to its applicability to mixing problems.

This measure has several issues that need to be analyzed and discussed [62]:

- interferences formation: compounds such as ${}^xUH^+$ may interfere with the mass ${}^{x+1}U$, Pb in the matrix may form polyatomic species such as PbO_2^+ and PbN_2^+ that may overlap uranium mass range.
- dead time correction: the detector dead time can be defined as the minimum time interval between the impact of two ions on the detector allowing to identify them as two different events. Measuring solutions with the same isotope ratios but different uranium concentrations may alter the measured isotope ratios due to the total dead time variation. There are several different ways to calculate the dead time value although the use of standard isotopic solutions with different concentrations seems to be the best [63].
- analog conversion factor: it means the cross calibration factor between the counting and the analog detector modes. It comes into play when the two measured isotopes have a great isotopic abundance difference which forces the use of the two detector modes as in the case of $\frac{{}^{234}U}{{}^{238}U}$.
- abundance sensitivity: for a nuclide of M mass it is defined as the ratio between the signal at mass $M + 1$ and the signal at mass M of the same isotope.
- mass bias: it is a mass-dependent transmission in mass spectrometers due to several physical processes taking place mainly in ionization and transmission sectors of the instrument.

3.3.1 Materials

Hyperpure nitric acids (Panreac, Barcelona, Spain), deionized water (Milli-Q water system, Millipore, Bedford, MA, USA), and syringe filters $0.45\ \mu m$ (Olimpeak) were used.

Uranium isotopic standards were obtained by dilution from a $100.5\ Bqg^{-1}$ natural isotopic composition STD IRMM-3184 (Institute for Reference Material and Measurements of European Commission Joint Research Centre, Geel, Belgium).

3.3.2 Equipment

A SF-ICP-MS (Finnigan Element 2, Thermo Scientific) was used. It was equipped with a desolvating system Apex Q high-sensitivity (Element Sci-

entific Inc.). Samples were introduced by means of a $100\mu\text{Lmin}^{-1}$ micro-nebulizer. Tuning and acquisition parameters are reported in table 3.7.

Table 3.7: Optimized values of Finnigan Element 2 with Apex Q introduction system.

Instrumental parameters	
Gas flow (L/min)	
Sample	0.875
Auxiliary	0.2-0.3
Cool	16
RF power (W)	1250
Interface cones	Nickel
Apex-Q parameters	
Spray chamber temperature ($^{\circ}\text{C}$)	100
Peltier-cell condenser temperature ($^{\circ}\text{C}$)	2
N_2	on
Acquisition parameters	
Resolution	300
Number of run	30
Number of passes	1
Samples per peak	50
Mass window (%)	20
Integration window (%)	100
Analyte time	(s)
^{238}U	0.01
^{235}U	0.1
^{234}U	1
Total acquisition time (s)	264.4

The instrument was optimized with respect to the gas flow and the ion lenses parameters, in order to reach stable signal and flat peaks top. The acquisition strategy was centered on increasing sensitivity and on improving count statistics, especially for ^{234}U . A narrow (20%) mass window allows to measure, where the peaks are flat, a lower number of samples (8 in our

case). An integration window of 100% means taking into account the entire mass window being chosen. The total sample acquisition time was about 266.4s, divided among the different masses in a near inverse proportion to the isotopic abundance.

3.3.3 Results

In this study it was chosen to work without preconcentration in order not to risk that the matrix effect might alter isotope ratios in comparing standards and samples, so 10 mL water samples was filtered and acidified at 2.5% HNO₃. This choice led to an analytical challenge: measuring ²³⁴U. As a matter of fact ²³⁸U concentration in our samples is between 1 and 2 ngg⁻¹, so, considering the relative isotopic abundances ²³⁸U = 99.27%, ²³⁵U = 0.72%, and ²³⁴U = 0.005%, a ²³⁴U concentration of about (50 – 100)fgg⁻¹ is expected. In the first place, in order to improve count statistics the acquisition duration time on ²³⁴U was extended as in the ²²⁶Ra case.

In order to evaluate interferences formation due to PbO₂⁺ and PbN₂⁺, an interference test was performed measuring a 10 ngg⁻¹ Pb aqueous solution acidified at 2.5% HNO₃. The signal found for the masses of interest was comparable with the instrumental background, therefore, being the concentration of lead in our samples less than 1 ngg⁻¹, interference of this type was excluded.

Regarding the formation of ^xUH⁺, a signal ratio ²³⁸UH⁺/²³⁸U of 5 * 10⁻⁵ is reported in the literature [58]. Using a desolvation system can only improve this ratio, diminishing the formation of such a molecule. Moreover, considering the relative abundances, this interference may have an impact in the case of ²³⁶U or ²³⁹Pu, but not in the cases of our interest.

A dead time correction value of 5ns was determined by measuring a series of uranium isotopic standard in a concentration range of 0.5-10 ngg⁻¹.

An overall correction of the analog conversion, the abundance sensitivity, and the mass bias effects was performed using the standard bracketing method. This consists in interpolating the bias of the unknown sample between the biases inferred from two standard runs, one preceding and one following the sample analysis. The measured isotope ratios (*r_i*)_{sm} are corrected accordingly to

$$(R_i)_{sm} = (R_i)_{std} \frac{(r_i)_{sm}}{\sqrt{(r_i)_{std}^1 \times (r_i)_{std}^2}}$$

where (*R_i*)_{std} is the standard certified value, (*r_i*)_{std}¹ and (*r_i*)_{std}² are standard solution measured values after and before the sample, and (*R_i*)_{sm} is the

corrected value for the isotope ratio involved. This correction can only be applied when standards and samples have just minimal differences in matrix composition [62].

In this study, the following uranium isotope ratios have been measured:

$$(R_i)_{sm} = \frac{{}^{235}\text{U}}{238\text{U}}, \frac{{}^{234}\text{U}}{238\text{U}}$$

The data analysis strategy is fundamental in achieving a reasonable uncertainty level especially in case of ${}^{234}\text{U}/{}^{238}\text{U}$. The instrument software was not developed for the isotope ratios analysis, so for each analyte it calculates the signal value and the relevant RSD(%). Starting from these values a ratio is calculated and the relevant relative uncertainty is:

$$\frac{\Delta(R_i)}{R_i} = \sqrt{\left(\frac{\Delta(x\text{U})}{x\text{U}}\right)^2 + \left(\frac{\Delta({}^{238}\text{U})}{238\text{U}}\right)^2}$$

where $x\text{U}$ and ${}^{238}\text{U}$ are signal values, and $\Delta(x\text{U})$ and $\Delta({}^{238}\text{U})$ are the corresponding statistical uncertainties. Typical relative uncertainty values are about 3% for ${}^{235}\text{U}/{}^{238}\text{U}$ and 4% for ${}^{234}\text{U}/{}^{238}\text{U}$ including a coverage factor $k = 1$.

These uncertainty levels do not allow to distinguish hypothetical differences among samples from the same point or from different points of sampling in the same aquifer.

Noting this issue, therefore a totally different data analysis approach was adopted. Raw data files were recovered. For each of the 30 passes (sequential scan of the peaks of the chosen analytes) the isotope ratios ${}^{235}\text{U}/{}^{238}\text{U}$ and ${}^{234}\text{U}/{}^{238}\text{U}$ were calculated. The signal value of each analyte was obtained by averaging the 8 acquisitions per peak. Mean and standard deviation of the isotope ratio population were calculated, an outliers rejection procedure using a 2σ criterion was performed. Mean, standard deviation, and standard deviation of the mean were recomputed.

From the methodological point of view, this is the most appropriate strategy because, on one side, even if in a sequential manner it tends to the simultaneity of a multi-collector measurement. On the other side, keeping the acquisitions separate and rejecting the outliers protects against the effects of rapid changes in signal values due to the nature of the ion source or to possible malfunctioning of the instrument.

Typical relative uncertainty values, adopting this procedure, are about 0.3% for ${}^{235}\text{U}/{}^{238}\text{U}$ and 0.5% for ${}^{234}\text{U}/{}^{238}\text{U}$ including a coverage factor $k = 1$.

Chapter 4

Results and discussion

4.1 Gran Sasso aquifer

The Gran Sasso and the Velino-Sirente mountains (central Italy) form a hydrogeological system which extends over an area of about 2000 km^2 (figure 4.1). This complex system can absorb 714 mm of annual effective infiltration and it has a mean discharge of $49 \text{ m}^3/\text{s}$ [64]. The system consists of a double chain separated by deep trenches and high plains and with deep depressions at the boundaries. The northern part, the Gran Sasso chain, is formed mainly by carbonatic units which thrust northwardly over clay-marly sandstones. The southern slope consists of a series of ridges stretching out along a NW–SE direction, and sloping down southwards. These ridges extend under alluvial deposits of the Aterno River Valley [65].

Inside the Gran Sasso massif a regional deep aquifer is located, consisting of a series of minor aquifers separated by the main structural discontinuities with permeability values from 10^{-11} up to 10^{-4} m/s . These differences in permeability values identify aquifer areas with different hydrogeological features ranging from porous, to fractured, to karst. A detailed study of this structure was performed by drilling three boreholes before the tunnel construction and establishing the INFN underground laboratory (1970–1985) [68] (figure 4.2). After the construction of the tunnels, the aquifer reached a new hydrodynamic equilibrium.

Gran Sasso National Laboratory (LNGS-INFN) underground facilities are located on a side of the ten kilometers long freeway tunnel crossing the Gran Sasso Mountain, precisely below the Mount Aquila. The Laboratory hosts experiments in the fields of astroparticle physics and nuclear astrophysics needing low background environment. Figure 4.3 shows the structure of the underground laboratory.

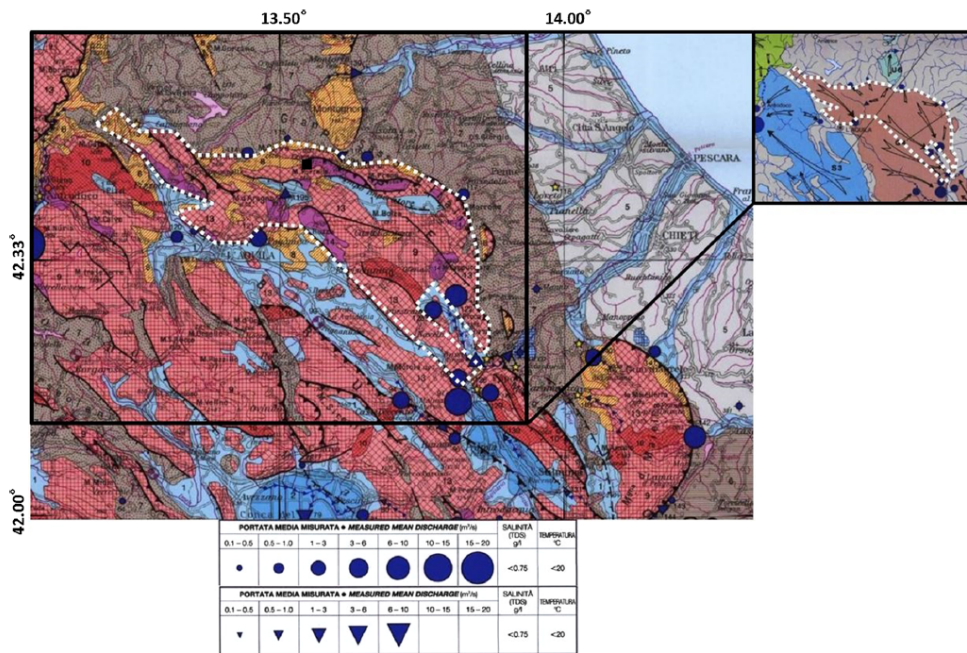


Figure 4.1: Hydrogeological scheme of central Italy, modified from Boni et al. (1986)[66]. The white dotted line represents the Gran Sasso aquifer, symbolized by a 25 vertices polygon. The black dot represents LNGS-INFN. Groundwater flow lines are shown by arrow symbols in the small picture. Hydro-geological complex: light blue (1) is used for shallow alluvial aquifer, dark blue (2) for thick multi-strata alluvial aquifer. A pattern of red squares shows the carbonate infiltration areas (9, 10, 11, 12, 13), where effective infiltration prevails over both surface runoff and evotranspiration. The mesh is closer where infiltration is higher. Yellow areas refer to volcanic complex (4) and marly-calcarentic complex (8), where the effective infiltration preferably occurs in the most fractured hard rocks. Violet refers to dolomitic complex (14). Effective infiltration seems to be comparable to that of volcanic complex (4). No data is available regarding surface runoff and evotranspiration. Light gray (5) is used for areas where both surface runoff and evotranspiration prevail over infiltration. Percolation and aquifer capacity are consequently negligible. Dark gray (7) shows the occurrence of limited effective infiltration and diffuse percolation. Hydrological symbols: blue filled circles identify springs, considered as a localized natural discharge of ground water emerging in a restricted area. The mean discharge is proportional to the diameter. Blue filled triangles identify linear springs, considered as a natural discharge of ground water emerging into a portion of a stream, which varies in length from a few hundred meters to some kilometers. The mean discharge is proportional to the size [67].

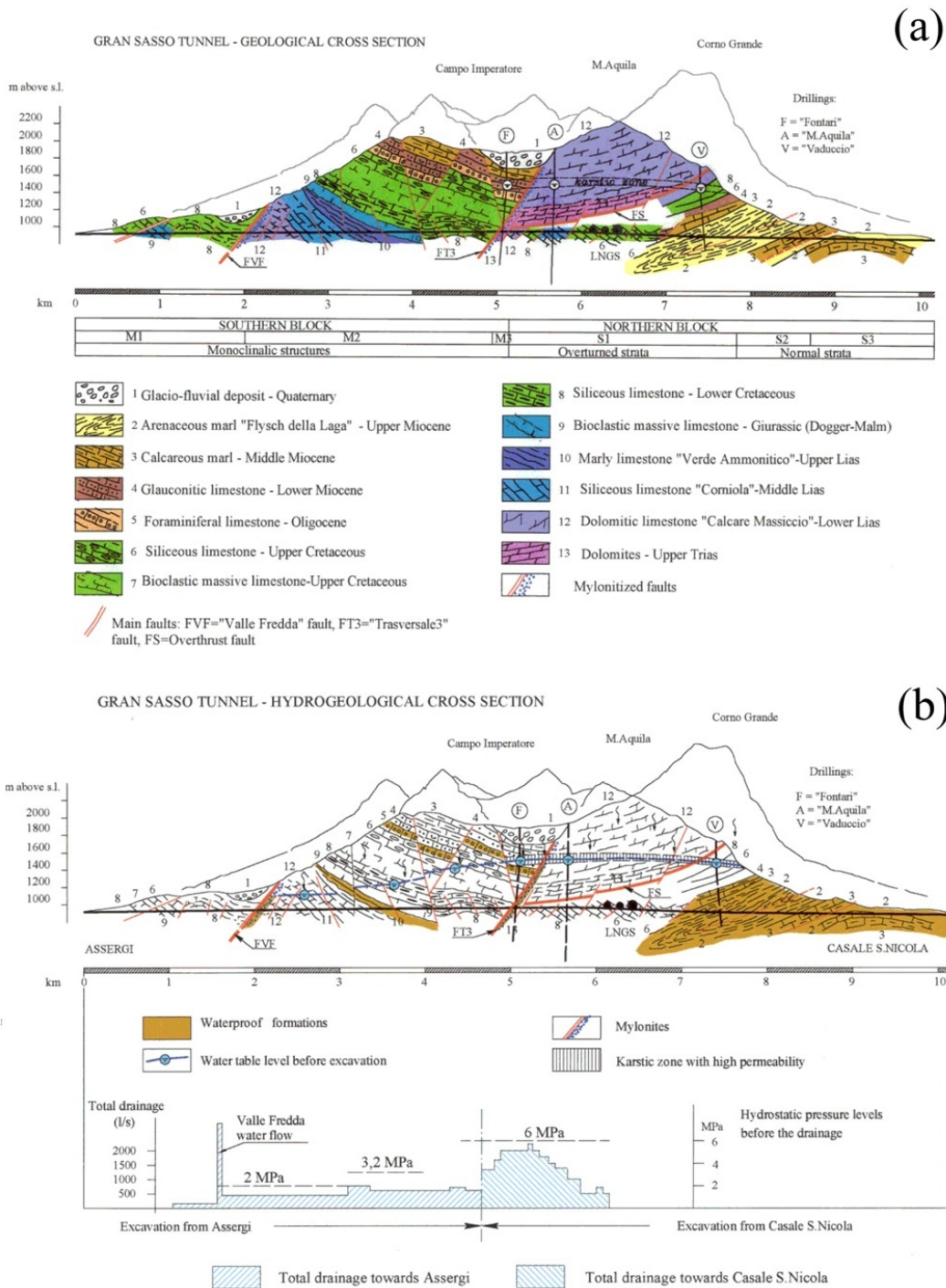


Figure 4.2: The Gran Sasso massif: (a) geological cross-section, (b) hydrogeological cross section. LNGS-INFN are denoted by three black dots.[2]

4.2 Experimental setup

The Gran Sasso National Laboratory is located inside the largest aquifer in central Italy, within the limestone formation of the upturned syncline, near the main overthrust fault. This complex hydrogeological system is characterized by separation of water masses belonging to two different flowpaths: the former, where the main underground laboratories are located, flows in well drained cretaceous formation, while the latter flows within not drained and poorly permeable dolomitic formations. Depending on the path and on the percolation features, water masses are therefore characterized by different chemical-physical properties. LNGS-INFN is located in the saturated zone in the core of the aquifer, below the water table oscillation zone.

Within the framework of the LNGS-INFN scientific program ERMES (Environmental Radioactivity Monitoring for Earth Sciences) radioactivity together with chemical, physical and fluid dynamical characteristics of groundwater inside the underground laboratory are monitored.

The groundwater monitoring started in June 2008 with the aim of better defining the groundwater transport processes through the cataclastic rocks as well as to check the groundwater contribution to the neutron background at the LNGS-INFN. In fact, neutrons from cosmic radiation are properly shielded by dolomite and flint rocks (1400 meters of overlying rocks, equivalent to 3100 of water (mwe)), while the contribution of the spontaneous fission of rocks and water inside the underground facilities is under investigation.

Groundwater to be analyzed flows in pipes inserted into the rock wall for 3 to 6 meters. Samples have been collected weekly in sites E1, E3, and E4, located inside the underground laboratories; the relevant positions are shown in figure 4.3. More precisely samples collection sites are located on both sides of the overthrust fault (shown in figure 4.3 as a red line) which crosses the underground laboratories separating limestones from dolomite rocks [64]. In site E3, where rocks in the measurement site mainly consist of dolomites, two different sampling points are investigated: E3 which is parallel to the main overthrust fault, northward and E3dx which is orthogonal to the fault, towards E4.

After 5 minutes of water flushing at maximum flow, samples are collected and stored in 1L cleaned polyethylene bottles. On each water sample the concentrations of uranium (U), sodium (Na), magnesium (Mg), potassium (K) and calcium (Ca) are measured via ICP-MS; the values of electrical conductivity (EC), redox potential (ORP) and pH are also measured. Uranium concentrations obtained from June 2008 to October 2014, for the four sampling sites inside the LNGS (E1, E3 and E4, E3dx) are shown in figure 4.4. Results have been presented in several works [2, 3, 69, 67].

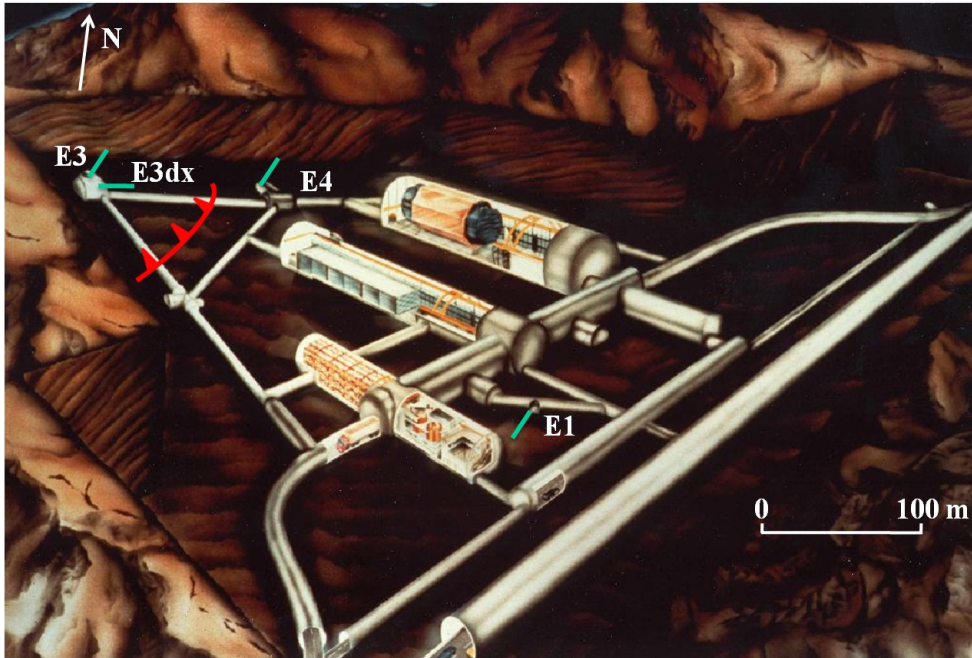


Figure 4.3: Schematic view of the LNGS-INFN. The overthrust fault (red line) and monitoring sites E1, E3 and E4 are also shown. At site E3 there are two sampling points: E3 which is parallel to the overthrust fault in the North direction; and E3dx which is orthogonal to the fault in the E4 direction into the cataclastic rocks [2].

Detected uranium contents, reported in figure 4.4 show different features. Two distinct groups of waters can be identified: one (E3 and E3dx) exhibits higher average value and large variations, while the other (E1 and E4) has shown relatively low and weakly varying content of uranium [2]. In both groups the uranium groundwater content follows a seasonal trend, with the exception of some anomalous values. In all four sites on this underlying trend, positive spike-like anomalies with short time variations of 40 – 80% can be observed in the period between June 2008 and March 2009. Such anomalies, can also be found in the period between May 2010 and September 2010, in site E3dx only.

The central part of the Apennines is characterized by extensional tectonics since the Pliocene epoch, with most of the active faults being normal in type and NW–SE trending. At a regional scale, fault systems and individual faults are organized into larger fault sets that run almost parallel to the Apennines chain axis [70]. The active normal faults of the central Apennines are commonly divided into two parallel sets, a western set and an eastern one. Some of the strongest historical earthquakes have been attributed to

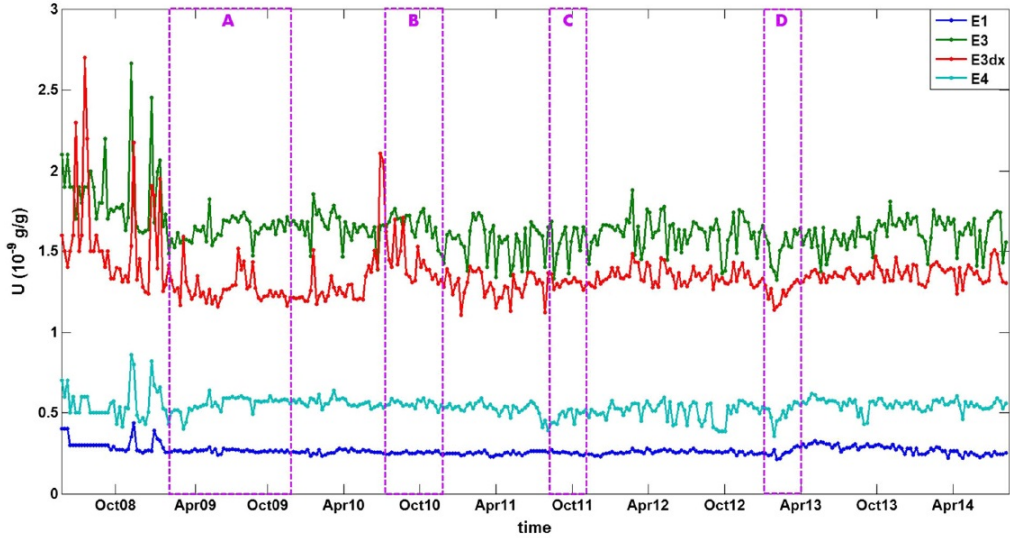


Figure 4.4: U time series for sites E1 (blue), E3 (green), E3dx (red) and E4 (cyan), together with Period A (February–December, 2009), Period B (July–December, 2010), Period C (August–November, 2011) and D (January–April, 2013) (dashed purple rectangles). Uranium groundwater anomalies are identified before the L’Aquila earthquake in all four sites, differently from the other three seismic activations. The relative accuracy for U is always less than 5% [67].

the rupture of the western set of normal faults in this area. On the contrary, the eastern set has not been activated in historical times [71].

The area under investigation has been affected by a seismic swarm from October 2008 to April 2009, before the main shock of April 6th 2009, $M_w = 6.3$, $M_L = 5.9$, occurred nearby L’Aquila, with normal faulting on an NW–SE oriented structure about 15 km long, dipping toward SW and located in the western fault set [3]. Geological investigation identified the Paganica fault as the causative fault of the seismic event [71]. The main shock was followed by a period of relatively intense seismic activity, associated with aftershocks occurrence. A further, moderate size, series occurred in the second half of 2010, NW of the main shock epicentral area, at a distance of about 30 km, from the Paganica fault. The main event in this cluster being an earthquake with $M_L = 4.0$ on August 28th 2010, accompanied by six earthquakes with magnitude $M_L \geq 3.0$, and by about 100 additional events with $M_L \geq 2.0$, which occurred within an area of 5 km radius, from July to December, 2010. Hence, the series is characterized by a quite large number of events with fairly small magnitudes [69].

Relations between uranium anomalies and seismic activity were deeply investigated [3, 67]. In order to do this, evaluating monthly number of events and normalized monthly energy release, four periods of relative intense seismic activity were identified (figures 4.4 and 4.5): Period A (February – December, 2009), i.e., the preparation phase, the main shock and the aftershocks of the L’Aquila earthquake, Periods B (July – December, 2010) with much lower normalized energy release and fewer number of events than the previous one and Periods C (August – November, 2011) and D (January – April, 2013) with a small increase of seismicity over the seismic background. For a detailed explanation of the methods used in this analysis we refer to [67].

In figure 4.5 the spacial distribution for the four clusters, relevant to both, the LNGS-INFN and the aquifer, is reported. This clearly shows the difference between a large seismic event and lighter seismic clusters. The sequence A consisted of almost 2800 recorded events with M_L ranging from 2.0 up to 5.9 (magnitude of the main shock). The maximum magnitude associated with the earthquakes in Periods B–D reaches values of $M_L = 3.4–3.6$. Moreover the cluster B is located in the northwestern area of the LNGS-INFN (in a normal fault area), while the clusters C and D are positioned north with respect to the LNGS-INFN, in a very close thrust fault region.

Uranium groundwater content spike-like anomalies were observed before Period A in all four sites and before B only in site E3dx in a regime of normal fault, while no anomalous values were individuated before Periods C and D. This might be due to the different structures involved, in fact clusters C and D were located in thrust fault area [67].

A possible physical explanation of the presence of spike-like anomalies in uranium concentration time series is given in [3]. It could probably be related to geodynamical processes occurring before earthquakes, which triggered fluids diffusion processes thorough the overthrust fault; moreover upward fluids migration is favored in the normal fault area, while it is inhibited in the thrust fault area.

4.3 Tritium time series

In order to test this hypothesis against the possibility that uranium content anomalies might be related to input by the vadose zone thorough variations of percolation processes linked with meteoric events, 3H activity concentration data were acquired and analyzed.

As discussed in the first chapter 3H concentration in groundwaters depends on the input function (tritium contents in rainfalls and snowfalls) and on the time span between infiltration and sample collection. Since there were

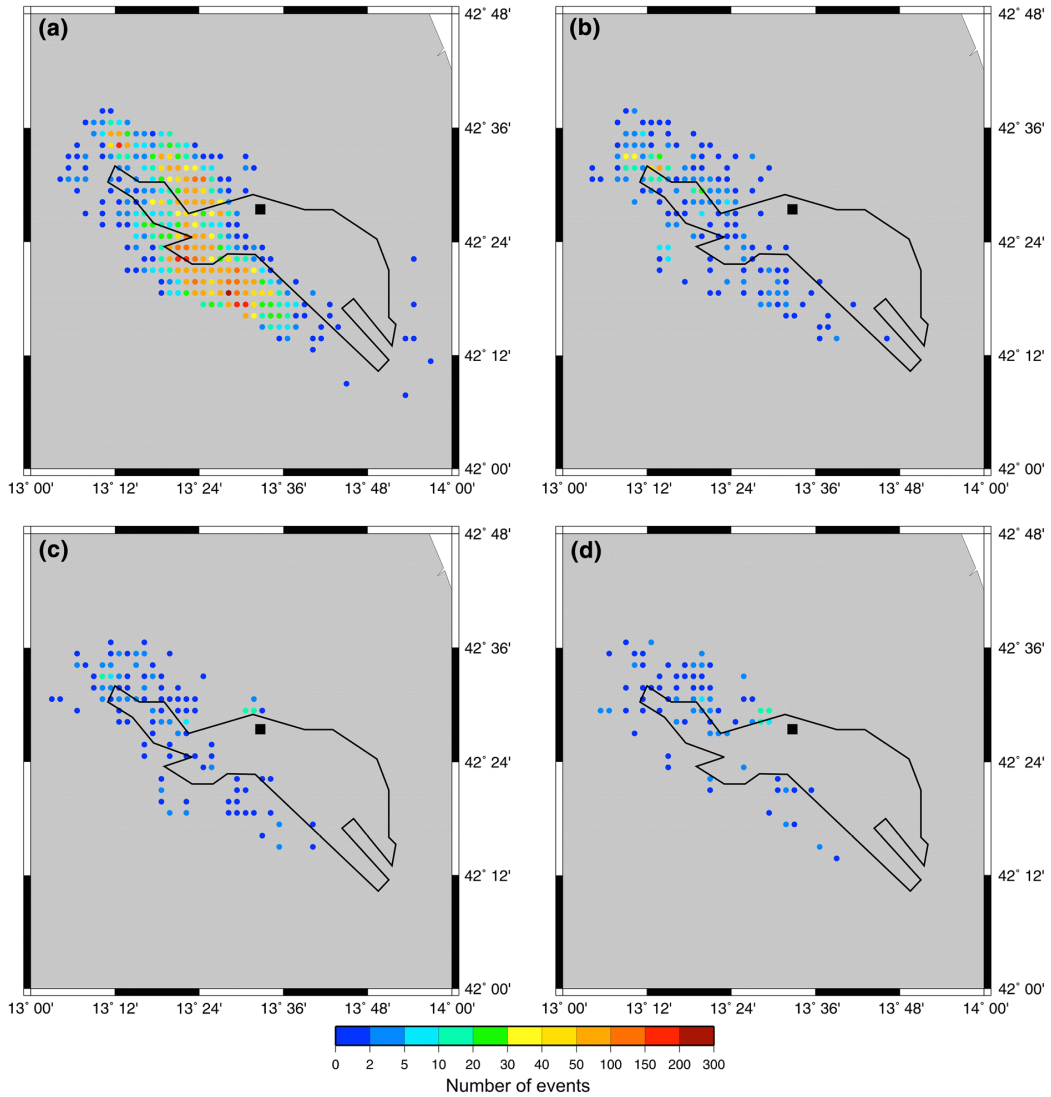


Figure 4.5: Spatial distribution of the events with $M \geq M_{min} = 1.5$. During the four identified time intervals A, B, C and D. The intensity of seismic activity, expressed as number of earthquakes over a regular grid of $0.05^\circ \times 0.05^\circ$, is represented by a color scale from blue to red. The black dot represents LNGS-INFN. The aquifer is also shown. [67]

no recordings of tritium content in precipitations for the zone of interest, percolation and residence times could not be quantified, nevertheless assuming as input function a tritium constant distribution in space, differences can still be identify among water masses due to percolation processes and residence times. Moreover studying tritium content variation over time may enable to evaluate the dynamic behavior of the aquifer sector as a response, for

example, to an external input variation or fluids mixing within the aquifer.

A first evaluation of tritium activity concentration on the four sites inside the underground laboratories were made for a single date in [72]. The results, reported in table 4.1, show that each site has a different value. Tritium activity concentration values are expressed in tritium unit (TU) defined as

$$1 \text{ TU} \equiv \frac{[{}^3\text{H}]}{[\text{H}]} = 10^{-18}$$

Where one TU corresponds to $0.11919 \pm 0.00021 \text{ Bq/kg}$.

Table 4.1: it shows tritium activity concentration for the four sampling points on the same data inside the underground lab.

Sampling points	A(TU)
E1	4.8(3)
E3	8.4(4)
E3dx	8.2(4)
E4	6.4(4)

An attempt to study the ${}^3\text{H}$ activity concentration with respect to time was first carried out at point E3dx on six dates [69, 72], showing promising results. Tritium concentration measurements have, therefore, been extended on a bimestrial basis to the E3dx and E4 sample series. The sampling points have been chosen for their position on the two sides of the overthrust fault, which separates water masses belonging to two distinct flow paths: the former (E3dx) located in a poor permeable dolomitic formation and orthogonal to the fault, the latter (E4) located in a well drained cretaceous formation.

4.3.1 Tritium Data Analysis

E3dx

Bimestrial time series of tritium concentration for the E3dx sampling point is reported in figure 4.6. It covers a five years time span from July 2008 to July 2013, equivalent to 31 values.

Concentration values vary from $(5.9 - 9.2)\text{TU}$ with a mean of 7.5TU and a standard deviation of 0.7TU . The time plot in figure 4.6 shows strong

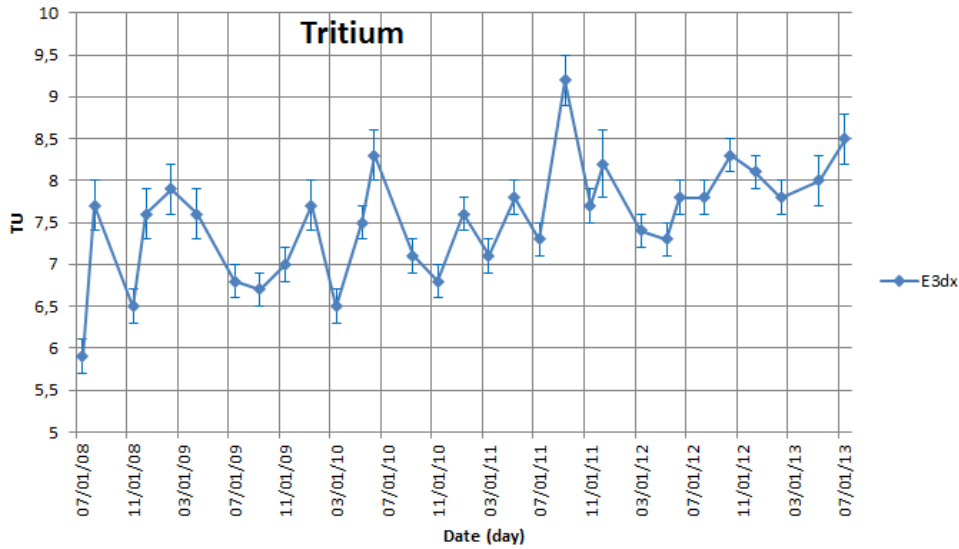


Figure 4.6: bimestrial series of 3H concentration for site E3dx.

variations over time overlapping an increasing linear trend in the second part of the series.

To introduce the analysis carried out on these series it has to be pointed out that a frequency-domain analysis, based on Fast Fourier Transform algorithm (FFT), cannot be applied due to the low number of observations [73]. Therefore the analysis is limited to a time domain analysis.

In order to highlight the presence of a trend reducing seasonal and cyclic effects, smoothing techniques were applied. The 3H series were smoothed using a weighed Moving Average filter on 7 terms. A generic term is

$$T_t = \frac{\frac{1}{2}y_{t-3} + y_{t-2} + y_{t-1} + y_t + y_{t+1} + y_{t+2} + \frac{1}{2}y_{t+3}}{6}$$

$$t = 1, \dots, N$$

where N is the sample size.

Using this filter excludes from smoothing the first and the last three terms of the original series. The weighed Moving Average (MA) on seven terms, reported in figure 4.7 as a red solid line, shows an increasing trend starting in the second part of the series approximately from October 2010.

Such a trend can be interpreted as a progressive water "rejuvenation" process due to a change in percolation paths, i.e. a supply of younger wa-

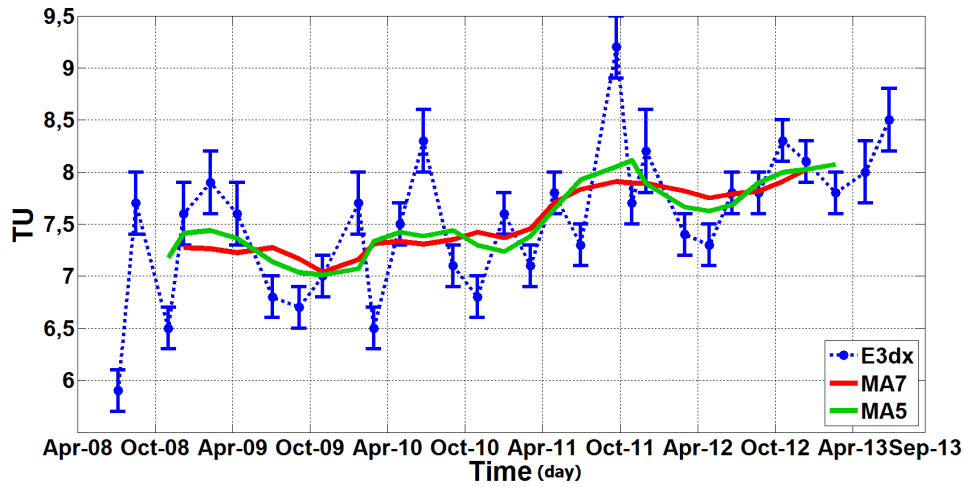


Figure 4.7: bimestrial series of 3H concentration for site E3dx, as solid lines are also plotted Moving Average on 7 terms (red) and Moving Average on 5 terms (green).

ter from the surface that slowly increases the tritium concentration in the reservoir.

In order to appreciate slow seasonal oscillation, a weighed MA filter on five terms was implemented and used to smooth the original series. A generic term is represented by

$$T_t = \frac{\frac{1}{2}y_{t-2} + y_{t-1} + y_t + y_{t+1} + \frac{1}{2}y_{t+2}}{4}$$

$$t = 1, \dots, N$$

Using a MA on 5 terms causes the loss of the first and of the last two terms of the original series. The results are plotted in figure 4.7 as a green solid line in which three and a half distinct oscillations can be observed, that may be related with the aquifer water level fluctuations.

In order to compare tritium and uranium content variation over time with respect to seismic activity, figure 4.8 was created. Yellow dashed rectangles reported periods of relative intense seismic activity for the zone of interest.

Uranium shows its typical behavior, described in the second paragraph of the present chapter, with anomalous values preceding periods A and B. Tritium content does not show any anomalous values in correspondence of ${}^{238}U$ spikes, that would justify assuming that there was an input from the vadose zone. Moreover the highest value (09/26/2011) in the original series and the

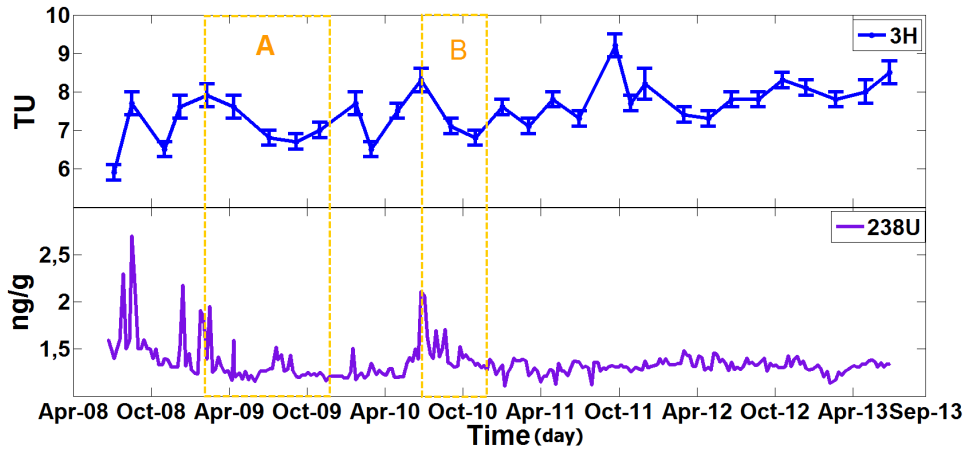


Figure 4.8: Site E3dx: the upper plot reports bimestrial series of 3H concentration. The lower plot shows weekly series of ^{238}U concentration, relative uncertainties on these values being always below 5%. Dashed yellow rectangles indicate periods of relative intense seismic activity (Period A February–December 2009 and Period B July–December 2010).

most pronounced oscillation (March 2011 - March 2012) in the MA5 were far from periods of intense seismic activity and far from uranium anomalous values.

Looking at figure 4.8, the increasing linear trend observed in the original data series and, more clearly, in the smoothed curves, might be explained as an effect of the seismic activity that induced an alteration of the percolation paths.

In order to identify a possible relation between the ^{238}U and 3H concentration time series, the correlation coefficient was estimated from the sample data, That is defined as follows, considering that the random variables x and y are sampled to obtain N pairs of observed values:

$$Corr(x, y) = \frac{\sum_{i=1}^N (x_i - \bar{x})(y_i - \bar{y})}{\sqrt{\sum_{i=1}^N (x_i - \bar{x})^2 \sum_{i=1}^N (y_i - \bar{y})^2}}$$

where \bar{x} and \bar{y} are the sample means of the variables x and y .

The estimation of the correlation coefficient, on the original data series of ^{238}U and 3H concentrations, gives $Corr(^3H, ^{238}U) = 0.12$. The estimation was repeated after the de-trending of the original series and the results is $Corr(res^3H, res^{238}U) = 0.41$. It can, therefore, be concluded that in both

cases the ^{238}U and ^3H concentration time series were not linearly related.

A particular behavior of tritium content can be observed during periods A and B where its oscillations were damped and delayed. This can likely be due to an aquifer response to the seismic activity in the zone. In particular it can be seen as a settling of the fluids squeezed out immediately after the main shock of the L'Aquila sequence [2].

E4

Bimestrial time series of tritium concentration for the E4 sampling point is reported in figure 4.9. As the previous one, it covers a five years time span from July 2008 to July 2013, equivalent to 31 values.

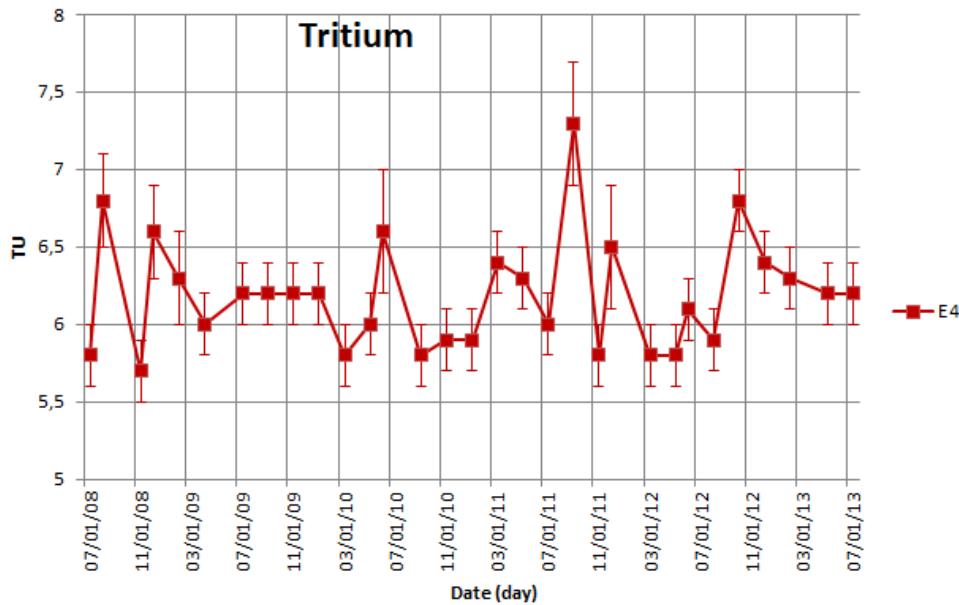


Figure 4.9: bimestrial series of ^3H concentration for site E4.

Concentration values vary from (5.7–7.3)TU with a mean of 6.2TU and a standard deviation of 0.4TU. The time plot shows significant variations over time with respect to single measurement uncertainty, that can range from 0.2 to 0.4 TU, equivalent to a relative uncertainty ranging from 3 to 6%. No long-term trend presence was observed.

According to the procedure applied in the previous paragraph, a weighed MA filter on 7 terms was used to smooth the original series. In figure 4.10 it is reported as a red solid line that shows a light decreasing trend in the first part of the series followed by one complete oscillation and a truncated one in the second part.

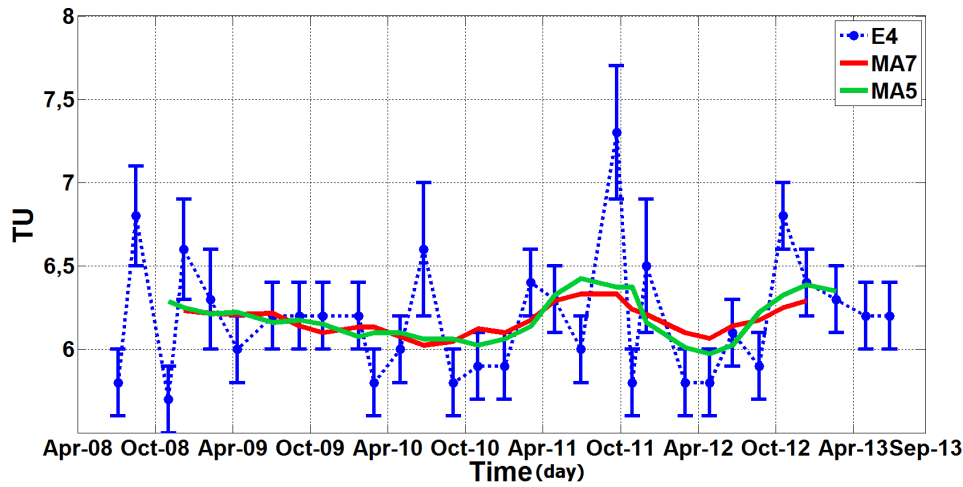


Figure 4.10: bimestrial series of 3H concentration for site E4. As solid lines Moving Average on 7 terms (red) and Moving Average on 5 terms (green) are also plotted.

As in the case of the E3dx tritium concentration time series, a weighed MA filter on five terms was also used. It is plotted in figure 4.10 as a green solid line. Unlike the previous case MA5 curve does not highlight oscillations during the first part of the series, while the oscillations in the second part of the series, already identifiable by means of the MA7 curve, where amplified by the use of this filter.

In figure 4.11 tritium and uranium concentration time series were reported with respect to periods of relative intense seismic activity, individuated by means of yellow dashed rectangles.

Uranium anomalous values can be identified before period A (February–December 2009), during the preparatory phase before L’Aquila swarm. As in the E3dx tritium content series, there are no anomalous values in the E4 series in correspondence of ^{238}U spikes, so also in this case input from the vadose zone can not be taken into account as possible source of uranium anomalies. This statement is further supported by the fact that the highest value (09/26/2011) in the original series and the most pronounced oscillation (March 2011 - March 2012) in the MA5 are found far from periods of intense seismic activity and also far from when uranium anomalous values occur.

The correlation coefficient between ^{238}U and 3H was estimated from the sample data. On the original concentration data series of ^{238}U and 3H it gives $Corr(^3H, ^{238}U) = 0.19$, while after the de-trending procedure the result is $Corr(res^3H, res^{238}U) = 0.23$. In this case too, it can be assumed that in both original and de-trended series the ^{238}U and 3H concentrations were not

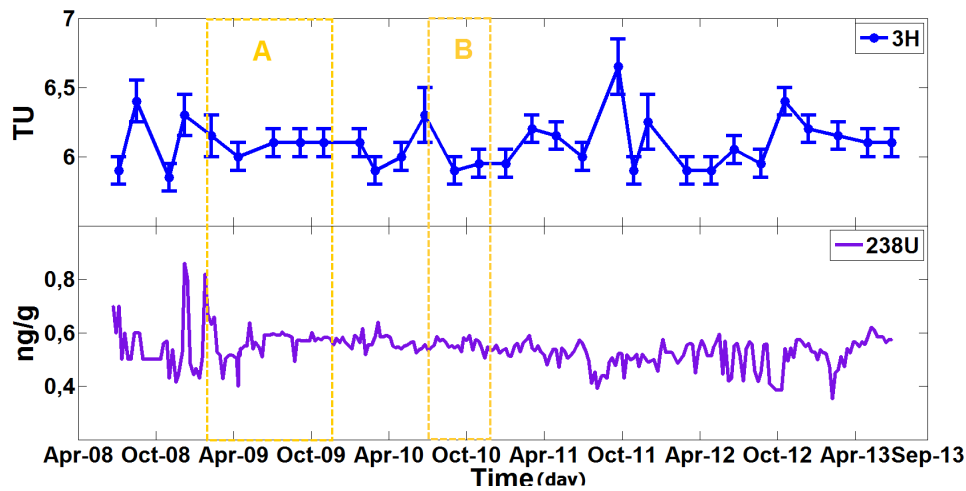


Figure 4.11: Site E4: the upper plot reports bimestrial series of 3H concentration. The lower plot shows weekly series of ^{238}U concentration, relative uncertainties on these values being always below 5%. Dashed yellow rectangles indicate periods of relative intense seismic activity (Period A February–December 2009 and Period B July–December 2010).

linearly related.

In figures 4.10 and 4.11, from the beginning of Period A (February 2009) to the end of Period B (December 2010) the tritium content shows a linear slightly decreasing trend without oscillations that could be associated to water table movements, those oscillation were found instead in the second part of the series. This scenario, where downward percolation water movements were almost completely inhibited, can be interpreted as a peculiar response of this aquifer sector to seismic activity, in particular as a return to previous condition after the fluids squeeze-out caused by L'Aquila earthquake (6th April 2009).

Comparison

Tritium measurements on each sampling site provide useful information on the behavior of the relevant aquifer region. A comparison between the two points may help to describe the dynamics connected to the two adjoining aquifer sectors separated by a natural discontinuity such as an overthrust fault.

First of all the E3dx and E4 sampling points show different mean values (7.5|6.2)TU and standard deviations(0.7|0.4)TU, confirming the presence of two distinct reservoirs with different supply systems and peculiar behaviors.

Looking at figure 4.12 it is important to notice that the increasing long-term trend is present in E3dx, while it does not show in E4.

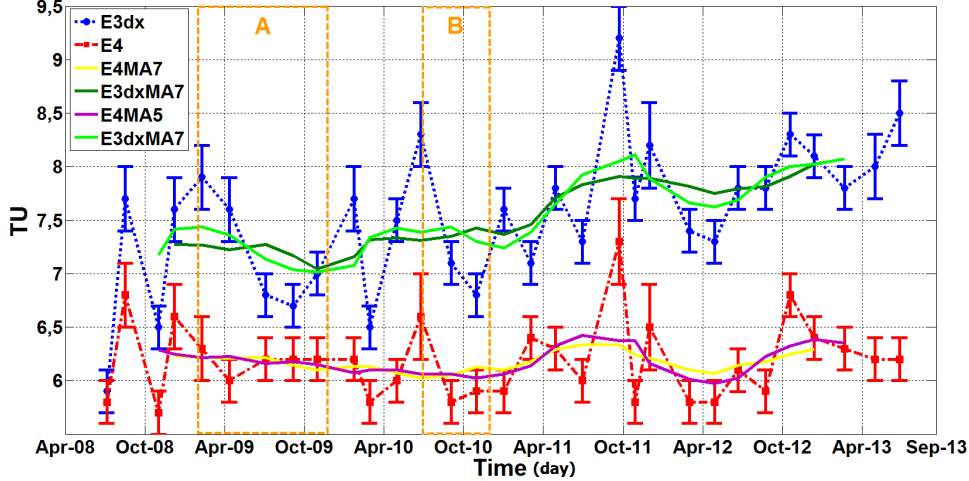


Figure 4.12: bimestrial series of 3H concentration for sites E3dx and E4 are plotted together with the relevant Moving Average on 7 and 5 terms curves. Dashed orange rectangles indicate periods of relative intense seismic activity (Period A February–December 2009 and Period B July–December 2010).

This simple observation, along with the following argument plays a key role in defining the whole system dynamics and the hydrological role of the overthrust fault, the two sampling points being on the two sides of the overthrust fault (figure 4.3) and located inside the saturated part of the aquifer below the water table oscillation level. Now considering the Darcy’s law, that is a phenomenologically derived constitutive equation that describes the flow of a fluid through a porous medium:

$$\vec{v} = -\frac{k}{\phi\mu}\vec{\nabla}p \quad (4.1)$$

where \vec{v} is the fluid velocity, k and ϕ are the permeability and porosity of the medium, μ the fluid viscosity and p the pressure. Using this equation and also considering the environmental condition $p_{E3dx} > p_{E4}$, it can be said that horizontal water movement through the fault would only be allowed in the E3dx towards the E4 direction. If this groundwater movement had actually taken place, a long-term increasing trend, similar to the E3dx one, should be noticed in the E4 tritium content time series too, which does not happen.

This simple consideration allows to support the following statements:

- the overthrust fault hydrological role is that of a impermeable septum, blocking water movements between the two aquifer sectors in the study area
- there is no evidence of water mixing between this two reservoirs during the time span taken into account
- uranium anomalies in E4, therefore, were not caused by a diffusion process through the fault from E3dx, where concentration values and spike like anomalies relative variations were higher.

Examining the MA5 curves in figure 4.12, a different behavior between the two sites can be observed in the first part of the entire time span considered, i.e. from July 2008 to about February 2011. E3dx presents two weak oscillations, while E4 shows a linear slightly-decreasing trend. In the second part a clear oscillation can be seen in both sites, suggesting a common dynamics.

In order to test this observation the entire time length was divided in two periods, called Period 1 (July 2008 - February 2011) and Period 2 (March 2011 - July 2013), the former characterized by the presence of the two seismic swarms A and B. Working on the de-trended series, the correlation coefficients were estimated and the results are reported in table 4.2 below.

Table 4.2: De-trended series correlation coefficients for E3dx and E4 sampling points on three different time spans: total, Period 1 (July 2008 - February 2011) and Period 2 (March 2011 - July 2013).

	Total	Period 1	Period 2
E3dx Corr($^3H, ^{238}U$)	0.41	0.54	-0.21
E4 Corr($^3H, ^{238}U$)	0.23	0.39	0.01
3H Corr(E3dx,E4)	0.76	0.68	0.89

Correlation values between the 3H series show agreement with the previous observation: in fact in Period 2 a linear correlation between the variables (about 0,9) occurs, while in Period 1 they are poorly correlated.

The different behavior in Period 1 might reflect a peculiar response of the aquifer sectors to seismic activity. In particular this difference in returning to pre-existing conditions after fluids squeeze-out due to L'Aquila earthquake (6th April 2009) could be related to the different rocks features in the sampling sites, E3dx located in a poor permeable porous dolomitic formation and E4 located in a well drained calcareous formation.

Considering both sites, the 3H data during Period 1 showed, despite their differences, a common state where mixing with younger water were highly inhibited (E3dx) or totally absent (E4), while in Period 2 the oscillations, related to water table movement due to a provision of percolation water, can clearly be observed in both sites.

The correlation between tritium and uranium for each site was also performed on the entire series and on the two periods separately. They always resulted uncorrelated (table 4.2).

As already discussed in the previous two paragraphs, it can be said that in both cases, independently treated and considered together, these data strongly support the hypothesis of a deep origin of ^{238}U compared to the one in which uranium content anomalies are related to water input from the vadose zone.

4.4 Radium time series

A detailed study of ^{226}Ra over time can give us information about disequilibrium in the ^{238}U decay chain, making it clear whether there is a dynamic in this variable and whether it might be related to seismic activity. Moreover the study of ^{226}Ra over time might provide information about the water-rock interaction and its development compared to the seismic activity in the area. Unfortunately no information is available on the host aquifer rock isotopic composition, in particular there are no data on ^{238}U and ^{226}Ra concentrations, so the analysis is limited to the groundwater nuclides pool.

In order to do this the ^{226}Ra measurement method via ICP-MS, presented in chapter 3, was developed and optimized [57]. The application of this procedure allowed to perform the analysis of a large number of samples, consequently two bimestrial time series from July 2008 to November 2014 are reported.

In this case E3 and E4 were chosen among the sampling points due to their position on the two sides of the overthrust fault in two distinct aquifer sectors.

In particular the E3 sampling point was preferred to E3dx because parallel to the fault, taking water along the flowpath. Tritium measurements repeated on several common dates for E3dx and E3 have shown good agreement, confirming that E3 and E3dx are sampling the same reservoir.

4.4.1 Radium Data Analysis

E3

The E3 radium time series was analyzed on a bimestrial basis from July 2008 to November 2014, measuring 39 samples. It exhibits values in a range (0.16-0.22 fg/g) with mean 0.19 fg/g and standard deviation of 0.016 fg/g. Uncertainty on single value suffers from the poor count statistics due to the very low concentration, so that the relative uncertainties range between 4% and 8% with a coverage factor $k = 1$.

Uranium, on this sampling point, shows a mean value of 1.64 ng/g with a std of 0.15 ng/g and spike-like anomalies with relative positive variations of 30-60% localized before Period A.

In order to check for disequilibrium in the decay chain over time, ^{226}Ra concentration was converted into U_{eq} concentration using $U_{eq} = \frac{\lambda_{226}}{\lambda_{238}} \text{Ra}$, where λ_{226} and λ_{238} are the relevant decay constants, and the ratio between U_{eq} and U concentrations was calculated. The uncertainty on the variable U_{eq}/U was estimated, as usual, by means of the uncertainty propagation law, that in this case is:

$$\frac{\Delta(U_{eq}/U)}{U_{eq}/U} = \sqrt{\left(\frac{\Delta(U_{eq})}{U_{eq}}\right)^2 + \left(\frac{\Delta(U)}{U}\right)^2}$$

and reported with a coverage factor $k = 2$. Uncertainty is generally dominated by the U_{eq} term, while the uncertainty contributions of λ_{226} and λ_{238} are negligible.

U_{eq}/U time series exhibits values in a range (0.22-0.38) with mean of 0.31 and standard deviation of 0.03. The condition of secular equilibrium inside the decay chain is $U_{eq}/U = 1$. In this case a ratio $U_{eq}/U < 1$ shows a decay chain out of equilibrium with a lower presence of ^{226}Ra than ^{238}U .

In figure 4.13 a time plot of U_{eq}/U together with smoothed MA7 and MA5 curves are reported.

U_{eq}/U shows a quite constant value along all the series with non statistically significant variations. To be noticed: two very low values before period A.

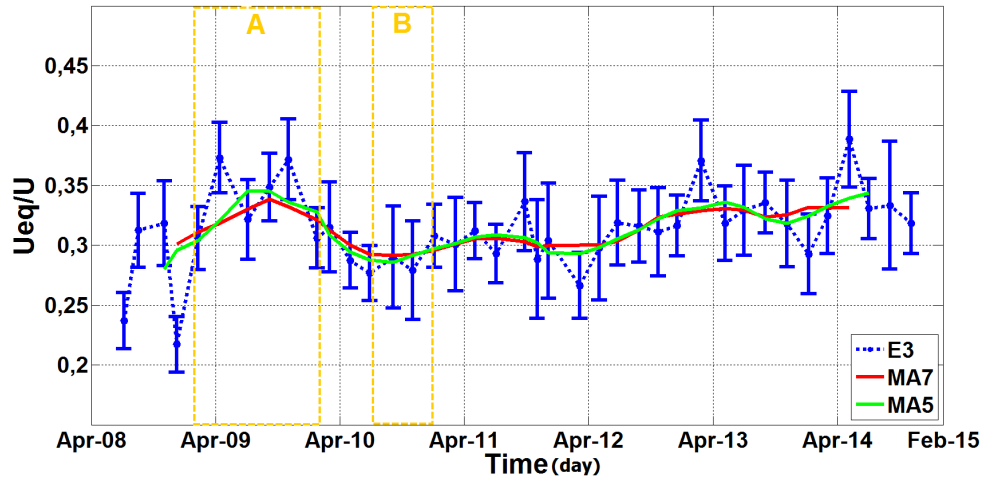


Figure 4.13: U_{eq}/U bimestrial series for site E3, as solid lines are also plotted Moving Average on 7 terms (red) and Moving Average on 5 terms (green). With dashed orange rectangles periods of relative intense seismic activity are indicated (Period A February–December 2009 and Period B July–December 2010).

E4

The E4 radium time series was analyzed on a bimestrial basis from July 2008 to November 2014, measuring 39 samples. It exhibits values in a range (0.07-0.12 fg/g) with mean of 0.094 fg/g and standard deviation of 0.013 fg/g. Uncertainty on single value again suffers from the poor count statistics related to the very low concentration (a factor two times lower than E3), so relative uncertainties range between 4% and 12% with a coverage factor $k = 1$.

On this sampling point uranium shows a mean value of 0.54 ng/g with a std of 0.06 ng/g and spike-like anomalies with relative variations of 30-60% localized before Period A.

^{226}Ra concentration was converted into U_{eq} concentration, and the ratio between U_{eq} and U concentrations was calculated. U_{eq}/U time series exhibits values in a range (0.29-0.75) with mean 0.49 and standard deviation of 0.1. This sampling point shows range of variation and mean higher than the previous one, but retains a ratio value always below 1. This means a decay chain out of equilibrium with a lower presence of ^{226}Ra than ^{238}U .

In figure 4.14 a time plot of U_{eq}/U together with smoothed MA7 and MA5 curves are reported.

U_{eq}/U shows a higher range of variation with the lowest values of the series localized before period A. After period B the data exhibit an increasing trend

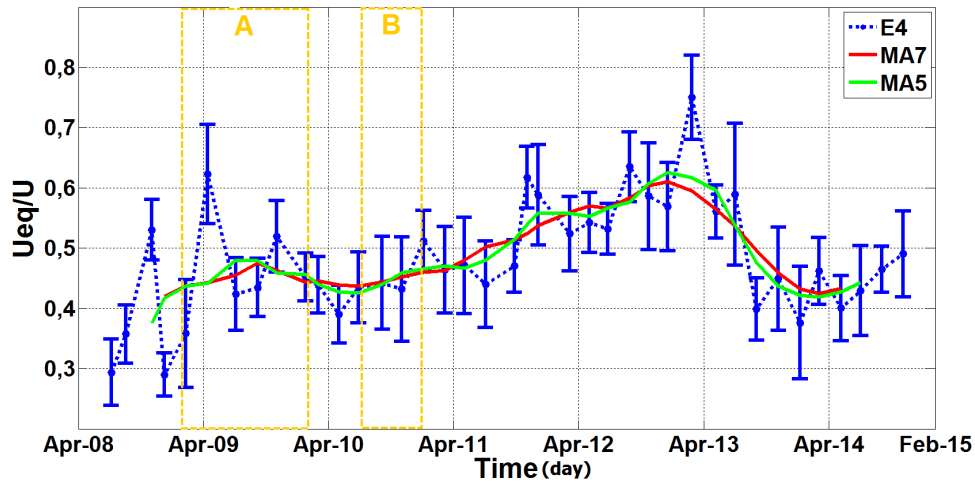


Figure 4.14: U_{eq}/U bimestrial series for site E4, as solid lines are also plotted Moving Average on 7 terms (red) and Moving Average on 5 terms (green). With dashed orange rectangles periods of relative intense seismic activity are indicated (Period A February–December 2009 and Period B July–December 2010).

followed by a decreasing one, which leads to values similar to the previous one.

Comparison

The E3 and E4 sampling sites exhibit different mean values and standard deviations of radium and uranium concentrations and of their ratio U_{eq}/U , as it can be seen in table 4.3, which means that the sites belong to two distinct radionuclides pools.

U_{eq}/U values were plotted with respect to uranium concentration in figure 4.15. This shows two clearly defined clusters consistent with the two sites. E4 shows a higher variability in U_{eq}/U with respect to E3. Both sites present values out of the relevant cluster, all characterized by high ^{238}U concentration and low U_{eq}/U .

In figure 4.16, U_{eq}/U original data series and the smoothed curve (MA7) for both sites were plotted, evidencing Period A and Period B of relatively intense seismic activity. E3 was characterized by a almost flat trend during the entire time span, while E4, as already pointed out for figure 4.15, showed higher mean and variability with an almost flat trend in the first part of the series followed by a structure in the second part. The lowest U_{eq}/U values have been identified in both sites before Period A; they represent spike-like

Table 4.3: Mean values and STD of ^{238}U , ^{226}Ra and U_{eq}/U for E3 and E4 sampling point

	Mean	STD
E3		
^{238}U (ng/g)	1.64	0.15
^{226}Ra (fg/g)	0.187	0.016
U_{eq}/U	0.31	0.03
E4		
^{238}U (ng/g)	0.54	0.06
^{226}Ra (fg/g)	0.094	0.013
U_{eq}/U	0.5	0.1

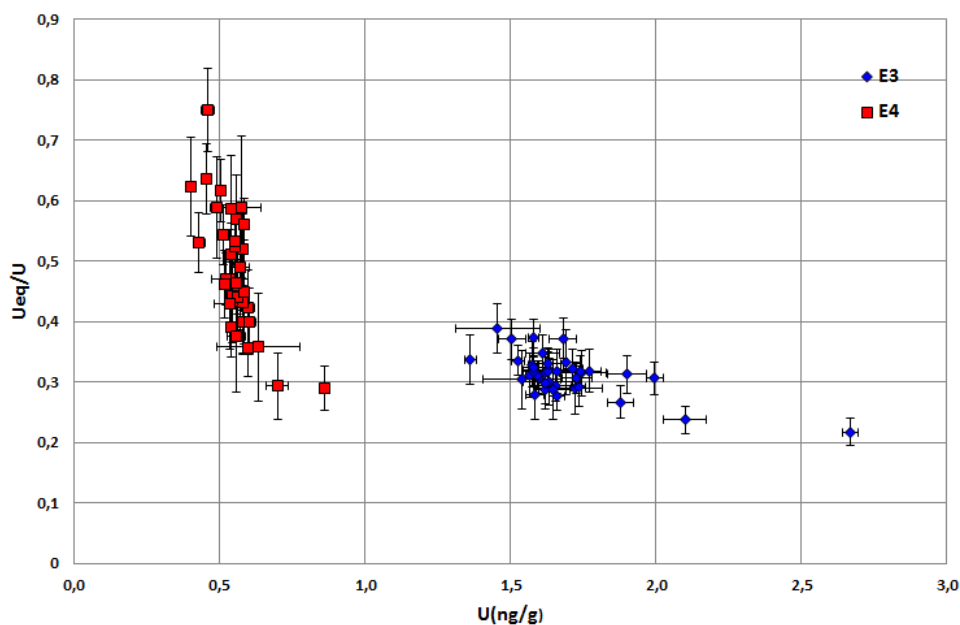


Figure 4.15: U_{eq}/U vs U concentrations for sites E3 and E4 are shown.

anomalies in uranium concentration time series and also values out of cluster in figure 4.15.

In order to explain the presence of a trend and to evaluate its nature,

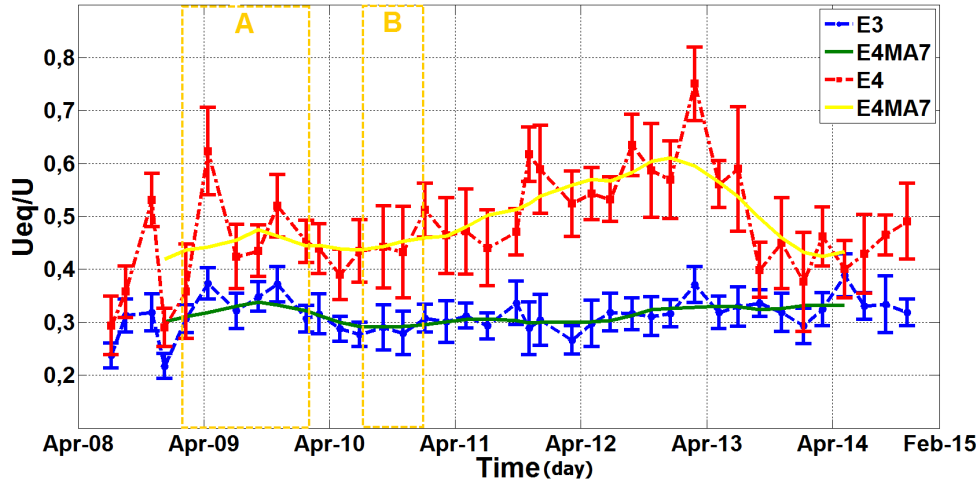


Figure 4.16: U_{eq}/U bimestrial series for sites E3 and E4 are plotted together with relevant Moving Average on 7 terms curves.

the correlation coefficients among U_{eq}/U and the variables from which it is calculated, were evaluated and reported in table 4.4.

Table 4.4: Correlation Coefficients Period 2

	Total	Period 1	Period 2
E3			
Corr(Ra, U_{eq}/U)	0.42	0.46	0.67
Corr(U, U_{eq}/U)	-0.68	-0.66	-0.76
E4			
Corr(Ra, U_{eq}/U)	0.81	0.53	0.88
Corr(U, U_{eq}/U)	-0.72	-0.85	-0.67

On site E4 anticorrelation with U can be observed in Period 1, while a clear correlation with Ra can be found in Period 2. Therefore the trend in the second part of the series could be assumed as being related to Ra behavior. It is then possible to assert that in Period 2 water-rock interaction processes, typical aspects of radium behavior, began to play a fundamental

role in the Ra/U ratio pattern over time, showing a recovery of the aquifer sector dynamics likely related to a provision of percolation water, that is almost completely inhibited in Period 1 (seismic activity), where flat trend were observed, and uranium dynamics is dominant.

4.5 Uranium isotope ratios analysis

In groundwater studies $^{234}U/^{238}U$ is used as a tracer for water mixing due to its observed variability among different water masses [9, 74]. As already explained in chapter one, a value of activity ratio above unity (secular equilibrium in ^{238}U decay chain) is registered worldwide and can be explained by means of the greater mobility of ^{234}U than ^{238}U and by means of ^{234}Th recoil from host aquifer rock and active layer pools.

Measuring the isotopic ratio on site E3 and E4 could be a useful tool for evaluating the mixing between this two reservoirs. Studying it over time and, in particular, before and after L'Aquila earthquake (6th April 2009) might provide useful pieces of information whether or not different conditions may arise from the seismic activity. Moreover including samples with observed uranium concentration anomalies can bring out possible differences in their isotopic compositions compared with the normal values.

The graph in figure 4.17 reports $^{235}U/^{238}U$ on the x axis and $^{234}U/^{238}U$ on the y axis, as a green dot. The value of the natural isotopic composition certified standard STD IRMM-3184 is also reported. For both sites a higher value of $^{234}U/^{238}U$ than the standard one is shown.

Figure 4.18 was obtained rescaling the previous graph and reporting uncertainties: two distinct clusters can be observed without any anomalous value. Uranium isotopic ratios were reported as molar ratios $n(U^{234})/n(U^{238})$; in this case the mean values and STD of the two clusters are $(7.20 | 0.05) * 10^{-5}$ for E3 and $(7.83 | 0.08) * 10^{-5}$ E4. Converting molar ratios in activity ratios, the results are $(1.311 | 0.009)$ E3 and $(1.424 | 0.014)$ E4.

In figure 4.19 by yellow and green indicators the $^{234}U/^{238}U$ and $^{235}U/^{238}U$ values of samples collected before L'Aquila earthquake are reported. They do not show statistically significant differences with values after the earthquake. The sampling dates before L'Aquila earthquake were chosen taking both those showing spike-like anomalies and near mean values of uranium concentration.

This study shows how these two sampling sites have distinct uranium isotopic ratio characterization, exhibiting values well clustered around the mean without outliers, implying that they belong to two well defined different reservoirs. The ratio does not vary before and after L'Aquila earthquake,

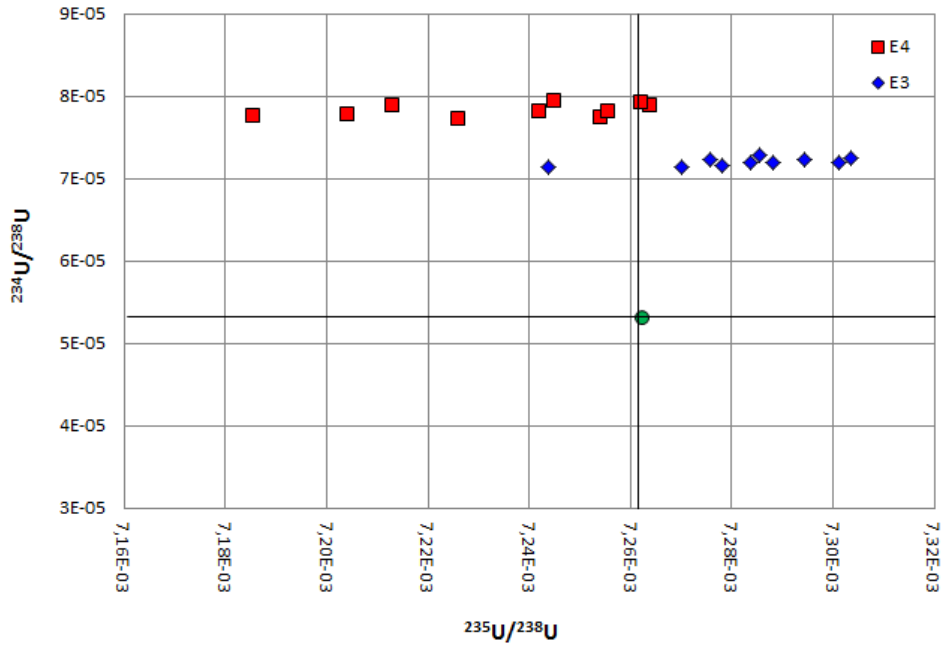


Figure 4.17: $^{234}\text{U}/^{238}\text{U}$ vs $^{235}\text{U}/^{238}\text{U}$ for E3 and E4 sampling points are shown. Green dot represents the standard certified values for these ratios.

therefore, no mixing through the fault, related to seismic activity, is recognizable. In addition to that it can be said that spike-like anomalies in uranium concentration for both sites have the same isotopic composition of the rest of the relevant time series.

4.6 Discussion

In this section the results from single elements measurement and analysis are gathered and evaluated as taken together. In table 4.5 ^3H , ^{226}Ra , ^{238}U and $^{234}\text{U}/^{238}\text{U}$ mean values and standard deviations are summarized.

Tritium data identify two water masses with different age, due to different infiltration mechanisms, percolation paths and residence times. Radium and uranium mean concentration together with uranium isotopic ratios, and disequilibria along the ^{238}U decay chain confirm that two water masses each with its own characteristics likely resulting from different host rock hydrogeological features, are being dealt with.

Studying the patterns of these variables over time has brought to several interesting results. The isotopic ratio $^{234}\text{U}/^{238}\text{U}$ on the two sites (figure 4.19) has pointed out two well defined cluster with no evidence of mixing

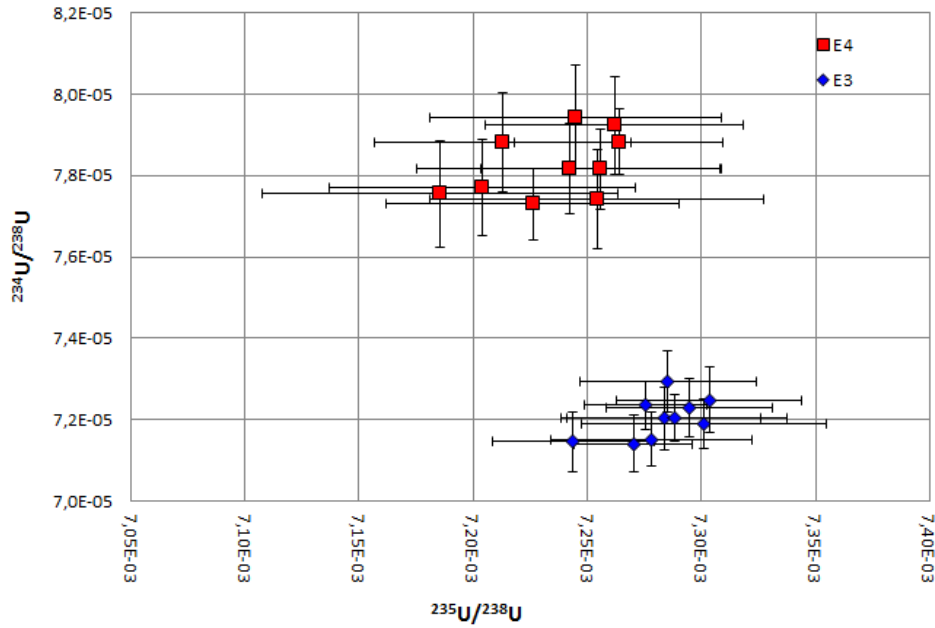


Figure 4.18: $^{234}\text{U}/^{238}\text{U}$ vs $^{235}\text{U}/^{238}\text{U}$ for E3 and E4 sampling points are shown. Relevant uncertainties are reported with a coverage factor $k = 2$.

Table 4.5: Means and std of the elements subject of the study for sites of interest. E3 tritium values shown are actually those of E3dx.

	^3H (TU)	^{226}Ra (fg/g)	^{238}U (ng/g)	U_{eq}/U	$^{234}\text{U}/^{238}\text{U}$
E3					
mean	7.5	0.187	1.64	0.31	1.311
STD	0.7	0.016	0.15	0.03	0.009
E4					
mean	6.2	0.094	0.54	0.5	1.424
STD	0.4	0.013	0.06	0.1	0.014

between them. This result is strongly confirmed by tritium analysis where pressure gradient should enable water movement from E3dx towards E4, but

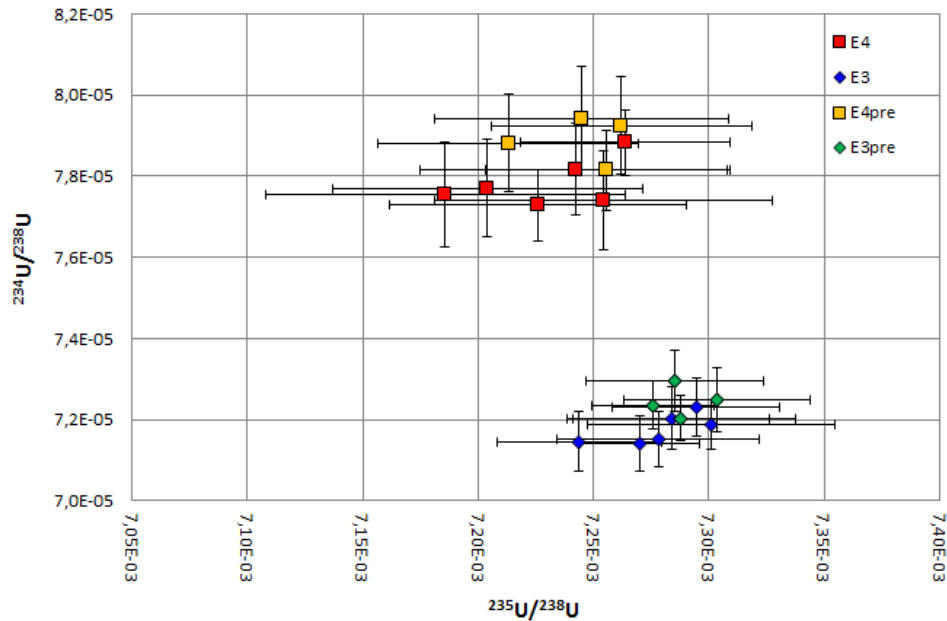


Figure 4.19: $^{234}\text{U}/^{238}\text{U}$ vs $^{235}\text{U}/^{238}\text{U}$ for E3 and E4 sampling points are shown. Values relative to dates before the L'Aquila earthquake are reported with yellow and green markers.

the presence of a long-term increasing trend in E3dx tritium time series, not recognizable in E4, denies this water movement, therefore excluding mixing between the two reservoirs. This is the first experimental evidence of the hydrological role of the overthrust fault, that, at least in the area of our investigation, behaves as a impermeable septum, separating two independent adjoining aquifer sectors.

The measurements cover a time span of 5 years between July 2008 and July 2013 in the tritium case, while of 6 years between July 2008 and November 2014 for the other elements. In that period, the Abruzzo region was the site of an intense seismic activity mostly clustered during the two periods of time A (February-December 2009) and B (July-December 2010), that culminated in the event of April 6, 2009 ($M_w = 6.3$).

It is interesting to evaluate the data collected with respect to the seismic activity. Its effects on fluids are reported in [2], considering the flow rate which is observed at the Traforo spring located in the highway tunnel close to the monitoring area (figure 4.20), which collects percolation water from the LNGS underground facilities and the highway tunnel. The Traforo spring flow rate showed a seasonal trend due to the snow melting during the Summer period. This trend was drastically modified during the main shock of 6th

April 2009, with a jump-like anomaly of about 120 L/s. This behavior could be explained by the presence of a locked normal fault when the fluids filling the cracks are squeezed out as a consequence of the hanging wall earthquake downward movement.

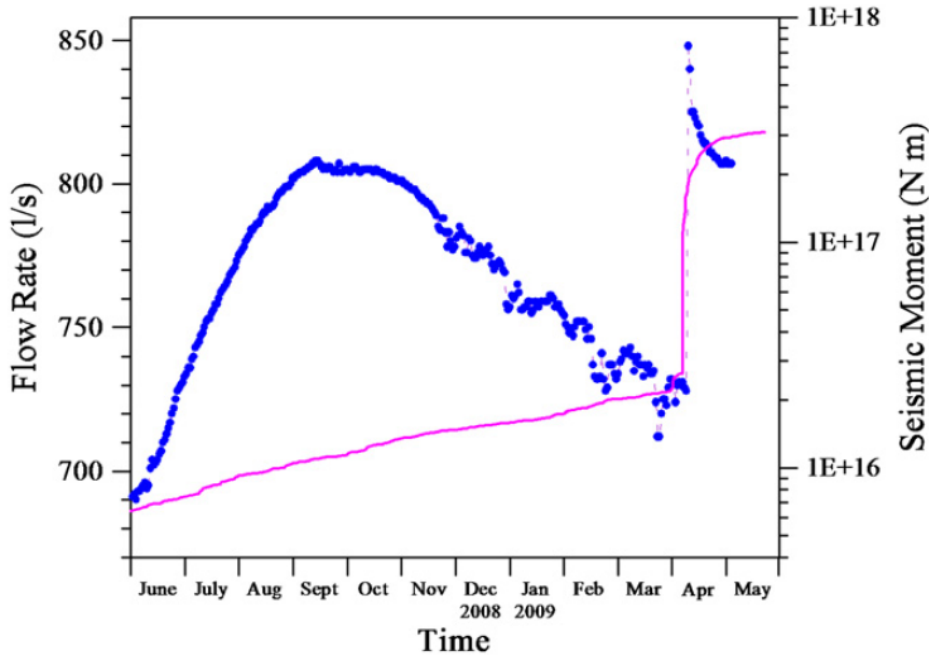


Figure 4.20: Flow rate observed at the Traforo spring, and cumulative seismic moment from January 2008 to May 2009. The jump-like raise in the cumulative seismic moment indicates the main shock on 6th April, 2009. The flow rate data are from the Ruzzo Waterwork Society. [2]

It is therefore to be noted that the absence of mixing result retain its validity even in this extreme situation.

Looking at the tritium activity concentration data (figure 4.12), the aquifer sectors responses to this strong hydrological alteration can be observed to last till the end of Period 1 (July 2008 - February 2011). This happened on both sites but with different modes. E3dx presented two damped and delayed oscillations, while E4 showed a linear trend without oscillation. In Period 2 (March 2011 - July 2013) both sites presented a common pattern with an oscillation that could be associated to water table movements. Different behaviors in Period 1 might be explained as a consequence of different hydrogeological features in the sampling sites, E3dx being inserted into a poor permeable porous dolomitic formation and E4 in a well drained limestone

formation.

Considering the Ra/U time series on both sites with respect to the seismic activity, the lowest ratio values were identified before L'Aquila seismic swarm (Period A in figure 4.16), they are due to spike-like anomalies in uranium concentration not followed by similar variations in radium concentration.

3H and $^{226}Ra/^{238}U$ analysis showed how in Period 1, when seismic swarms were present, younger percolation water supply was inhibited. This pattern is recognizable in both aquifer sectors despite their hydrological differences. Period 2, instead, was characterized by a recovery of the aquifer sectors dynamics related to water table movement and with percolation water supply.

The uranium isotopic composition in the two sites showed no appreciable differences with regards to seismic activity (figure 4.19), evidencing no mixing during pre-seismic and post-seismic periods. No appreciable differences in the isotopic composition were found also between the samples showing spike-like anomalies in uranium concentration values and the other samples.

Conclusions

The aim of this thesis was to ascertain whether the uranium behavior, studied at LNGS with respect to the seismic activity in the region, could be related to the Gran Sasso aquifer local dynamics. For this purpose a new approach has been developed of studying together and over time 3H , ^{226}Ra concentrations and $^{234}U/^{238}U$ isotopic ratio chosen due to their specific characteristics that enable different groundwater dynamics features to be investigated.

Measuring these quantities required the application of distinct techniques and sample preparation procedures: tritium was preconcentrated by means of electrolytic enrichment, a well-established procedure, and detected using Liquid Scintillation Spectrometry; while a method for radium separation and preconcentration by means of a sequential use of selective resins, followed by Inductively Coupled Plasma Mass Spectrometry measurement, was developed and optimized; uranium isotopic ratios were detected by ICP-MS, without sample pretreatment, applying an unconventional statistical data treatment. Measurements were performed on groundwater samples taken weekly from two sites inside LNGS-INFN, selected for their enviable position in describing the aquifer, that is on the two sides of the overthrust fault dividing a dolomitic formation from a limestone one.

Data analysis of the two sampling sites highlighted different mean contents and also different patterns over time; $^{234}U/^{238}U$ and 3H analysis excluded water mixing between them, locally configuring the aquifer as two separate sectors divided by an impermeable septum such as the overthrust fault.

During the time span of our analysis (July 2008 - November 2014) two seismic clusters occurred in the region of interest in Periods A (February - December 2009) and B (July - December 2010), the former culminating with the main shock of L'Aquila April 6, 2009 ($M_w = 6.3$).

The analysis of the 3H data collected showed a different response of the two water sectors to these solicitations, which might be related to the different hosting rock hydrogeological characteristics.

The analysis that were performed singled out that, during pre-seismic,

co-seismic and post-seismic periods, the 3H and $^{226}Ra/^{238}U$ data collected showed a common flat behavior which means an inhibited mixing with young superficial water. After Period B, then, a recover of the water table movement in the 3H data series along with changes occurring in water-rock interaction pattern in $^{226}Ra/^{238}U$ data series were observed.

These results highly support the hypothesis of the uranium concentration spike-like anomalies, observed before Period A in all sites and before Period B in E3dx only, being related to geodynamical processes and not being related to the input from the vadose zone, through variations of percolation processes linked to meteoric events, thus confirming the proposal of uranium groundwater content as a key geochemical signal of geodynamical processes that may occur in an earthquake preparation phase.

$^{234}U/^{238}U$ and $^{226}Ra/^{238}U$ data analysis provided further interesting information on samples with uranium concentration anomalous values: they showed appreciably unaltered $^{234}U/^{238}U$, while they exhibited the lowest $^{226}Ra/^{238}U$ ratio of the entire series. In order to fully interpret these features, the aquifer host rock elemental composition needs to be known.

Further study should try to clarify if these anomalies could be related with the upward movement of deep fluids, for example measuring and evaluating the ^{14}C concentration over time on the same sites of this work.

In order to confirm and further extend the knowledge acquired carrying out this project, the measurement campaign should be extended to other sites in the seismic area of subduction and normal fault.

Appendix A

Uncertainty Assessment

Tritium

Tritium electrolytic enrichment followed by LSC measurement is a long and complex procedure, consisting of several steps. Each step is characterized by different sources of uncertainty that must be taken into account and minimized when possible. Procedure steps and relevant uncertainty sources are reported in table A.1.

Tritium activity concentration was calculated following the equation (3.2):

$$A_T = \frac{N_{SA} A_{ST}}{N_{ST} Z_I} \exp D$$

The influence of different parameters in the above equation on the final result A_T are shown in figure A.1. The combined standard uncertainty of the measured quantity A_T can be expressed by the standard uncertainties of the parameters in the equation A.1 using the law of uncertainty propagation, that, in case of linear equations of a purely multiplicative form, is:

$$\frac{u(A_T)}{A_T} = \sqrt{\left(\frac{u(N_{SA})}{N_{SA}}\right)^2 + \left(\frac{u(N_{ST})}{N_{ST}}\right)^2 + \left(\frac{u(A_{ST})}{A_{ST}}\right)^2 + \left(\frac{u(Z_I)}{Z_I}\right)^2 + \left(\frac{u(D)}{D}\right)^2}$$

Referring to [30], that inspired this appendix, the dominating contributions to the overall uncertainty arise from Z_I and N_{SA} . The former was estimated using equation 3.5:

$$Z_I = \left(\frac{W_i}{W_f}\right)^{\frac{PQ}{(W_i - W_f)F}}$$

The standard uncertainty of enrichment factor Z_I for the given cell was calculated using the law of uncertainty propagation:

Table A.1: Breakdown of tritium enrichment and measurement the method in steps. Slightly modified from [30]

Step	Description	Symbol	Sources of uncertainty
1	Distillation of the water samples (initial distillation)		Possible contamination of low tritium content samples
2	Weighing of the cells before electrolysis	W_{CE}, W_{CI}, W_i	Uncertainty of electronic balance, buoyancy forces
3	Electrolysis of the water samples	Q	Uncertainty of amperehour-meter, current leaks
4	Weighing of the cells after electrolysis	W_{CE}, W_{CF}, W_f	Uncertainty of electronic balance, buoyancy forces
5	Neutralisation and distillation of the water samples after enrichment (final distillation)		Possible contamination of samples with low tritium content, too high pH in the distilled sample
6	Preparation of the scintillation mixture	V_W	Uncertainty of pipettes volumes, temperature of the preparation process, exposure of the scintillation mixture to sunlight
7	Radioactivity measurement	N_{SA}, N_{ST}, N_B	Random variations of count rates, long-term stability of the spectrometer, static charges, fluorescence
8	Calculating the actual enrichment parameter for the sample cell	P	Temperature of the enrichment process, losses of water due to evaporation from the cells, propagation of uncertainties associated with steps 2-7
9	Calculating the enrichment factor for each sample	Z_I	Temperature of the enrichment process, losses of water due to evaporation from the cells, propagation of uncertainties associated with steps 2-8
10	Calculating the decay correction factor	D	Uncertainty of the decay constant for tritium
11	Tritium standard and dilution	A_{ST}	Uncertainty of the certified high-level standard, dilution procedure
12	Calculating tritium activity concentration in the sample	A_T	Propagation of uncertainties associated with steps 2-11

$$u(Z_I) = \sqrt{\left(\frac{\partial Z_I}{\partial Q}\right)^2 (u(Q))^2 + \left(\frac{\partial Z_I}{\partial P}\right)^2 (u(P))^2 + \left(\frac{\partial Z_I}{\partial W_i}\right)^2 (u(W_i))^2 + \left(\frac{\partial Z_I}{\partial W_f}\right)^2 (u(W_f))^2}$$

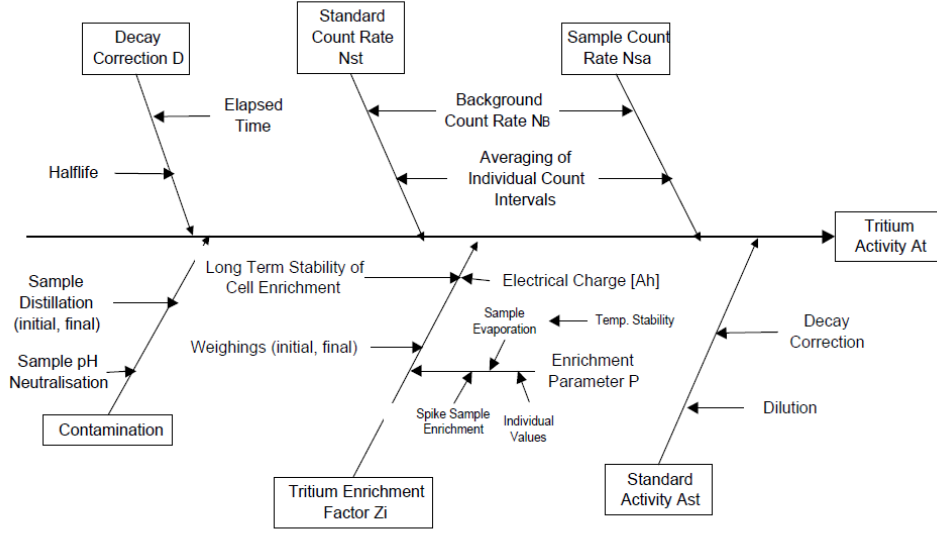


Figure A.1: Fishbone Diagram (Cause and Effect Diagram) showing the influence of the different parameters in Formula (3.1) on the final result A_T . [30]

the initial and final water masses W_i and W_f were calculated according to:

$$W_i = (W_{CI} + 0.49) - W_{CE}$$

$$W_f = (W_{CF} + 0.02) - W_{CE}$$

where W_{CE} is the weight of the empty electrolytic cell, W_{CI} and W_{Cf} are the weights of cell filled with the initial and final water mass respectively. In addition buoyancy correction terms have to be applied for W_{CI} and W_{Cf} to account for the decrease of specific density of the complete system of cells and water (steel and water) compared to the empty cells and the calibration weight (steel), which results in a slight underestimation of the actual determined mass. By calculating partial derivatives of Z_I and inserting the appropriate values of the parameters and their estimated standard uncertainties we obtain a typical value of $u(Z_I) = 0.26$ for a value of $Z_I = 17.73$ obtaining a relative uncertainty of:

$$\frac{u(Z_I)}{Z_I} = 0.015$$

The standard uncertainties of the net count rates (N_{SA}) of the sample and of standard are calculated according to the law of uncertainty propagation. As additional component the uncertainty of the scintillation mixture preparation is included ($u(V_W)$). A typical reading of it is:

$$\frac{u(N_{SA})}{N_{SA}} = \sqrt{\left(\frac{\sqrt{u(N_{GSA})^2 + u(N_B)^2}}{N_{SA}}\right)^2 + \left(\frac{u(V_W)}{V_W}\right)^2} = 0.033$$

Radium

^{226}Ra concentration measurements were performed by ICP-MS, after pre-treating the samples with the procedure outlined in chapter 3. This procedure mainly consists of the sequential application of a cation exchange resin and an extraction chromatographic resin, in order to separate the radium from the principal matrix constituents and from the interfering elements, and to concentrate the radium in the samples. After this treatment radium count rates were measured by ICP-MS and converted into concentrations by acquiring an external standard calibration curve consisting of five standards from 0 to 55 fg g^{-1} . The standard solutions were prepared by means of gravimetricall dilution and mimicking the sample matrix composition after the entire procedure. An example of calibration curve for Ra-226 is reported in figure A.2.

In [57] and in chapter 3 a study of the influence of varying acid molarity on the separation and recovery efficiencies was performed for each step. It clearly showed the best elution conditions, but effects of slight acid molarity variations in the single step due, for example, to uncertainties of the calibrated pipette set used for dilution, on the efficiency of the entire procedure are difficult to quantify. Therefore an overall assessment of the uncertainties related to the chemical preparation of the sample, and of the ^{226}Ra recovery efficiency (R_ϵ) of the procedure was performed on twelve independently eluted groundwater samples spiked at 22 fg g^{-1} . A R_ϵ value equal to 1 was obtained with a relative uncertainty of

$$\frac{u(R_\epsilon)}{R_\epsilon} = 0.035$$

The reported results of radium concentration (Ra_{RE}) were calculated following:

$$Ra_{RE} = Ra_{MS} \frac{1}{R_\epsilon}$$

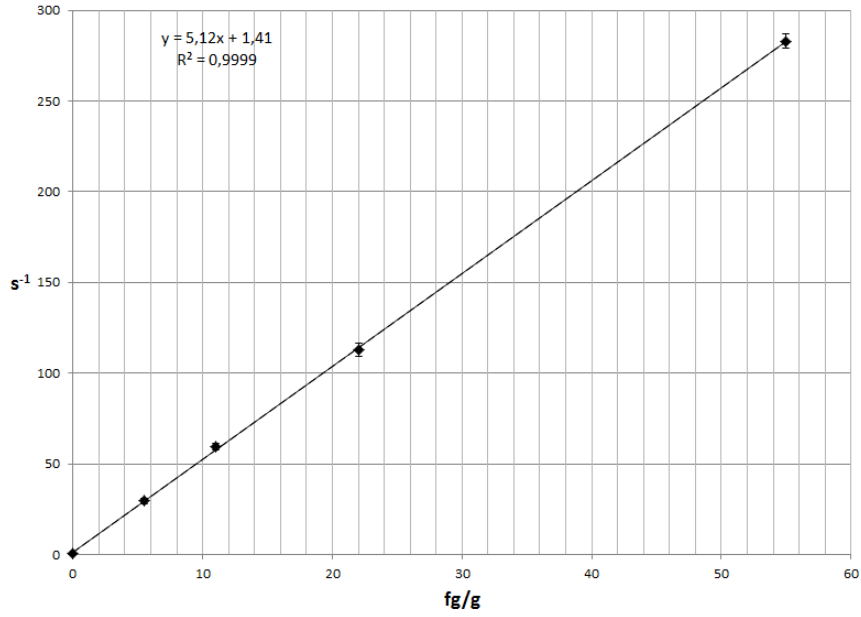


Figure A.2: An example of ^{226}Ra calibration curve on five levels from 5,5 to 55 fg/g ; in the graph the linear regression curve and the relevant R^2 are also reported.

where Ra_{MS} is the radium concentration value measured by the ICP-MS. The combined standard uncertainty of Ra_{RE} can be expressed as:

$$\frac{u(Ra_{RE})}{Ra_{RE}} = \sqrt{\left(\frac{u(Ra_{MS})}{Ra_{MS}}\right)^2 + \left(\frac{R_{\epsilon}}{R_{\epsilon}}\right)^2}$$

Bibliography

- [1] W. Plastino, S. Nisi, G. De Luca, M. Balata, M. Laubenstein, and F. Bella, “Environmental radioactivity in the ground water at the gran sasso national laboratory (italy): a possible contribution to the variation of the neutron flux background,” *Journal of radioanalytical and nuclear chemistry*, vol. 282, no. 3, pp. 809–813, 2009.
- [2] W. Plastino, P. P. Povinec, G. D. Luca, C. Doglioni, S. Nisi, L. Ioannucci, M. Balata, M. Laubenstein, F. Bella, and E. Coccia, “Uranium groundwater anomalies and l’aquila earthquake, 6th april 2009 (italy),” *Journal of Environmental Radioactivity*, vol. 101, no. 1, pp. 45 – 50, 2010.
- [3] W. Plastino, G. Panza, C. Doglioni, M. Frezzotti, A. Peccerillo, P. De Felice, F. Bella, P. Povinec, S. Nisi, L. Ioannucci, P. Aprili, M. Balata, M. Cozzella, and M. Laubenstein, “Uranium groundwater anomalies and active normal faulting,” *Journal of Radioanalytical and Nuclear Chemistry*, vol. 288, no. 1, pp. 101–107, 2011.
- [4] C. Hammond, *Handbook of Chemistry and Physics*. CRC press, 81st edition ed., 2000.
- [5] B. Bourdon, S. Turner, G. M. Henderson, and C. C. Lundstrom, “Introduction to u-series geochemistry,” *Reviews in Mineralogy and Geochemistry*, vol. 52, no. 1, pp. 1–21, 2003.
- [6] K. Krupka and R. Serne, “Geochemical factors affecting the behavior of antimony, cobalt, europium, technetium, and uranium in vadose sediments.”
- [7] M. Gascoyne, “Geochemistry of the actinides and their daughters,” in *Uranium-series disequilibrium: applications to earth, marine, and environmental sciences. 2. ed*, 1992.

- [8] D. Porcelli and P. W. Swarzenski, “The behavior of u-and th-series nuclides in groundwater,” *Reviews in Mineralogy and Geochemistry*, vol. 52, no. 1, pp. 317–361, 2003.
- [9] T.-L. Ku, S. Luo, B. Leslie, and D. Hammond, “Decay-series disequilibria applied to the study of rock-water interaction and geothermal systems,” in *Uranium-series disequilibrium: applications to earth, marine, and environmental sciences. 2. ed*, 1992.
- [10] A. Tricca, D. Porcelli, and G. Wasserburg, “Factors controlling the groundwater transport of u, th, ra, and rn,” *Journal of Earth System Science*, vol. 109, no. 1, pp. 95–108, 2000.
- [11] D. Porcelli, *Investigating groundwater processes using U-and Th-series nuclides*, pp. 105–153. Elsevier, 2008.
- [12] K. Rozanski, R. Gonfiantini, and L. Araguas-Araguas, “Tritium in the global atmosphere: Distribution patterns and recent trends,” *Journal of Physics G: Nuclear and Particle Physics*, vol. 17, no. S, p. S523, 1991.
- [13] C. Eastoe, C. Watts, M. Ploughe, and W. Wright, “Future use of tritium in mapping pre-bomb groundwater volumes,” *Groundwater*, vol. 50, no. 1, pp. 87–93, 2012.
- [14] A. Grosse, W. Johnston, R. Wolfgang, and W. Libby, “Tritium in nature,” *Science*, vol. 113, no. 2923, pp. 1–2, 1951.
- [15] I. Cartwright and U. Morgenstern, “Constraining groundwater recharge and the rate of geochemical processes using tritium and major ion geochemistry: Ovens catchment, southeast australia,” *Journal of Hydrology*, vol. 475, pp. 137–149, 2012.
- [16] H. E. Taylor, “Chapter 4 - instrumentation,” in *Inductively Coupled Plasma-Mass Spectrometry* (H. E. Taylor, ed.), pp. 29 – 51, Academic Press, 2001.
- [17] J. T. Watson and O. D. Sparkman, *Electron Ionization*, pp. 315–448. John Wiley and Sons, Ltd, 2008.
- [18] J. ter Wiel and T. C. Hegge, “Advances in scintillation cocktails,” in *Liquid Scintillation Counting and Organic Scintillators*, pp. 51–67, Lewis Chelsea, Michigan, 1991.

- [19] M. F. L'Annunziata and M. J. Kessler, "Chapter 7 - liquid scintillation analysis: Principles and practice," in *Handbook of Radioactivity Analysis (Third Edition)* (M. F. L'Annunziata, ed.), pp. 423 – 573, Amsterdam: Academic Press, third edition ed., 2012.
- [20] G. F. Knoll, *Scintillation Detection Principles*, pp. 219–264. John Wiley and Sons, Ltd, 2010.
- [21] M. J. Kessler, "Applications of quench monitoring using transformed external standard spectrum (tsie)," in *Liquid Scintillation Counting and Organic Scintillators*, pp. 343–364, Lewis Publishers, Chelsea, MI, 1991.
- [22] J. Thomson, "Di-isopropylnaphthalene. a new solvent for liquid scintillation counting," in *Liquid Scintillation Counting and Organic Scintillators*, pp. 19–34, Lewis Chelsea, Michigan, 1991.
- [23] C. Arpesella, "A low background counting facility at laboratori nazionali del gran sasso," *Applied Radiation and Isotopes*, vol. 47, no. 9, pp. 991–996, 1996.
- [24] W. Plastino, L. Kaihola, P. Bartolomei, and F. Bella, "Cosmic background reduction in the radiocarbon measurements by liquid scintillation spectrometry at the underground laboratory of gran sasso," *Radiocarbon*, vol. 43, no. 2; PART A, pp. 157–162, 2001.
- [25] T. Florkowski, "Low-level tritium assay in water samples by electrolytic enrichment and liquid-scintillation counting in the iaea laboratory," in *Methods of low-level counting and spectrometry*, 1981.
- [26] G. Sauzay and W. Schell, "Analysis of low level tritium concentrations by electrolytic enrichment and liquid scintillation counting," *The International Journal of Applied Radiation and Isotopes*, vol. 23, no. 1, pp. 25–33, 1972.
- [27] C. Taylor, "Tritium enrichment of environmental waters by electrolysis: development of cathodes exhibiting high isotopic separation and precise measurement of tritium enrichment factors," *Proceedings of the international conference on low radioactivity measurements and applications*, pp. 131–140, 1976.
- [28] U. Morgenstern and C. B. Taylor, "Ultra low-level tritium measurement using electrolytic enrichment and lsc," *Isotopes in Environmental and Health Studies*, vol. 45, no. 2, pp. 96–117, 2009. PMID: 20183224.

- [29] W. Plastino, I. Chereji, S. Cuna, L. Kaihola, P. D. Felice, N. Lupsa, G. Balas, V. Mirel, P. Berdea, and C. Baciú, “Tritium in water electrolytic enrichment and liquid scintillation counting,” *Radiation Measurements*, vol. 42, no. 1, pp. 68 – 73, 2007.
- [30] K. Rozanski and M. Gröning, “Tritium assay in water samples using electrolytic enrichment and liquid scintillation spectrometry,” *Quantifying uncertainty in nuclear analytical measurements. IAEA-TECDOC-1401*, IAEA, Vienna, pp. 195–217, 2004.
- [31] M. Gröning and K. Rozanski, “Uncertainty assessment of environmental tritium measurements in water,” *Accreditation and Quality Assurance*, vol. 8, no. 7-8, pp. 359–366, 2003.
- [32] A. Baeza, E. García, and C. Miró, “A procedure for the determination of very low activity levels of tritium in water samples,” *Journal of radioanalytical and nuclear chemistry*, vol. 241, no. 1, pp. 93–100, 1999.
- [33] M. Kakiuchi, K. Tanaka, and K. Kigoshi, “Natural tritium measurements: determination of the electrolytic enrichment factor of tritium,” *International Journal of Radiation Applications and Instrumentation. Part A. Applied Radiation and Isotopes*, vol. 42, no. 8, pp. 741–748, 1991.
- [34] P. Theodorsson, “A review of low-level tritium systems and sensitivity requirements,” *Applied radiation and isotopes*, vol. 50, no. 2, pp. 311–316, 1999.
- [35] M. Groening, R. Auer, D. Brummer, M. Jaklitsch, C. Sambandam, A. Tanweer, and H. Tatzber, “Increasing the performance of tritium analysis by electrolytic enrichment†,” *Isotopes in environmental and health studies*, vol. 45, no. 2, pp. 118–125, 2009.
- [36] I. Schäfer, D. Hebert, and U. Zeiske, “On low-level tritium measurements with lsc quantulus,” *Applied Radiation and Isotopes*, vol. 53, no. 1, pp. 309–315, 2000.
- [37] P. Benzi, F. Nebbóa, R. Righetti, and P. Volpe, “Electrolytical enrichment for liquid scintillation determinations of low tritium samples: A revised methodology,” *Journal of Radioanalytical and Nuclear Chemistry*, vol. 196, no. 1, pp. 15–24, 1995.

- [38] G. Hut, “Low-level tritium counting facilities: A survey,” *Nuclear Instruments and Methods in Physics Research Section B: Beam Interactions with Materials and Atoms*, vol. 17, no. 5, pp. 490–492, 1986.
- [39] M. Villa and G. Manjón, “Low-level measurements of tritium in water,” *Applied radiation and Isotopes*, vol. 61, no. 2, pp. 319–323, 2004.
- [40] H. Satake and S. Takeuchi, “Electrolytic enrichment of tritium with fe-ni and ni-ni electrodes and estimation of tritium enrichment factor using fe-ni electrodes.,” *GEOCHEMICAL JOURNAL*, vol. 25, no. 6, pp. 429–435, 1991.
- [41] S. Gupta and H. Polach, “Radiocarbon dating practices at anu: Handbook, radiocarbon laboratory, research school of pacific studies,” *Canberra, Australia: Australian National University*, 1985.
- [42] E. W. Group, S. Ellison, A. Williams, Eurachem, and C. operation on International Traceability in Analytical Chemistry, *Quantifying Uncertainty in Analytical Measurement*. CITAC guide, LGC (Teddington) Limited, 2000.
- [43] G. Kim, W. C. Burnett, H. Dulaiova, P. W. Swarzenski, and W. S. Moore, “Measurement of 224ra and 226ra activities in natural waters using a radon-in-air monitor,” *Environmental Science and Technology*, vol. 35, no. 23, pp. 4680–4683, 2001. PMID: 11770771.
- [44] U. Repinc and L. Benedik, “Development of a method for the determination of 226ra by liquid scintillation counting,” *Journal of Radioanalytical and Nuclear Chemistry*, vol. 254, no. 1, pp. 181–185, 2002.
- [45] K. Morvan, Y. Andres, B. Mokili, and J.-C. Abbe, “Determination of radium-226 in aqueous solutions by alpha-spectrometry,” *Analytical Chemistry*, vol. 73, no. 17, pp. 4218–4224, 2001. PMID: 11569812.
- [46] A. Johnston and P. Martin, “Rapid analysis of 226ra in waters by gamma-ray spectrometry,” *Applied Radiation and Isotopes*, vol. 48, no. 5, pp. 631 – 638, 1997.
- [47] A. S. Cohen and R. K. O’Nions, “Precise determination of femtogram quantities of radium by thermal ionization mass spectrometry,” *Analytical Chemistry*, vol. 63, no. 23, pp. 2705–2708, 1991.
- [48] F. Chabaux, D. Othman, and J. Birck, “A new ra-ba chromatographic separation and its application to ra mass-spectrometric measurement in volcanic rocks,” *Chemical Geology*, vol. 114, no. 3–4, pp. 191 – 197, 1994.

- [49] C. J. Park, P. J. Oh, H. Y. Kim, and D. S. Lee, "Determination of ^{226}Ra in mineral waters by high-resolution inductively coupled plasma mass spectrometry after sample preparation by cation exchange," *J. Anal. At. Spectrom.*, vol. 14, pp. 223–227, 1999.
- [50] D. Lariviere, V. N. Epov, R. D. Evans, and R. J. Cornett, "Determination of radium-226 in environmental samples by inductively coupled plasma mass spectrometry after sequential selective extraction," *J. Anal. At. Spectrom.*, vol. 18, pp. 338–343, 2003.
- [51] D. Lariviere, V. Epov, K. Reiber, R. Cornett, and R. Evans, "Micro-extraction procedures for the determination of ^{226}Ra in well waters by sf-icp-ms," *Analytica Chimica Acta*, vol. 528, no. 2, pp. 175 – 182, 2005.
- [52] Z. Varga, "Ultratrace-level radium-226 determination in seawater samples by isotope dilution inductively coupled plasma mass spectrometry," *Analytical and Bioanalytical Chemistry*, vol. 390, no. 2, pp. 511–519, 2008.
- [53] M. L. Cozzella, A. Leila, and R. S. Hernandez, "Determination of ^{226}Ra in urine samples by q-icp-ms: A method for routine analyses," *Radiation Measurements*, vol. 46, no. 1, pp. 109 – 111, 2011.
- [54] B. Reynolds, G. Wasserburg, and M. Baskaran, "The transport of u- and th-series nuclides in sandy confined aquifers," *Geochimica et Cosmochimica Acta*, vol. 67, no. 11, pp. 1955 – 1972, 2003.
- [55] W. Plastino, M. Laubenstein, S. Nisi, A. Peresan, P. Povinec, M. Balata, F. Bella, A. Cardarelli, M. Ciarletti, L. Copia, M. De Deo, B. Gallese, and L. Ioannucci, "Uranium, radium and tritium groundwater monitoring at infn-gran sasso national laboratory, italy," *Journal of Radioanalytical and Nuclear Chemistry*, vol. 295, no. 1, pp. 585–592, 2013.
- [56] E. Philip Horwitz, R. Chiarizia, and M. L. Dietz, "A novel strontium-selective extraction chromatographic resin*," *Solvent Extraction and Ion Exchange*, vol. 10, no. 2, pp. 313–336, 1992.
- [57] L. Copia, S. Nisi, W. Plastino, M. Ciarletti, and P. P. Povinec, "Low-level ^{226}Ra determination in groundwater by sf-icp-ms: optimization of separation and pre-concentration methods," *Journal of Analytical Science and Technology*, vol. 6, no. 1, pp. 1–7, 2015.
- [58] M. Hamester, D. Wiederin, J. Wills, W. Kerl, and C. B. Douthitt, "Strategies for isotope ratio measurements with a double focusing sector

- field icp-ms,” *Fresenius’ Journal of Analytical Chemistry*, vol. 364, no. 5, pp. 495–498, 1999.
- [59] V. Epov, D. Lariviere, R. Evans, C. Li, and R. Cornett, “Direct determination of ²²⁶Ra in environmental matrices using collision cell inductively coupled plasma mass-spectrometry,” *Journal of Radioanalytical and Nuclear Chemistry*, vol. 256, no. 1, pp. 53–60, 2003.
- [60] P. R. Trincherini, C. Baffi, P. Barbero, E. Pizzoglio, and S. Spalla, “Precise determination of strontium isotope ratios by tims to authenticate tomato geographical origin,” *Food chemistry*, vol. 145, pp. 349–355, 2014.
- [61] P. R. Trincherini, C. Domergue, I. Manteca, A. Nesta, and P. Quarati, “The identification of lead ingots from the roman mines of cartagena: the role of lead isotope analysis,” *Journal of Roman Archaeology*, vol. 22, pp. 123–145, 2009.
- [62] F. Albarède and B. Beard, “Analytical methods for non-traditional isotopes,” *Reviews in mineralogy and geochemistry*, vol. 55, no. 1, pp. 113–152, 2004.
- [63] S. M. Nelms, C. R. Quétel, T. Prohaska, J. Vogl, and P. D. Taylor, “Evaluation of detector dead time calculation models for icp-ms,” *Journal of Analytical Atomic Spectrometry*, vol. 16, no. 4, pp. 333–338, 2001.
- [64] W. Plastino and F. Bella, “Radon groundwater monitoring at underground laboratories of gran sasso (italy),” *Geophysical Research Letters*, vol. 28, no. 14, pp. 2675–2677, 2001.
- [65] F. Bella, P. Biagi, M. Caputo, E. Cozzi, G. Della Monica, A. Ermini, W. Plastino, and V. Sgrigna, “Aquifer-induced seismicity in the central apennines (italy),” *pure and applied geophysics*, vol. 153, no. 1, pp. 179–194, 1998.
- [66] C. Boni, P. Bono, and G. Capelli, “Schema idrogeologico dell’italia centrale,” vol. 35, pp. 991–1012, 1986.
- [67] M. Ciarletti, W. Plastino, A. Peresan, S. Nisi, L. Copia, G. F. Panza, and P. P. Povinec, “Uranium groundwater monitoring and seismic analysis: A case study of the gran sasso hydrogeological basin, italy,” *Pure and Applied Geophysics*, pp. 1–17, 2015.
- [68] A.N.A.S.-CO.GE.FAR., “Gran sasso, il traforo autostradale,” 1980.

- [69] W. Plastino, M. Laubenstein, S. Nisi, A. Peresan, P. P. Povinec, M. Balata, F. Bella, A. Cardarelli, M. Ciarletti, L. Copia, *et al.*, “Uranium, radium and tritium groundwater monitoring at infn-gran sasso national laboratory, italy,” *Journal of Radioanalytical and Nuclear Chemistry*, vol. 295, no. 1, pp. 585–592, 2013.
- [70] A. Akinci, F. Galadini, D. Pantosti, M. Petersen, L. Malagnini, and D. Perkins, “Effect of time dependence on probabilistic seismic-hazard maps and deaggregation for the central apennines, italy,” *Bulletin of the Seismological Society of America*, vol. 99, no. 2A, pp. 585–610, 2009.
- [71] E. Falcucci, S. Gori, M. Moro, A. R. Pisani, D. Melini, F. Galadini, and P. Fredi, “The 2009 l’aquila earthquake (italy): what’s next in the region? hints from stress diffusion analysis and normal fault activity,” *Earth and Planetary Science Letters*, vol. 305, no. 3, pp. 350–358, 2011.
- [72] L. Copia, “Analisi di uranio, radio e trizio in acqua a infn-laboratori nazionali del gran sasso nell’ambito dell’esperimento ermes.”
- [73] C. Chatfield, *The analysis of time series: an introduction*. CRC press, 6th ed., 2013.
- [74] R. Tripathi, S. Sahoo, S. Mohapatra, P. Lenka, J. Dubey, and V. Puranik, “Study of uranium isotopic composition in groundwater and deviation from secular equilibrium condition,” *Journal of Radioanalytical and Nuclear Chemistry*, vol. 295, no. 2, pp. 1195–1200, 2013.